A Visual Study of the Coanda Effect on a Circular Wall Water Jet Off-Set from a Smooth Flat Plate

by

SAMER H. MAHMOUD

B.S., Kansas State University, 1992

A THESIS

submitted in partial fulfillment of the

requirements for the degree

MASTER OF SCIENCE

Department of Mechanical Engineering
College of Engineering

KANSAS STATE UNIVERSITY
Manhattan, Kansas

1996

Approved by:

B. Terry Beck
Major Professor

Abstract

This work includes a visual study of the conda effects on the three dimensional laminar wall jet issuing from a circular opening parallel to a flat plate that is offset certain distance away from the nozzle center. The effect of varying the plate-to-nozzle distance on the laminar jet was investigated for five values of the plate-to-nozzle heights. It was verified as predicted by previous research that the point of the jet attachment to the wall moves away from the nozzle as the jet-to-nozzle distance increased. Also, the effect of the temperature variation between the jet and its surroundings were investigated qualitatively. The temperature difference between the jet and the surrounding was changed for a fixed nozzle-to-plate height. For the cold jet, at the low Reynolds Number, the jet remained detached from the plate. Some periodic instabilities were observed in the axial shape of the jet at distances further away from the nozzle. The effect of varying the flow rate on the jet were studied qualitatively. The jet axial and cross-sectional images obtained show how the jet shape changed with time. Simple two-dimensional theory was used to predict the attachment distance for the isothermal circular jet. No quantitative velocity profile measurements of the jet were undertaken in this study which was a preliminary investigation for building a scaled model for later studying of the air diffusion mechanisms of jet-wall interaction.

Table of Contents

Page

Page

Page

Nomenclature

Roman

a: distance between the camera focal plane and the air/water interface, [m]

Ar_c: Critical Archemides number

b: Distance between the calibration frame of refrence and the the water /air interface, [m]

d: Distance measured along the scale during calibration, [m]

D: Nozzle Diameter, [m]

d_h: Horizontal distance measured along the scale during calibration, [m]

d_v: Vertical distance measured along the scale during calibration, [m]

E_d: Absolute uncertainty in measuring scale distances during calibration, [m]

$E_{\Delta T}$: Absolute uncertainty in measuring the temperature difference, [°C]

$E_{\Delta x}$: Absolute uncertainty in measuring number of pixels between two image points, [pixels]

E_k: Absolute uncertainty in the scale factor, [m/pixel]

E_L: Absolute uncertainty in the jet-to-plate attachment length, [m]

e_L: Relative uncertainty in the jet-to-plate attachment length

E_m: Accuracy of the scale used during calibration, [m]

E_r: Absolute uncertainty in resolving point location on the image, [pixel]

E_s: Absolute uncertainty associated with Scattering of the scale distance measurement from the best fit line through the scale image pixel coordinates, [m]

E_{sk}: Absolute uncertainty due scattering between the scale factor data from the linear fit, [m/pixel]

f: focal length of the camera focusing lens (12 mm), [m]

h: Ceiling-to-nozzle Height, [m]

I_h: Image horizontal dimension, [pixel]

I_v: Image vertical dimension, [pixel]

J: Jet momentum, [kg.m/sec^2]

Jo: Jet Momentum at the nozzle , [kg.m/sec^2]

k_x: Image horizontal scale factor, [m/pixel]

k_y: Image vertical scale factor, [m/pixel]

L: Jet-to-plate attachment length , [m]

m: Jet mass flow rate, [kg/s]

m_h: Slope of the best linear fit of the horizontal scale dimension versus the horizontal pixel count for the horizontal scale line referenced during calibration, [m/pixel]

m_v: Slope of the best linear fit of the vertical scale dimension versus the vertical pixel count for the vertical scale line referenced during calibration, [m/pixel]

m_{xy}: Slope of the best linear fit of the horizontal pixel count versus the vertical pixel count for the vertical scale line referenced during calibration

m_{yx}: Slope of the best linear fit of the vertical pixel count versus the horizontal pixel count for the horizontal scale line referenced during calibration

n_a: air index of refraction

n_w: water index of refraction

O_h: Horizontal dimension of Object being imaged, [m]

O_v: Vertical dimension of Object being imaged, [m]

R: Jet trajectory radius of curvature, [m]

Re: Nozzle Reynolds number, [m]

t: Time, [second]

T: Integration substitution variable, see Equation # D.16

T_{avg}: Average temperature reading of all thermocouple used during calibration, [°C]

Td: Discharge temperature, [°C]

T_∞: Ambient water temperature, [°C]

T_m: Measured jet discharge temperature, [°C]

u: In-line jet velocity, [m/s]

U_{max}: Center line jet velocity, [m/s]

V: Volume flow rate, [m^3/s]

x: image horizontal coordinates, [pixel]

X: X-axis of the Coordinates system, [m]

X_1: Axial distance along jet axis to wall attachment point, [m]

Xo: Distance between the nozzle and the jet virtual origin, [m]

y: Image vertical coordinate, [pixel]

Y: Y-axis of the Coordinate system, [m]

y_d: Image height below the optical axis, [m]

y_i: Height above the optical axis at which ray #1 in Figure B.1 hits the glass, [m]

y_o: Object height above the optical axis, [m]

Y_R: Distance away from the nozzle exit at which the reattaching streamline exists (see Figure D.1), [m]

Z: Z-axis of the Coordinate system, [m]

Greek:

δ: Jet thickness, [m]

ΔP: Pressure difference acting on the jet, [Pa]

ΔT: Discharge-to-ambient temperature difference, [°C]

Δx: Difference in horizontal pixel number, [pixel]

Δx_L: Horizontal pixel count associated with the attachment length, [pixel]

Δy: Difference in vertical pixel number, [pixel]

η: Dimensionless similarity parameter

θ: Angle measured between the jet radius of curvature and the Y axis, [degrees]

θ_a: Angle between incident ray #2 and the normal to the air/water interface, [degrees]

θ_w:: Angle between refracted ray #2 and the normal to the air/water interface, [degrees]

ρ: Fluid density, [kg/m^3]

σ: Empirical constant related to the jet entrainment

List of Figures

Figure	Title	Page

Figure	**Title**	**Page**

List Of Tables

Table	Title	Page
C.5	Estimating the Uncertainty in the Attachment distance Measured from the Longitudinal Isothermal Data	124
I.1	Axial Images Measurements of the Jet-to-Wall Attachment	144
I.2	Cross-Sectional Measurements of the Jet-to-Wall Attachment	144
I.3	Isothermal Cross-Sectional Images Raw	145-149
I.4	Isothermal Cross-Sectional Images Processed Data	145-149
I.5	Isothermal Jet Axial Image Data	150-154
J.1	Flowmeter Calibration	158
J.2	Flowmeter Calibration Raw Data	159
K.1	Thermocouples Calibration	162
L.1	Isothermal Cross -Sectional File List	166
L.2	File List of the Cross-Sectional Buoyant Jet	166
L.3	File List of the Cross-Sectional Variable Flowrate Jet Images	167
L.4	Isothermal Axial File List	167
L.5	File List of the Axial Images of Buoyant Jet	167
L.6	File List of the Axial Variable Flowrate Jet Images	168

Acknowledgment

I would like to thank my advisor Dr. B.T. Beck for all of his help, suggestions, and support which made completing this thesis possible. Also, I would like to express my gratitude and thanks to Dr. B.W. Jones for accepting to be on my advisory committee and for his encouragement. I also like to thank Dr. M. Hosni for being on my advisory committee and for his support and encouragement. I also would like to thank Mr. Robert Handke, ME department network supervisor, for helping with the ME novel network and for allowing access for the needed disk space on the network.

Finally , my deepest appreciation goes to my parents and family for their financial assistance and encouragement during this study.

Chapter 1

Introduction

This chapter provides definition of the problem under investigation and a list of the research objectives. Background information about jet flows and a literature review are presented first.

1.1 Background

As a nozzle discharges a flow of fluid into a reservoir, the disturbance of the fluid at the nozzle outlet causes a change in the flow behavior as the fluid passes across the exit plane of the nozzle. The disturbance referred to here is the change of the boundary condition at the outer edge of the fluid. Inside the nozzle, the outer edge of the fluid has zero velocity caused by the wall presence. As the fluid leaves the nozzle, the wall no longer restricts the motion of the fluid. The flow behavior is influenced by the ambient fluid surrounding the nozzle exit. All flows of fluid discharged from a nozzle are classified as jets. Jets may be grouped into different categories according to the nozzle geometry, Reynolds number, ambient fluid, and the presence of a solid boundary in the jet vicinity. Different nozzle shapes also result in different flow behavior. The Reynolds number is used to classify whether a jet is laminar or turbulent. The ambient fluid influence on jet is based on the velocity, relative temperature, and/or the type of the ambient fluid. If the reservoir fluid is the same as the jet fluid, the jet is called a submerged jet. Temperature difference between the jet and the reservoir alters the jet trajectory. If no temperature difference exists between the jet and the ambient fluid, the jet is called an isothermal jet. Presence of a solid boundary near the jet also affects the jet development. If no solid boundary exists near the jet, the jet is called a free jet. The rest of this section contains some back ground about the submerged isothermal free jet. Also, information about solid boundary and non-isothermal effects are presented here.

1.1.1 The Submerged Free Jet

When a jet leaves the nozzle, the reservoir fluid in the vicinity of the jet moves in a tangential direction to the intermittent surface that separates between the jet fluid and the ambient fluid. The fluid away from the center of the jet moves to replace the fluid which is entrained in the jet. This entertainment generates a circulating motion in the surrounding reservoir fluid. The entertainment of the reservoir fluid expands the jets cross-sectional area and increases the jet mass flow rate Blevins(1984). The expansion of the jet causes the jet mean velocity to decrease.

The transition Reynolds number, from laminar to turbulent flow, for a submerged free jet is 30 for a submerged jet emerging from a plane nozzle and 1000 for a submerged free jet issuing from a circular nozzle Blevins(1984). The strongest difference between a laminar and turbulent submerged free jet is the rate of entertainment. The entertainment rate in a turbulent jet is much higher than that in a laminar jet. Schlichting (1979) obtained a solution for the axial and transverse velocity profiles of a laminar submerged free jet using a similarity parameter. Solving for the velocity profile of the turbulent submerged free jet requires a closure model for the Reynolds stresses, which is determined experimentally. The flow behavior of the turbulent submerged free jet is characterized by the core region, the transition region, and the fully developed region. The core region is a shear free region; it isusually called the potential flow region. This region extends between the nozzle exit and the position where collapse of the shear layers occurs; essentially a meeting of boundary layers extending from the nozzle wall. In the transition region the shape of the velocity profile starts approaching a Gaussian distribution. The jet becomes fully- developed when the velocity profile takes on this bell shape. In the fully-developed region, a similarity solution for the jet velocity profile is obtainable if the eddy viscosity is much higher than the kinematic viscosity of the fluid. The eddy viscosity is a measure of the jet entrainment; it is usually determined experimentally.

1.1.2 Solid Boundary Interaction

Solid boundary interaction with the jet depends upon the geometry of the solid boundary, its orientation, and its location with respect to the jet. Only a plane surfaces were considered in the present study. According to the location and orientation of the plane surface relative to the jet, three types of jets may emerge. In general the jet either discharges away from the surface, is directed towards it, or jet is parallel to it at an offset distance away. The first type of jet boundary interaction produces a wall jet. In the wall jet, the fluid is retarded by a rigid surface on one side and by still fluid on the other side. The wall jet is considered fully-developed when equilibrium exists between the shear layer adjacent to the solid boundary and the point at which the local velocity falls to half of the maximum local velocity. The boundary layer due to the wall jet is defined by the region between the solid boundary and the locus of points at which the velocity is maximum. The momentum of the wall jet is not conserved due to the shear stress applied by the solid boundary on the jet.

If the jet discharges toward the surface, it is called an impinging jet. The impinging jet may discharge normal to the surface, or at an angle. In the impingement region the static pressure rises well above the static pressure in the reservoir because of fluid deceleration caused by the solid surface. The impingement region is also characterized by a high connective heat transfer coefficient. As the fluid from the jet flows along the surface, it turns into a wall jet.

In the offset jet, the jet deflects toward the solid boundary and attaches itself to the boundary at some downstream location. The trajectory deflection of an isothermal jet is caused by the Coanda effects. Blevins (1984) defines the Coanda effect by " the tendency of a fluid to adhere to and flow around nearby solid boundaries". The phenomena is named after Henry Coanda who first observed it and used it in many of his inventions. The presence of a solid wall restricts the motion of the ambient fluid near the solid surface, preventing entrained fluid replacement, and creating a low pressure in the region between the inner edge of the jet and the solid boundary. The resulting net pressure force acting on the jet deflects the jet toward the wall. At the point of attachment, where the jet meets the wall, part of the jet flows forward and the remaining part flows back in the reverse direction. The fluid entrained from the low pressure bubble, trapped between the wall and the jet, returns back to the low pressure bubble at the attachment point. The flow field of an offset jet is divided into the region between the nozzle and the point of attachment, in which the jet acts like a free jet. Within the impingement region, the jet is similar to a tilted impinging jet. In the wall jet region, the flow adheres to the wall and may eventually detach at some further downstream location.

1.1.4 Buoyancy effects

A temperature difference between the jet and the ambient fluid induces a buoyancy force acting on the jet. The buoyancy force alters the jet trajectory. The magnitude and direction of the induced buoyancy force is related to the temperature difference. The buoyancy force may act upward or downward depending on the direction of the jet and the jet discharge-to-ambient temperature difference. Warmer jet fluid will be deflected upward, while cooler jet fluid will fall downward unless acted upon by another force. For an offset jet, warmer jet fluid shortens the attachment distance. Colder jet fluid increases the length of the attachment distance, if the jet remains attached to the wall. At some critical temperature difference, where the buoyancy force overcomes the Coanda force, the jet will detach from the wall to form a free jet.

1.2 Literature Review

Many researchers have studied the Coanda effect in relation to various applications. Bourque and Newman(1960) related their study to improving the scavenging of the internal combustion engine, augmenting the thrust of a nozzle with induced flow, and increasing the maximum lift coefficient of a wing. Sawyer(1960) related his study to sudden expansion in pipes and channels, flow over spoilers, and the wake of bluff bodies. Davis and Winatro (1971) studied the behavior of aircraft jet exhaust and its loading effect on the ground. Shakouchi and Onohara(1989) related their study to separating different particle sizes from each other. Smith and Hawkins(1991) investigated Coanda flare, a concept that utilizes the enhanced entertainment of ambient air to give more efficient combustion. Also, Coanda forces are significant in controlling the circulation of air movement inside ventilated rooms, and are an essential parameter for optimizing thermal comfort in air conditioned spaces. Several investigators have studied offset jets, and wall jets, in HVAC (Heating Ventilating and Air Conditioning) systems using high-side wall diffusers.

Some of the researchers, that investigated the behavior of a jet flowing nearby a solid surface, limited their investigation to one particular region of the flow. Others studied the entire span of the offset jet. Some of the researchers used slot diffusers, while others used circular nozzles. Most, if not all researchers investigated turbulent jet flows. Also, some researchers investigated buoyant jet flows, and the buoyancy effects on offset jet trajectory.

Dodds (1960) developed a theory, based on an approximate integral method, to predict the position of jet reattachment and the mean pressure in the separation bubble for an isothermal offset jet issuing from a slot nozzle. His theory postulated the existence of a force balance between the fluids on both sides of the jet and the induced centripetal force. The pressure difference in the fluid on both sides of the jet rises due to the decreased pressure in the gap between the jet and the wall, which is a result of the reduced fluid entertainment in the gap cased by the wall presence. The induced centripetal force is equal to the jet momentum divided by its radius of curvature. The jet radius of curvature was found from geometrical properties associated with the problem, in combination with a momentum balance applied at the point of reattachment. Dodds used a velocity profile similar to the velocity profile of a free plane jet. His solution was simplified by assuming that the radius of curvature of the jet and the mean pressure separation bubble to have constant values. He also did not account for pressure change caused by the jet impact on the wall. Dodds showed, through dimensional analysis, that the reattachment position becomes independent of the Reynolds number at high Reynolds number. Also he used dimensional analysis to show that the length of the plate had no effect on the reattachment position for a very long plate.

Bourque and Newman(1960) ran an experimental study of the reattachment of a two-dimensional incompressible turbulent jet to an adjacent flat plate. Their experimental results were in good agreement with the Dodds' theoretical predictions. Their experiments showed that the position of reattachment becomes independent of the plate length as long as the plate length exceeds 3.8 times the length of the attachment distance. Also they found that the flow becomes independent of the Reynolds number when the Reynolds number, based on the nozzle diameter, exceeds a threshold of 5500. They also found that the jet did not interact with the plate when the offset distance was 35 times bigger than the width of the slot at the Reynolds numbers that they used. They found that for a small nozzle to wall distance, the jet reattachment occurs when the sign of the pressure coefficient changes. They also investigated the effect of the plate tilt on the jet reattachment.

Sawyer (1960) conducted a study similar to that of Bourqe and Newmans's. He used a variable slot width and three jet-to-wall separation lengths, which enabled him to use a wide combination of gap-length to slot-width ratios. He did not investigate the effect of Reynolds number. He used a fixed Reynolds number of 4.9×10^4, at which the jet behavior is independent of the Reynolds number. He used pressure taps to measure the wall pressure, and observed that the wall maximum pressure coincided with the location of the attachment point. Sawyer (1963) modified the theory proposed by Dodds to account for the pressure loss in the impingement region, and to account for the different rates of entertainment on both sides of the jet. Also, he used a velocity profile similar to the velocity profile in a turbulent mixing layer to approximate the velocity distribution at the nozzle exit. Using a first order mixing length analysis, Sawyer showed that the velocity distribution of a deflected plane jet is not much different than the velocity distribution of a free plane jet. He observed that the deflected jet maintained a symmetrical velocity spread. However; the maximum cross-sectional velocity decreases more rapidly in the offset jet. Sawyer found that curvature had a big influence on jet entertainment properties. Also, he studied the influence of the wall tilt on the jet.

Newman and Patel(1971) conducted an experiment in which they measured pressure and velocity profiles in an offset jet issuing from a circular nozzle. They used water and air as working fluids. In the apparatus using air, they used a 1040 mm long plate, a 3.175 mm nozzle, and a 3.175 mm high nozzle-to-jet offset. In the apparatus using water as the working fluid, the plate length was 1520 mm, the nozzle diameter was 2.0 mm, which was about 3/5 of the nozzle diameter in air apparatus, and the gap height was 2.0 mm. The average nozzle velocity used in the air apparatus was about 1/50 of the velocity used in the air apparatus. The Reynolds number range in the water apparatus was between 2800 and 16,400. They also measured the normal and lateral growth scales of the emerging three-dimensional wall jet, and compared the measurements to an approximate theoretical prediction. Their approximate theory predicted that the normal growth scale was 1/25 of the axial distance, the lateral growth scale was about 1/3 of the axial distance. It was proven, from their experimental results, that the growth rate in the lateral direction was about 7 times larger than the growth rate in the normal direction. Their results also showed that the rate of the jet growth normal to the plane wall was less than that for a two- dimensional jet.

Koyozo Ayukawa and Toshihiko Shakoughi (1976) investigated the oscillation of a two-dimensional jet attaching to a plane wall undergoing periodic infinitesimal fluctuation of the pressure within the separation bubble. They used 3 mm width nozzle and a 45 mm jet to wall distance. They used velocities between 10 m/s and 40 m/s, and pressure fluctuations between 3.8 Hz to 8 Hz. Their main conclusion was that the oscillation of the attachment point has no resonance. The amplitude of the oscillation decreased with increased frequency in the pressure fluctuation. Oscillations had larger phase lag and smaller amplitude as the frequency of the fluctuation increased.

Marster (1978) studied the effect of ventilation on a plane jet offset from a flat plate. Ventilation was allowed through a gap between the nozzle and the wall. He used two plate lengths; one plate was 12.7 cm long, and the other was 25.4 cm. He used a 2.54

cm wide slot-nozzle. He investigated several gap settings, with an average nozzle velocity equal to 75 m/s. The plate was parallel to the wall in one of the experiments, and subsequently he used three inclination angles of 30 degrees , 45 degrees, and 60 degrees. The pressure profile in the pre-attachment region decreased rapidly at first, then held a constant value, followed by a rapid increase to the maximum pressure and a subsequent recovery to the ambient pressure. In the deflected jets, the point of reattachment moved further downstream, and the point of maximum pressure became less well-defined. Marster concluded that the forces generated in the flat surfaces are significant, and that a sizable fraction of the jet momentum is recoverable in terms of a force normal to the jet axis.

Davis and Winarto (1980) studied the effect of varying the gap height of an offset jets issuing from a circular nozzle. They used a 1.7 m long plate, a 25.4 mm diameter nozzle, and 100 m/s average nozzle velocity. They used three ratios of gap height to nozzle diameter: 0.5,1.2, and 4. It was found that the jet-to-wall space changed the location of the region at which the jet interacts with the wall. If the offset distance was greater than 2.6 nozzle diameters, the jet interacted with the plate in the self-preserving region. If the attachment distance was less than 2.6 diameters, but greater than 1.2 diameters, the attachment occurred at the transition region where more rapid diffusion of the jet took place. They found that increasing the wall-to-jet space moved the apparent origin of the emerging wall jet further away from the nozzle. They also measured the velocity profile at some stations away from the exit of the jet, which showed the shape of the jet in that region of the flow.

Hoch and Jiji (1981) investigated the effects of the ambient motion on a two-dimensional turbulent offset jet, using a low speed wind tunnel facility. They tested two nozzle diameters of 0.26 in and 0.46 in. They also used three nozzle-to-jet spacings: 3 in., 5.7 in, and 8.7 in. They used a mean average nozzle velocities between 10 to 12 fps, and the ambient velocity values they used were 0, 0.25, and 0.1 fps. They modified the theoretical solution proposed by Dodds(1960), and assumed appropriate velocity profiles in the pre-attachment region, in the impingement region, and in the wall jet region. Then they applied momentum and mass flow balances at the points of transition from pre-attachment to impingement region, and at the point of transition from the impingement region to a wall jet flow. They also relaxed the assumption of constant radius of curvature for the jet. They assumed a fifth order polynomial and applied appropriate boundary conditions to define the unknown coefficients. Also, unlike Boroque and Sawyer, they allowed the pressure in the separation bubble to vary rather than assuming it to be constant. They used the measured pressure at the wall and they assumed the pressure to vary linearly in the wall jet region and the pre-attachment region.

El-Taher(1980) investigated a two-dimensional ventilated offset air jet. He used a 450 mm long plate, 3 mm wide slot nozzle, and 60 m/s average nozzle velocity. The apparatus had a relatively small gap-to-slot ratios; the gap-to-slot ratios were 2 and 4. El-Taher(1983) investigated the effect of wall curvature on the characteristics of a wall air jet. The nozzle diameter and velocity were similar to that given above. He used four wall test models; one model was a flat plate, while the others had radii of curvature of 300 mm, 400 mm, and 900 mm. He found that the rate of entertainment through the gap increased as the curvature of the surface increased, and the point of re-attachment moved closer to the nozzle. Wall pressure only had an effect on the flow in the pre-attachment region.

Recently a lot of theoretical and experimental studies have been directed toward air diffusion process. Recent theoretical analysis focused on a numerical solution of the Navier-Stokes equations. Several turbulence closure models have been presented in the literature. Murkami etcal (1989) used the k-epsilon two equation model to incorporate the effect of turbulence on room air diffusion. Murakami et al (1992) used a second-moment closure model. Experimental studies became necessary for validating the numerical models. Hawkins (1995) provided a good review of the experimental work conducted on room air diffusion. Hawkins ran experimental work in which he measured three- dimensional velocity and temperature profiles in an isothermal and non-isothermal ventilated room. Also, many researchers have pointed out the importance of running scaled experiments since smaller room sizes minimize the experimental costs and reduce computation time. Zhang et al (1991) ran a scaled experiment using a 1/4 scaled model, with the same nozzle geometry and Reynolds number in the model and in the prototype. He found that the velocity profiles and the turbulence characteristics in the model were substantially different from the velocity profiles and the turbulent characteristics in the prototype. Awbi (1990) showed that, for complete similarity between the model and the prototype, there must be similarity in Re, Ar, Fr, and Pr. Zhang(1991) pointed out that complete scaling is not possible in non-isothermal air diffusion. He proposed a new similitude modeling technique based on using the Ar number and he also defined a critical Ar number. Discrepancies between scaled and full-scale non-isothermal room air diffusion test results indicate the need for running additional scaled experiments to investigate the full effect of scaling on room air diffusion phenomena.

1.3 Objectives

The purpose of this investigation was to conduct qualitative (flow visualization) and quantitative experimental investigation of a submerged offset laminar water jet issuing from a round nozzle (circular aperture). The wall presence was expected to lead to the jet deflection and reattachment to the wall. The main focus of the present study was to observe how the adjacent wall influenced the jet development, and to measure the effect of the gap height on the length of the reattachment distance for an approximately isothermal jet. Images of the jet cross section at certain stations away from the plane of the nozzle exit were obtained experimentally. Also, images along the jet axis were acquired. Measured reattachment lengths were compared to a simple mathematical model for an isothermal jet. Flow visualization images were taken to look at the effect of buoyancy on the jet trajectory and cross-section. Qualitative images of the jet showing the effect of turbulence on the jet behavior were also obtained. The major tasks to be accomplished were as follows:

- Produce flow visualization of the isothermal submerged laminar round offset jet cross section and central axial plane.

- Measure the attachment distance of the isothermal submerged laminar round offset jet for different gap heights.

- Measure the normal and lateral growth rates of the isothermal submerged laminar round offset jet for different gap heights.

- Produce flow visualization of buoyant submerged laminar round offset jet cross section and central axial plane using negative and positive temperature difference between the jet and the ambient water.

- Produce flow visualization of the submerged round offset jet cross section and central axial plane using three different flowrates, one in the laminar range and two higher flow rates.

Chapter 2

Experimental Setup

To produce the flow visualization of a circular jet discharging parallel below a smooth flat plate, the experimental setup shown in Figure 2.1 was designed for obtaining both cross-sectional and axial images of the jet. The experimental setup consisted of the jet apparatus, the water circuit, the light illuminating system, and the image grabbing hardware. The experimental setup produced a jet discharging near the top of a 10 gallon aquarium tank using a 0.500 in OD, 0.473 in ID smooth brass tube as a nozzle. The test apparatus was enclosed inside the ten gallon aquarium tank shown in Figure 2.1. Water circulated through the apparatus by a pump. A flow meter and a gate valve were necessary to monitor and control the water flow rate at the nozzle. The copper coils shown in Figure 2.1 were immersed in a water bath for controlling the temperature of the water at the nozzle of the jet. All of the water circuit elements were connected together by 0.5 inch reinforced nylon hose. The light illumination system consisted of a laser source, a light sheet generating optic, and a manual traverse. The image grabbing hardware consisted of a CCD camera, a frame grabber board, a personal computer, and a VCR. Figure 2.2 shows the orientation of the jet and apparatus with respect to the CCD camera field of view for both the cross-sectional and the axial images of the jet. Also, Figure 2.2 shows the relation between the jet images and the global coordinate system that was adopted. The origin of the coordinate system is at the point where the vertical line that passes through the nozzle center crosses the Plexiglas plate representing the ceiling. The x-axis goes from right to left, the y-axis runs from top to bottom, and the z-axis points a way from the center of the jet such that the coordinate system is right handed.

A laser-generated 10 mw light sheet illuminated the flow field inside the test apparatus. Approximately neutral buoyant TiO_2 particles were injected into the flow to trace the jet trajectory and scatter light toward the CCD camera. The images sensed by the camera are transmitted through a cable into the frame grabber or, alternatively, into a VCR. Dynamic images were recorded by the VCR and still images were digitized by the frame grabber board which was controlled by a computer.

2.1 Test Apparatus

The experiment simulated to some extent room air diffusion from a wall diffuser offset from the ceiling. The working fluid utilized in this experiment was water instead of air. Of course water is not used in air conditioning. However, it is convenient for test purpose, it allows for a smaller test apparatus, and it is easy to seed for flow visualization purpose. The apparatus was mounted inside a ten gallon glass aquarium tank. The tank was 10 in wide, 12 in high, 20 in long, and it had 1/8 in thick clear glass walls. The test chamber was constructed by partitioning the tank using Plexiglas materials. Figure 2.3 shows the Plexiglas fixtures and how they were mounted inside the tank. The various components of the test apparatus are described in more details in the rest of this section.

2.1.1 Base Platform

The platform was made of 10 in x 12 in, 3/16 in thick Plexiglas plates. It was elevated over the tank floor on top of four 2 in x 1.5 in, 0.5 in thick Plexiglas feet. For details and dimensions of the base platform, see Figure 2.4. The purpose of the platform was to reduce the effect of water circulation on the jet trajectory. Also, it held the intake in place, and separated the open chamber region containing the jet from the intake line. The intake tube was clamped inside 2 in x 0.75 in x 0.5 in Plexiglas support blocks with 0.5 in diameter holes bored in their centers. These intake supports were bonded with Plexiglas adhesive to the bottom surface of the platform such that their centers were aligned with the platform center. One of the intake Plexiglas supports was mounted ½ in from the front end of the platform and the other was mounted 4 in away from the first supporting block.

The platform was secured in place using 2 in x 1.5 in, 3/16 in thick hard rubber sheets. Each rubber sheet was attached to the end of 0.25 in nylon screws that penetrated through one of the platform's feet. The positions of the plastic sheets were adjusted so they contacted the wall of the tank and wedged the platform in place so that it remained fixed in position.

2.1.2 Top Partition

The top partition was a right angle corner that formed the ceiling and the back wall of the test chamber. Both the ceiling and the back wall were made of 3/16 in thick Plexiglas. They were bolted together with 3/16 in fine thread screws. Figure 2.5 contains the dimensions and details of the top partitions. The ceiling was a 15 in x 7 in, ¼ in thick

Plexiglas plate. Two 11.75 in x 0.75 in x 0.5 in thick Plexiglas studs were bonded near the edges of the top surface of the ceiling. They were oriented along the longer dimension of the ceiling to improve the ceiling rigidity and minimize any possible deflection or warpage. Two T-shaped white plastic pieces were used to suspend the ceiling inside the tank. The plastic hangers were bolted to 6 7/8 in x 13/16 in, ¼ in thick Plexiglas pieces that were glued to the top surface of the ceiling. The hangers rested on the plastic lip edges of the tank top for positioning the top partition. The effective ceiling length was 13 in.

The back wall was the vertical wall of the chamber from which the jet was discharged. The height of the vertical back wall varied somewhat depending on the number of spacers that were used to position the jet away from the top wall. When no spacers were used, the back wall was 4 in high, and its width was fixed at 7 7/8 in A ½ in diameter hole bored in the vertical mid-plane of this wall 3/8 in beneath its top allowed for insertion of the nozzle. A 7 7/8 in x 1 ¾ in, ¼ in thick Plexiglas plate was bonded perpendicular to the back surface of the vertical wall and flushed with its top end. This helped in aligning the back vertical wall with the ceiling. The alignment plate had a 3/16 in diameter hole bored on each side of its center, located 1 in away from the center of the plate. Another 5 in x 1 ¾ in, ½ in thick Plexiglas block with a ½ inch hole bored in its center was bonded to the back surface of the back wall directly under the Plexiglas alignment plate. Also, this block had 3/16 in diameter holes bored 1 in away from its vertical mid-plane. The purpose of this block was to provide support for bolting the ceiling to the vertical back wall of the test apparatus. Also, it clamped on the nozzle and secured it in place.

2.1.3 The Nozzle

The jet nozzle was made from 0.5 in OD, 0.473 in ID smooth brass tube mounted flush with the back wall of the test chamber. As shown in Figure 2.6, the nozzle assembly consisted of a 3.25 in high vertical brass tube that was connected by a 0.5 in brass elbow to a 0.5 in diameter, 2.125 in long horizontal flow straightening section. The flow straightening section was coupled into another 0.5 in, 3.5 in long brass tube by a 0.5 in copper coupling. The flow straightening section consisted of three 0.220 in OD, 0.190 in ID, 2.125 in long brass tubes embedded inside a 0.5 in OD, 0.473 in ID, 2.125 in long brass tube. The presence of the three tubes in the flow straightening section was to attenuate secondary flows induced by the flow going around the elbow prior to the flow entering the nozzle. The exit end of the nozzle was carefully filed and sanded flat on the end with #400 sanding paper to remove any burrs in the exit plane. The whole assembly was soldered together to form a single unit.

2.1.4 The Intake

The intake line was 7 in long and was also made from a 0.5 in OD, 0.473 in ID smooth brass tube. It was mounted under the platform, and inserted in the into 0.5 in flexible plastic hose the leads to the pump intake.

2.2 Water circuit

As Figure 2.1 shows, the water inside the apparatus circulated from the intake of the return to the jet discharge. Components of the water circuit were a Teel Model 1P677 pump, a water filter with bypass attachment, an F&P Model 10A3555 rotameter type flowmeter, a 10 ft of 0.5 in OD copper coil immersed in a water bath, a throttle valve, and 0.5 in reinforced clear PVC hose. The intake port of the filter was connected by 0.5 in reinforced clear PVC hose to the intake of the return line inside the tank. The filter output lead was similarly connected to the intake port of the pump and the pump outlet was discharged to the input port of the flowmeter. As the water came out of the flowmeter, it passed through the 10 foot long, 0.5 in OD copper coils which were placed inside a 5 gallon, 12 in diameter plastic bucket. The water coming out of the copper coils was directed by 0.5 in reinforced clear PVC hosing to the nozzle assembly. The water circuit provided control over the speed and temperature of the water at the plane of the jet discharge.

2.2.1 Flow Rate Control

An F&P Model 10A3555 flowmeter was used to monitor the nozzle discharge water flowrate. The flowmeter range was 0 to 0.81 GPM with a 1% resolution. The flowmeter normally is repeatable to within 0.1-0.2 division, but no measure of flow rate was available on the flow meter near the mark that the float indicated during the laminar jet tests. Therefore it was necessary to calibrate the flow meter for these low flow tests. The flowmeter was calibrated to within ± 1.7% using the volume collection method. Details of the flowmeter calibration are in Appendix J. The flow rate was controlled by adjusting a globe valve mounted at the flowmeter exit.

2.2.2 Temperature Control

The copper coil, immersed in the water circulating through the plastic bucket, provided the heat exchange mechanism that was necessary for controlling the temperature at the nozzle discharge. Controlling the temperature at the nozzle discharge was done by adjusting the temperature of the water in the plastic bucket. The temperature of the water in the plastic bucket was adjusted by circulating tap water through it. No control was established over the temperature of the ambient water inside the tank. For adjusting the temperature difference between the jet discharge water and the ambient water, the temperature of the jet discharge water was adjusted to the appropriate setting in accordance with the ambient water temperature.

Type T # 24 gage thermocouple junctions, along with a Doric 403A digital temperature indicator and rotary selector switch, were used for monitoring the temperature at six points inside the experimental apparatus. Also, the temperature of the water circulating through the plastic bucket was monitored during tests. The thermocouple, used for monitoring the discharge temperature, was installed 2-3 in inside the 0.5 in reinforced clear PVC hosing leading to the nozzle assembly. Thermal analysis of the discharge temperature measurement is included in appendix K, along with the thermocouple calibration and uncertainty analysis for the temperature measurements that were made. The thermocouple measuring the intake of the return line temperature was installed about 5-6 in inside the intake tube. The ambient water temperature was monitored by four thermocouples that were located along the sides of the test chamber so they would not disturb the jet. The thermocouple junctions measuring the ambient temperature were placed about 2-3 inches in front of the vertical back wall of the test chamber. Two of those thermocouple junctions were placed about 1 inch below the ceiling (one on each side of the jet), each protruding about 1 inch inside the test apparatus. The remaining two thermocouple junctions were installed on both sides of the chamber 1 in above the base platform of the test apparatus. The absolute temperature measurement was accurate to within about ±1.0° F. Details of the thermocouple calibration are given in appendix K. The temperature control arrangement did not provide control over the discharge temperature, but it did allow for control over the temperature difference between the jet discharge temperature and the ambient temperature within (±0.2F).

2.3 Flow Field Illumination

A laser-generated light sheet was used for illuminating the flow field. The light sheet was moved on a manually-operated traverse to allow visualization of different slices of the flow. Also, it was necessary to inject seeds in the jet for it to become visible. When the seeding particles scatter the light incident on them from light the sheet, a thin slice of the flow in the plane of the light sheet could be visualized.

2.3.1 Laser Generated Light Sheet

A 10 mw, 632.8 nm wavelength 124B He-Ne STABLEITE Spectra Physics laser source was used for illuminating the flow. Specifications of the laser source are summarized in Appendix G. A line generating (cylindrical) lens placed in front of the output of the laser, transformed the laser beam into a light sheet. The divergence angle of the resulting line was 60 degrees. The length of the emerging line increased approximately linearly with distance from the cylindrical lens, and the nominal width of the light sheet was about 1 mm. The intensity of the laser light drops off as the light moved further away from the cylindrical lens, because the power is distributed over a bigger area. Thus, it was desirable to minimize the distance from the laser to the seeded region of the jet for maximizing the intensity of the image. Alternatively a focusing cylindrical lens could be used to collimate the sheet.

2.3.2 Seeding the Flow

Titanium dioxide particles (1.5-2.0 μm) were used to seed the flow. The titanium dioxide seeds were first mixed with water to form a suspended solution. Titanium dioxide particles are not quite neutral buoyant but they have a small settling velocity (a few microns/sec) and they therefore approximately trace the path of the jet. The titanium dioxide/water solution was injected by a syringe needle attached to a 1/8 in clear nylon tube whose output was inserted about 5-6 inches inside the intake of the return line. The system was drained and refilled periodically to prevent filling the whole tank with seed material. The filter was used occasionally to filter out the seed when the seed concentration in the system after use was not very high.

2.3.3 Traversing the light sheet

The traverse platform moved by means of a 32 in long, ¾ in diameter lead screw, which had a pitch of ten threads per inch. See Figure 2.1 for a diagram of the traverse. The end support of the traverse was clamped between two 1.5 in x 1.5 in x 36 in long

Unistrnt channels that were bolted to a 36 in x 1 in x 0.75 in wooden press-board base. The platform of the traverse was bolted to two 1.5 in x 1.5 in x 20 in long Unistrnt channel supports. A 20 in x 11 in x ¾ in press-board wood base was bolted on top of the C-channel supports. The total horizontal travel of the traverse was 88.5 turns which translated into 8.85 in This apparatus allowed traversing the light sheet along the jet both axes for obtaining cross-sectional and axial images of the jet.

2.4 Image Grabbing Hardware

The image grabbing hardware provided the ability to record still or dynamic images. The still image acquisition setup consisted of a digital camera, a frame grabber, and a personal computer. The still image dimensions were determined by first calibrating the CCD camera. Both quantitative and qualitative information about the jet trajectory and dimensions were available from the still images of the jet. The dynamic images were recorded by a VCR, and provided qualitative information about the jet. No calibration was made to determine the dynamic image dimensions. Both the axial and cross-sectional shapes of the jet were obtained in the tests.

2.4.1 CCD Camera

The camera used for imaging the jet was a TM-7EX miniature, high resolution CCD camera. A summary of the CCD camera specifications are given in Appendix E. The CCD camera was used with a 12 mm focal length focusing lens, which allowed close positioning of the camera near the flow field. For sharp images, the camera lens was manually focused on the jet prior to image grabbing. The camera was equipped with an AGC (automatic gain control) selection switch, which could be set for automatic gain of fixed gain. Also, the camera had a gamma (sensitivity) adjustment switch that could be set either to 0.45 or 1. The camera had a substrate drain type variable electronic shutter, which was capable of shutter speeds ranging from 1/60 to 1/10,000 sec in discrete steps. Spatial resolution of the camera images was determined from calibration tests (See Appendix A for details of the camera calibration).

2.4.2 Frame Grabber

The output signal of the CCD camera was connected to the 512 x 512 x 8-bit DT-2861 arithmetic frame grabber bored that was installed on a Data-Store 386 PC. The frame grabber had 4 Mbytes of on board frame-store memory used for storing sixteen 512 x 512 x 8-bit buffers. Through its arithmetic logic unit (ALU), and input look-up tables, the frame grabber was capable of acquiring images and performing arithmetical and logical operations on them at a 30 frames/second rate. With its flash A/D convector, the frame grabber digitizes the video input signal into an 8-bit pixel value representing 256 possible gray levels. Digitization of the video input signal to the frame grabber was done in an interlaced format. As an image is being acquired, the aperture of the camera opens for 1/60 second during which the even rows of the images are obtained. Within the next 1/60 second, the odd rows are obtained. Even and odd rows are then added together to produce an interlaced image. The frame grabber specifications are summarized in Appendix F.

2.4.3 VCR Recording

VCR recording was done by directing the CCD camera output signal into a VCR recorder. The CCD camera signal had to go through a modulator which condition the CCD camera signal to make it compatible with the VCR. The modulator device was internal to the Sony black and white monitor that was used to see the image view field of the camera. Still images from the VCR taping were displayed on a television screen by stepping through the frames. Pictures of the jets were then simply photographed from the television screen.

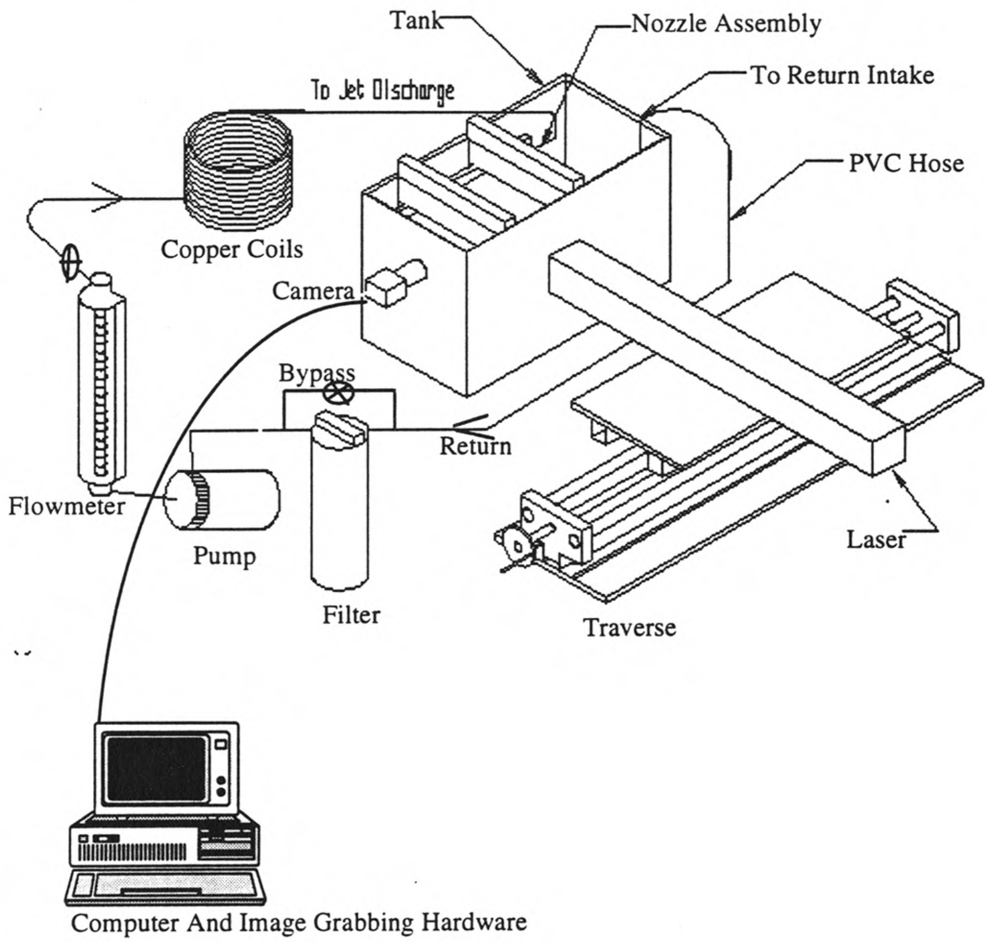

Figure 2.1: Experimental Setup

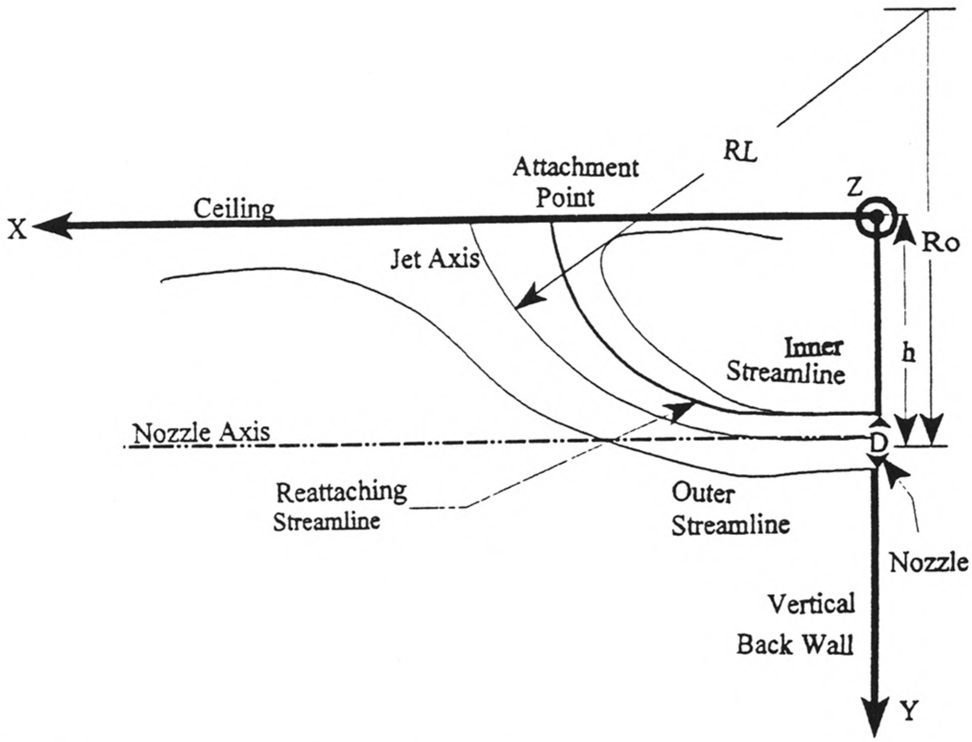

Figure 2.2 (a): Coordinate System for the Axial Images

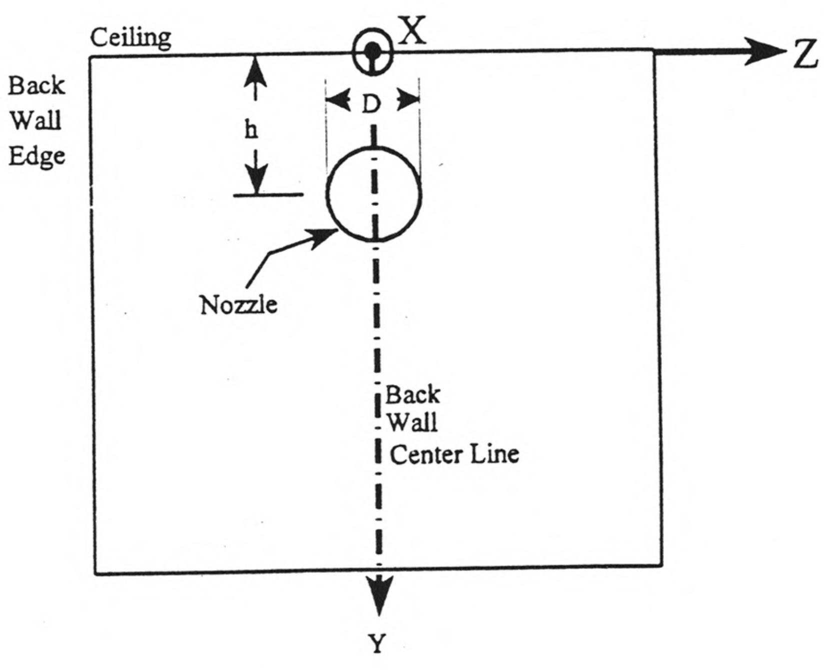

Figure 2.2 (b): Coordinate System for the Cross-Sectional Images

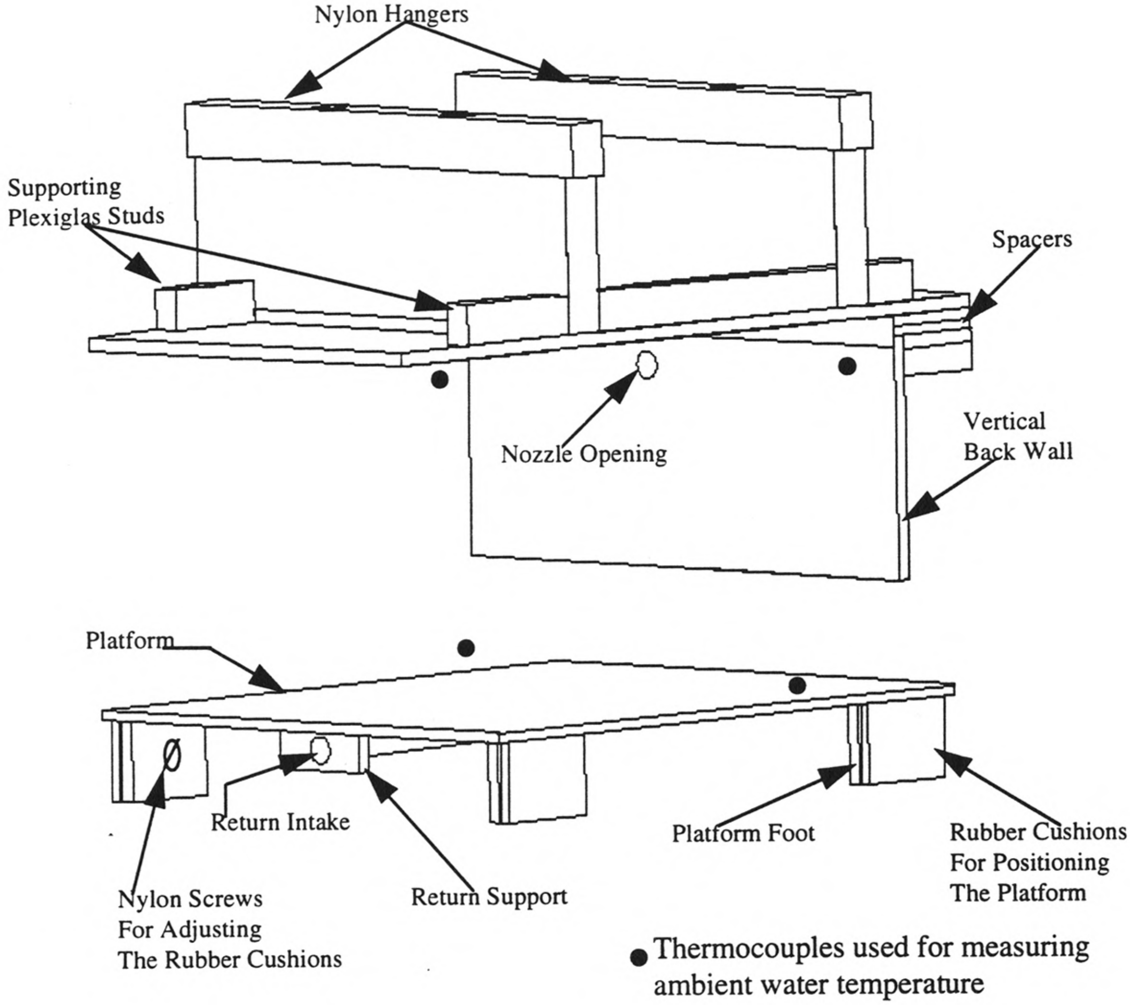

Figure 2.3: Plexiglas Partitioning of the Tank

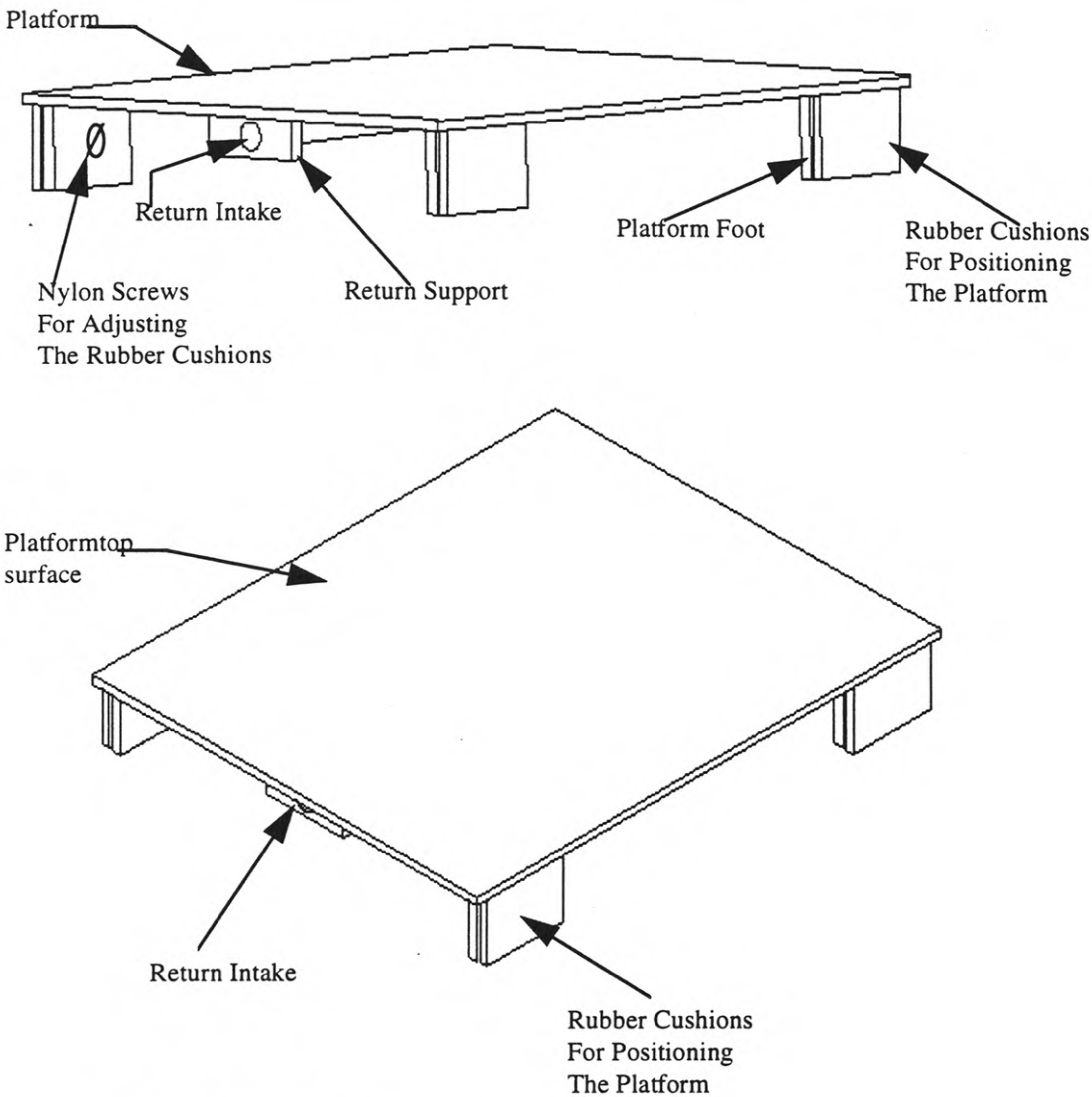

(a): Platform Three-Dimensional Views

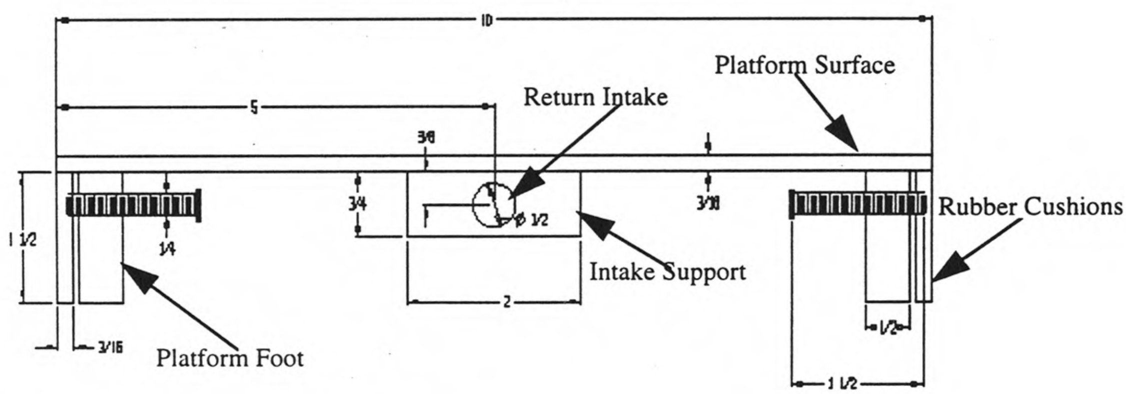

(b) : Platform Front View

Figure 2.4: Diagram of the Platform

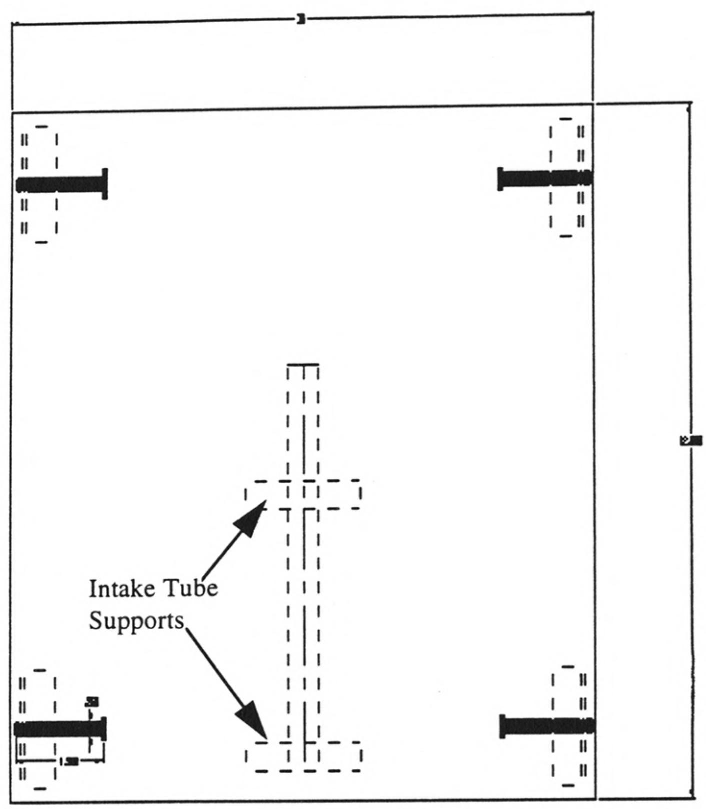

(c) Platform Top View

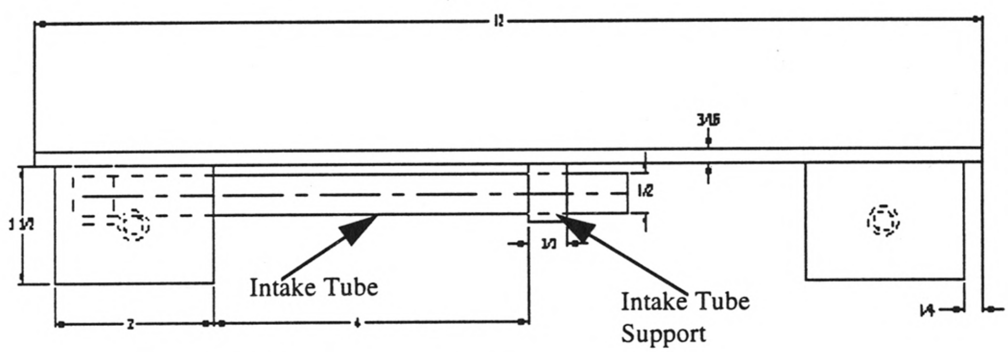

(d): Platform Side View

Figure 2.4: Diagram of the Platform (continues)

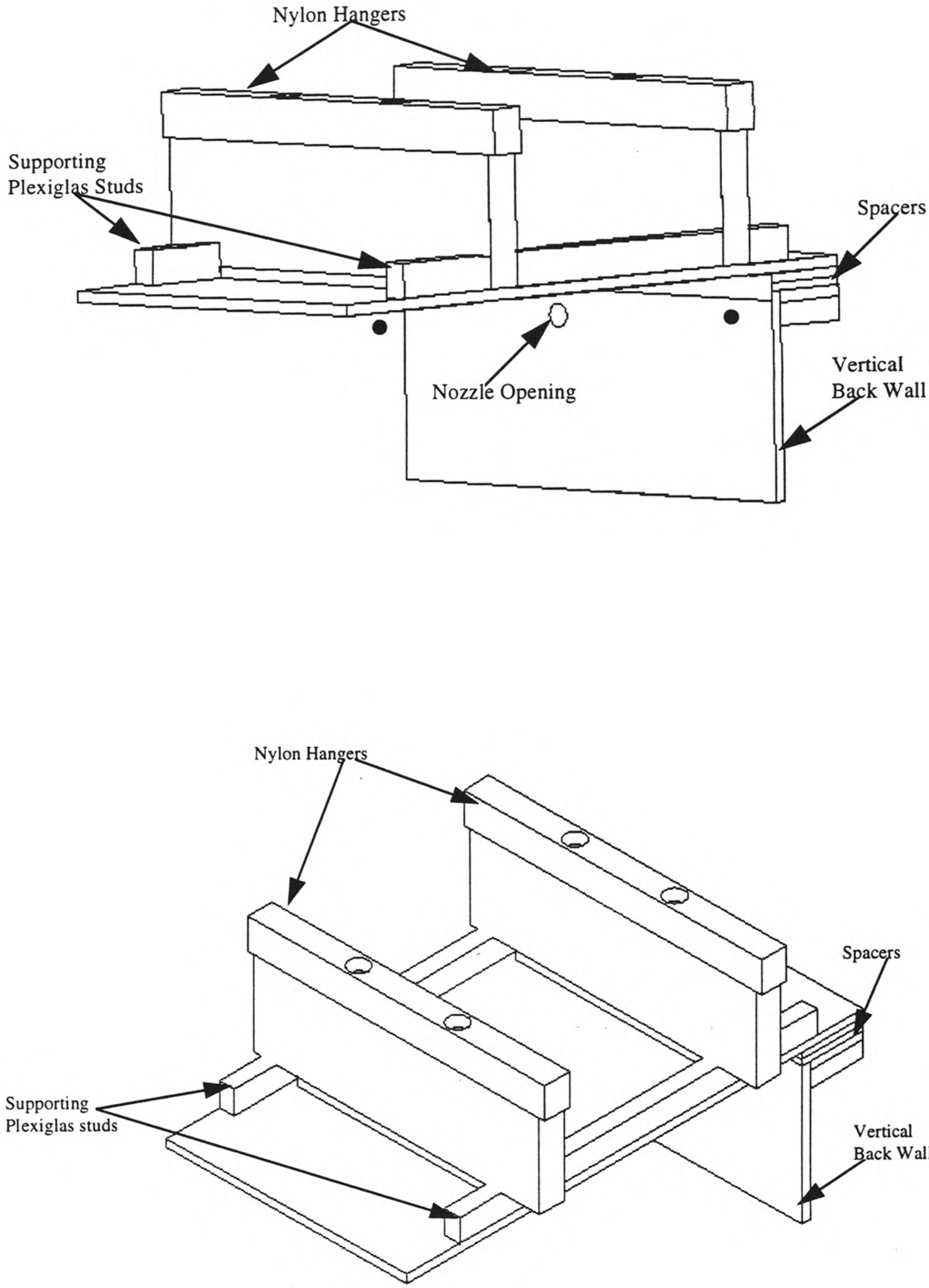

(a) Three-Dimensional Views

Figure 2.5 : Diagram of Plexiglas Partition

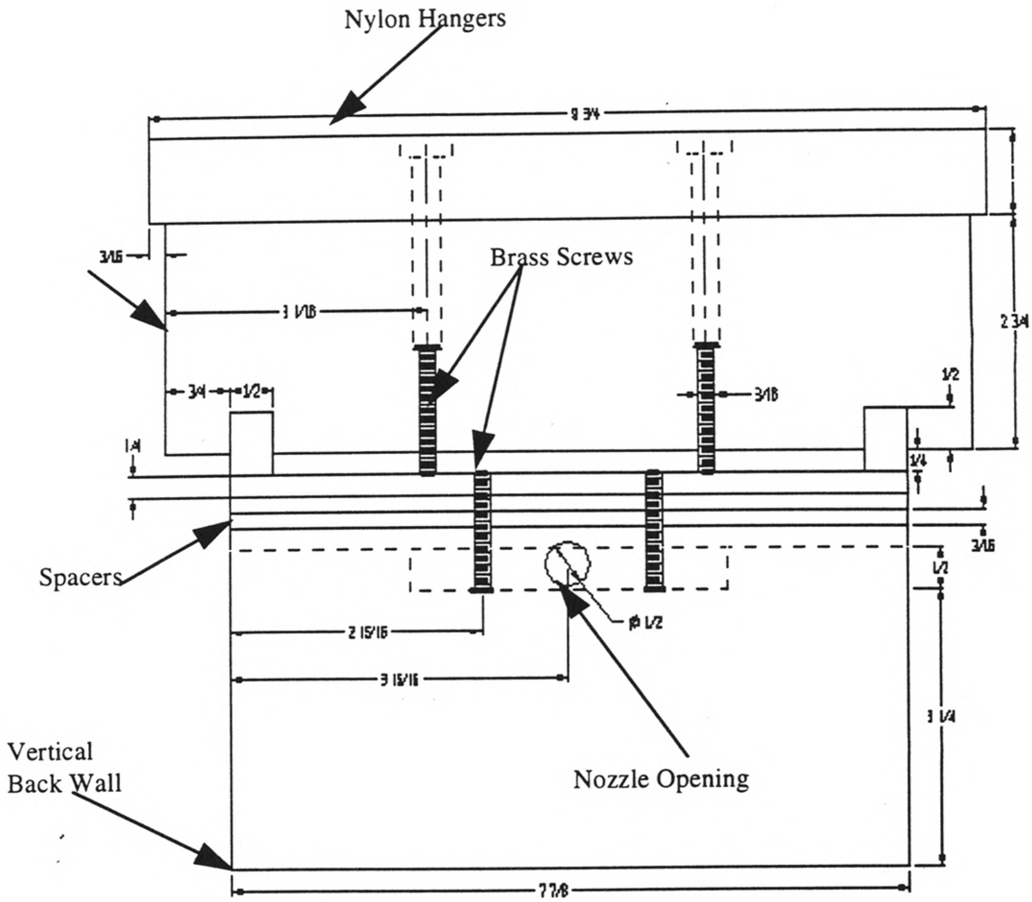

(b): Plexiglas Partition Front View

Figure 2.5 : Diagram of Plexiglas Partition (Continues)

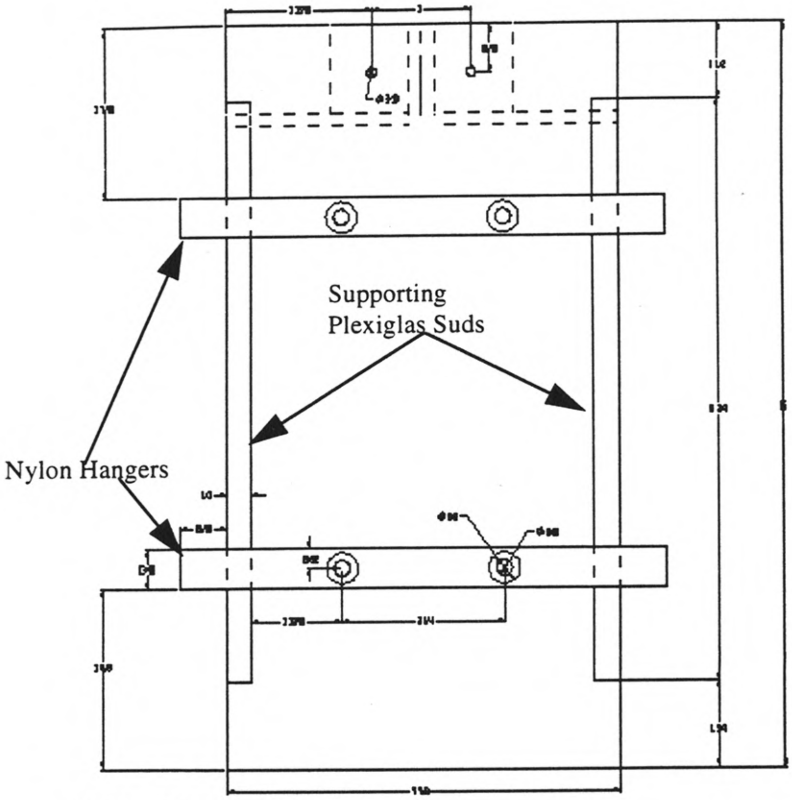

(c): Plexiglas Partition Top View

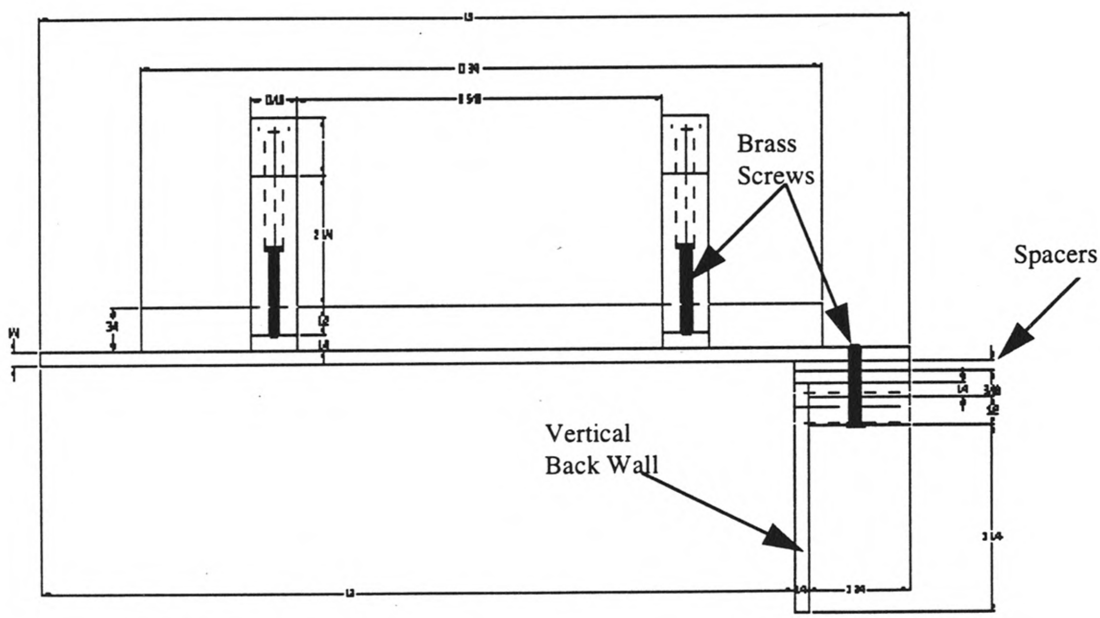

(d): Plexiglas Partition Side View

Figure 2.5 : Diagram of Plexiglas Partition (Continues)

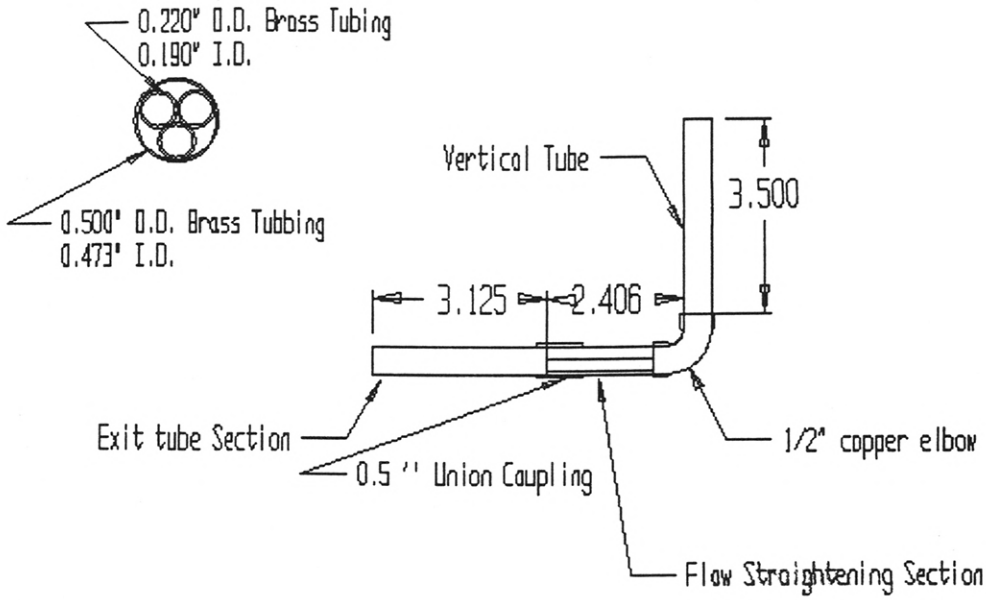

Figure 2.6: Nozzle Assembly

Chapter 3

Test Procedure

The experimental procedure consisted of calibrating the measurement instruments, actual running of tests, and subsequent image processing.

3.1 Calibration

All measurement systems used in the experiment were calibrated prior to actual tests. The flow meter was calibrated to within ± 1.7% using the volume collection method. Appendix J contains all details of the flow meter calibration. The thermocouple junctions were calibrated against each other to estimate the uncertainly in measuring the temperature difference between the water at the nozzle discharge and the ambient water inside the tank. Although the uncertainty associated with the single point absolute temperature measurement was within about ± 1.0 °F, the uncertainty associated with measuring the temperature difference was estimated to be about ± 0.2 °F. This is because the bias error associated with the thermocouple wire is offset some when calculating the temperature difference. A summary of the thermocouple calibration is in Appendix K. Calibrating the camera provided the size of the image pixel for locations inside the water tank at a certain distance away from the camera. The camera calibration provided vertical and horizontal scale factors for each image. Determining object or spatial dimensions from an image was achieved by measuring the image dimensions in pixels and multiplying the corresponding number of pixels by the appropriate image scale factor according to the following Equations:

$$O_h = k_x I_h \tag{3.1}$$

$$O_v = k_y I_v \tag{3.2}$$

Where O_h and O_v are the object horizontal and vertical dimensions, k_x and k_y are the horizontal and vertical image scale factors, I_h and I_v are the horizontal and vertical image dimensions measured in pixels. A separate calibration was made for the axial and cross-sectional images of the jet. Appendix A contains all details of the camera calibration. The uncertainty in the image scale factors was within ±6%. Uncertainty analysis of the image scale factors is presented in Appendix C.

3.2 Test Procedures

Running each test required assembling or adjusting the experimental apparatus, setting up the proper experimental conditions, and acquiring the images. The following sub-sections describe each aspect of the test procedure in detail.

3.2.1 Assembling experimental set up

Assembling the experimental setup involved physically setting up the apparatus assembly, hooking up the water circuit, and aligning the laser source and camera with respect to the apparatus. Before setting up the apparatus, a very important step for obtaining clear images was to ensure that the walls of the tank were clean. Then, the tank was filled with fresh tap water and left for about 2 hours to allow for the air bubbles dissolved in the water to come out of solution. This also allowed for the temperature of the water inside the tank to come into equilibrium with the room environment. Some of the air bubbles left the solution through the top surface of the water. The rest of the air bubbles tended to stick to the walls of the tank. All of the air bubbles stuck to the tank walls (including surfaces of the Plexiglas corner) had to be wiped off, otherwise they would have distorted the image, or possibly alternate the distribution of the flow.

3.2.1.1 Aligning the Laser and Camera with Respect to the Tank

Initially, the laser was aligned with respect to the tank while the tank was empty. The traverse was first set to the starting position, after which the laser was positioned on top of the traverse such that the laser axis was normal to the tank wall facing the laser. A square was used to align the laser axis approximately normal to the wall of the tank. For the cross-sectional jet images, the laser axis was normal to the nozzle axis. For the axial jet images, the laser light sheet source was oriented vertically such that its axis coincided with the nozzle axis. The laser-to-tank distance varied between the cross-sectional jet images and the axial jet images. For the cross-sectional case, the laser was placed such that the front face of the light generating optic was about 7.25 in away from the wall of the tank facing it. For the axial case, the laser displacement from the tank was about 2.75 in away, measured from the tank wall to the front edge of the light generating optic. After the test apparatus was assembled inside the tank, the laser/tank alignment was re-adjusted.

The camera position with respect to the tank was adjusted only after assembly of the apparatus. For the cross-sectional tests, the camera was facing the nozzle discharge. and the camera optical axis was aligned with the nozzle centerline. Figure 3.1 (a) contains an image of the camera alignment for the cross-sectional case. For the axial case, the camera was aligned such that its field of view covered the region of interest inside the tank. For the tests which acquired axial profile images of the jet (in the cases where ceiling-to-nozzle heights were between 6/16 in and 9/16 in) the camera field of view covered about 6.5 inches in front of the back wall of the test chamber. In the tests using 2,3 and 4 spacers, the field of view covered 8.0 inches in front of the back wall of the test chamber. Figure 3.1 (b) show the camera field of view for the axial images.

3.2.1.2 Assembling Apparatus and Water Circuit

Assembling the apparatus and the water circuit, as shown in Figure 2.1, started by inserting the 1/8 inch nylon tube, which was connected to the seed injecting needle, about 8-10 inches inside the return tube. Then, the intake line was held at the bottom of the tank and the Plexiglas platform was tightly fixed in position, such that it secured the intake tube in place. Refer to Figure 2.3 for a description of the Plexiglas platform and the return line intake tube. Also, the thermocouple junction measuring the intake temperature was placed 4-5 inches inside the intake tube. The thermocouple junction measuring the temperature of the nozzle discharge was installed 2-3 inches inside the 1/2 inch reinforced clear PVC hose leading to the nozzle. Although the thermocouple junction measuring the temperature of the jet discharge was not placed exactly at the nozzle exit plane, it was not expected to be much different from the discharge nozzle temperature. Thermal analysis of the discharge temperature measurement is in Appendix K. Next, the copper coils used for controlling the jet discharge temperature were placed in a plastic bucket located in a nearby sink. The thermocouple junction, measuring the temperature of the water inside the bucket, was placed near the bucket center. After installing the copper coil, the nozzle was installed such that the discharge end was flush with the back wall of the test apparatus. Next, the top Plexiglas partition, which formed the ceiling and the back wall of the test apparatus, was placed in position. Figure 2.3 shows a diagram of the top Plexiglas partition. The top Plexiglas piece was leveled and moved forward until the Plexiglas plate, representing the ceiling, rested against the front wall of the tank. It was necessary to place some weights on top of the Plexiglas partition to prevent it from moving around. Finally, four thermocouple junctions, that were used to measure the temperature of the ambient water inside the tank, were placed on both sides of the jet. On each side of the jet, two thermocouple junctions were positioned about 0.5 in inside the Plexiglas plate (representing the ceiling). Figure 2.3 shows the location of the thermocouples used for measuring the ambient water temperature. The thermocouples were located 4-6 inches in front of the test apparatus vertical back wall. Two of the thermocouples were about 1 to 2 inches bellow the ceiling and the other two were about 1 to 2 inches above the base platform.

3.2.2 Controlling Operating Conditions

The desired experimental conditions were obtained by controlling the flow rate of the discharge water, and the temperature difference between the discharge water and the ambient water inside the tank. When setting the flow rate, the pump was started and the throttle valve was adjusted to attain the desired flow rate. For controlling the temperature difference between the jet discharge and the ambient water inside the tank, the plastic bucket containing the copper coils was first filled with water. The water temperature was adjusted appropriately to provide the desired temperature difference between the water temperature at the nozzle discharge and the temperature of the ambient water in the tank. Uncertainty in the temperature difference measurement (inlet-to-ambient) was within about ±0.2 ° F. Details of the uncertainty analysis for temperature difference measurement are included in Appendix K, along with the thermocouple calibration. Based on the discharge flow rate, and the temperature difference between the jet discharge and the ambient water inside the tank, three types of test conditions were set up. The test conditions were either approximately isothermal, buoyant, or approximately isothermal with variable flow rate. For the isothermal tests, the water at the nozzle discharge was controlled to within ± 0.5 °F of the temperature of the ambient water inside the tank. For the buoyant jet, the temperature difference between the jet discharge and the ambient water in the tank was set to a negative value, then it was increased slowly towards a positive value. For the variable flow rate tests, the flow rate was set to three different levels (0.023 GPM, 0.062 GPM, and 0.078 GPM). For the low flow rate, the temperature conditions were close to isothermal. The jet in the higher flow rates tests was slightly buoyant. Table 3.1 includes a list of the test conditions for the axial and cross-sectional jet image tests.

For the approximately isothermal test, which was mainly conducted to investigate the effect of ceiling-to-nozzle spacing on the location of the jet attachment, the plastic bucket containing the copper coils was first filled with water at a temperature about 0.5 °F below the temperature of the water inside the tank. Then, the flow rate was set to the desired value (0.023 GPM). The copper coil immersed in the cooling water provided the necessary heat transfer to control the discharge water temperature before it reached the nozzle. As the test was first started, the water temperature at the nozzle discharge was the same as the water temperature in the plastic bucket containing the copper coils. The pump heat input then slowly increased the temperature of the water inside the plastic bucket containing the copper coils, and hence increased the water temperature at the jet discharge. The discharge water temperature increase was very slow, so the jet temperature was essentially quasi-steady. Most tests took about 30 minutes to run. This was mainly because the temperature of the ambient water eventually changed more than a tolerable amount. Also, the seed material clouded up the tank and no clear images of the jet could be obtained. Appendix O contains preliminary tests that were run to determine the duration during which the temperature of the water in the tank was essentially constant. The rate of the discharge water temperature increase was about 0.1 °F every 6-7 minutes. When the temperature of the discharge water was about 0.1 °F below the temperature of the ambient water inside the tank, the seeds were injected into the flow as described earlier. Usually when the seeds reached the nozzle exit plane, the jet discharge temperature was about 0.1 °F - 0.2 °F higher than the ambient water inside the tank.

For the negatively buoyant jet, the temperature of the water in the cooling bucket was initially set about 2 °F below the temperature of the ambient water inside the apparatus. Then the pump heat input was used to slowly increase the temperature of the water at the nozzle discharge. When the temperature difference between the jet discharge and the ambient water temperature became about -1.5 °F, the seeds were injected inside the intake tube. Since the temperature change was slow and the seeds eventually ran out, it was necessary to inject new water/ TiO_2 solution into the flow as the new temperature conditions were attained. For the positively buoyant jet, the seeding solution was injected into the flow when the jet was about isothermal. Then, the process continued as in the negatively buoyant jet case. Table 3.1 has a list of all temperature and flow rate conditions for the tests.

3.2.3 Image Acquisition

Once the seeds reached the nozzle exit, the camera was adjusted to properly view the jet, and the gamma setting (sensitivity) on the camera was set to 1. For the VCR taping of the jet, the tape recording was started and stopped using the VCR controls. Controlling the CCD camera was achieved by the DT-261 frame grabber, the computer, and using interactive image grabbing software. For the laminar jet images, the DT-IRIS TUTOR software was used to interface between the camera and the frame grabber. For the cross-sectional isothermal jet images, the position of the jet visible cross-section was incremented by 0.4 inches toward the camera after grabbing each image. Changing the position of visible jet cross-section was achieved by traversing the light sheet along the nozzle axis. The light sheet moved using the manual traverse which had 0.1 in distance of travel per turn. For the turbulent jet images, the program RECORD, which is a combination of several C and machine assembly codes, was used to grab one jet image every 0.1 second. A listing of the RECORD code is given in Appendix M.

3.3 Image Processing

Image processing and manipulation was necessary for extracting quantitative information from the jet images and printing them. The most important aspect of the image processing was using the images to measure the jet dimensions and deflection. To make a distance measurement between two points on an image, the distance was measured first in pixels, using image editing software such as the DT-IRIS TUTOR software and the XView[2] image editor. Then, the number of pixels in the image dimensions were combined with the image scale factors, according to Equations (3.1) and (3.2), to calculate the length of the measured distance in inches. Measuring the distance between two points on an image allowed measuring the jet-to-plate attachment length, and the jet parallel and normal growth scales. The Xview image editor was used to determine the image pixel coordinates in this work because it provided better resolution than the DT-IRIS TUTOR software. Before the image could be edited in the Xview image editor, the image was transformed into the (.PGM) format which is recognizable by the Xview editor. Transforming the image file format from the (.IMG) format into the (.PGM) format was done by the IMAGE.C program. A source listing of IMAGE.C is given in Appendix N.

Several steps of image processing were applied to the images before they were printed. A summary of the image processing sequence is given in Appendix H. The printing image processing included filtering the images from the background noise,

[2] Xview is an image editor available on the KSU UNIX work stations

selecting an area around the jet and deleting the image portions outside the selected area. Also, the image aspect ratio was normalized. A 0.25 inch grid was drawn on the images by setting the intensity value for the pixels that correspond to the grid to some uniform intensity level. The grid was drawn using the PROCESS.C program. A listing of the PROCESS.C source code is given in Appendix N. The grid provided a convenient way to represent the physical dimensions of each image. Several images then were combined on the same file for ease of comparison between the jet behavior for different boundary and flow conditions.

est Number	Jet Description	Orientation	Test conditions		
			plate-to-nozzle spacing	Discharge-ambient temperature difference	Flow Rate
1	Laminar Isothermal	cross-sectional	Varied 6/16 in - 18/16 in	ΔT<0.5 °F	Fixed 0.023 GPM
2	Laminar Isothermal	Axial	Varied 6/16 in - 18/16 in	ΔT<0.5 °F	Fixed 0.023 GPM
3	Buoyant	cross-sectional	fixed 12/16 in	varied -0.8 °F<ΔT<1.7 °F	Fixed 0.023 GPM
4	Buoyant	Axial	fixed 12/16 in	varied -1.2 F<ΔT< 1.2 F	Fixed 0.023 GPM
5	Turbulent	cross-sectional	fixed 12/16 in	fixed (not controlled) 1.5 °F 2.0 °F	varied 0.062 GPM 0.078 GPM
6	Turbulent	Axial	fixed 12/16 in	fixed (not controlled) 1.5 °F 2.0 °F	varied 0.062 GPM 0.078 GPM

Table 3.1 List of Experimental Conditions

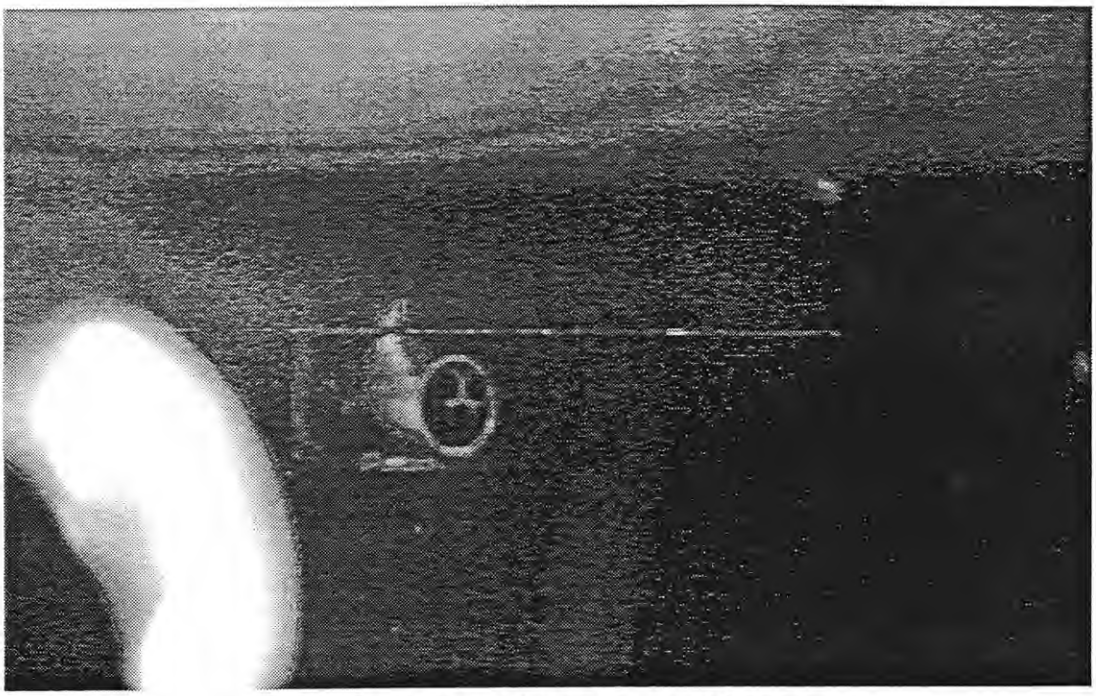

(a) Cross-Sectional Images Camera Alignment

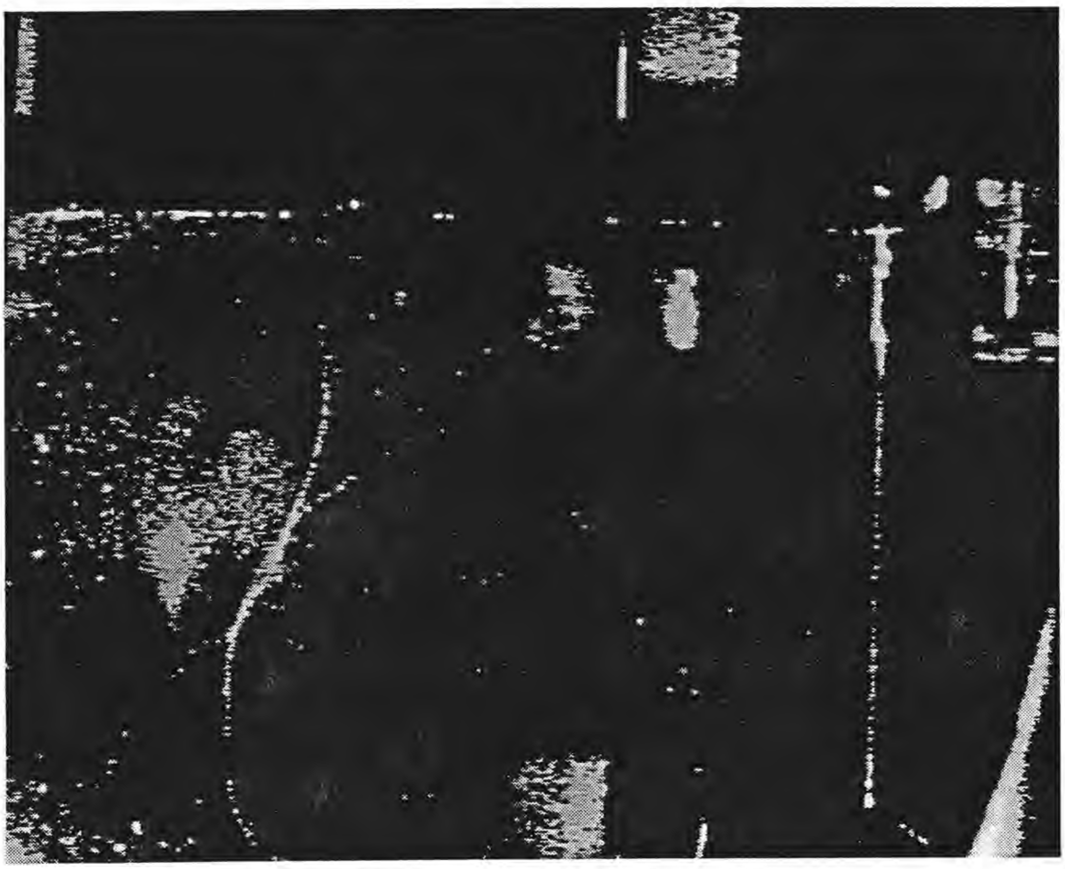

(b) Axial Images Camera Alignment

Figure 3.1 : Camera Alignments

Chapter 4

Experimental Results

This chapter includes a presentation of the experimental flow visualization test results. The effect of the jet-to-ceiling height on the isothermal laminar jet deflection and attachment distance was determined for five jet-to-ceiling heights. Also, the temperature (buoyancy) and flow rate effects on the jet were observed. Axial and cross-sectional images of the jet were obtained to show how the jet behaved in accordance with each set of imposed test conditions. Each of the following sections discusses a different set of the test conditions and the set of the jet images that goes along with them.

4.1. Effect of Jet-to-Ceiling Height on the Isothermal Laminar Jet Reattachment

The effect of ceiling-to-nozzle height on the deflection of the isothermal laminar jet was determined for five jet-to-ceiling heights. One axial jet image and a set of cross-sectional jet images were obtained for each jet-to-ceiling height. For these tests a nearly isothermal jet inlet-to-ambient temperature difference was attempted. However, since the axial and cross-sectional jet images did not have the exact temperature conditions (i.e. inlet-to-ambient temperature difference), some variation was expected between the jet trajectory extracted from the cross-sectional and axial images. The influence of temperature difference(buoyancy effects) is presented in section 4.2 below. The orientation of the jet with respect to the coordinates system of the images, for both the axial and cross-sectional tests, is illustrated in Figure 2.2. Axial jet images contain a vertical slice of the jet in the axial plane that passes through the center of the nozzle. The cross-sectional jet images contain slices of the jet parallel to the exit plane of the nozzle. Cross-sectional jet images were traversed along the jet axis such that the first image contained the jet very near to the exit plane of the nozzle. Subsequent images were spaced about 0.4 inches apart and were incremented towards the camera. Beside the qualitative information, the jet images provided quantitative information about the attachment distance and the (horizontal and vertical) growth rate of the jet.

4.1.1 Flow Visualization

Figure 4.1 shows cross-sectional jet images for the five variations in jet-to-ceiling height. The coordinate system for the cross-sectional images was illustrated in Figure 2.2(b). The top horizontal grid line coincided with the ceiling, and the central vertical grid line coincided with the vertical middle plane of the nozzle. All jet cross-sectional images were spaced 0.4 in apart along the jet axis starting from the plane of the nozzle exit. The jet cross-sectional (axial) position, with respect to the nozzle exit, is indicated beneath each cross-sectional jet image in Figure 4.1. The jet was designed to exit with an approximately fully-developed laminar velocity profile. Flow visualization of the jet profile, as the seed first enters the tank from the exit plane, suggests this is to be the case. It is seen in Figure 4.1(a) through Figure 4.1(e) how the jet was deflected up toward the ceiling, eventually attaching itself to the upper wall and turning into a wall jet. Figure 4.1(a) shows the variation in observed jet cross-section, as a function of distance from the exit plane of the jet, for the minimum spacing of 6/16 inches. The jet cross-sections were circular in shape and fairly symmetrical as the jet first came out of the nozzle for all cases. At some distance down stream from the nozzle, the jet cross sections became somewhat elliptical in shape. There was a flattening near the top of the cross-section before the jet actually became attached to the ceiling. For the minimum spacing shown in Figure 4.1(a), the observed attachment point appears to be approximately at the x=2.4 in axial position. By the time the jet reaches the x=4.4 in axial position, it is apparently somewhat flatter in the vertical direction and has about doubled in width. The cross-sectional images of the jet (for cases of jet-to-ceiling heights equal to 6/16 in, 9/16 in, and 15/16 in) maintained reasonable symmetry, within the limitations of the simple apparatus, as shown in Figures 4.1(a), 4.1(b), and 4.1(d). The cross-sectional isothermal jet images in the cases using ceiling-to-plate height equals to 9/16 in and 18/16 in, had slight asymmetry that appeared in the jet cross-section about 2.8 inches away from the nozzle exit. As shown in Figures 4.1(c) and 4.1(e), the jet asymmetry in the jet cross-sectional shape propagated and became more pronounced after the jet became attached to the wall. The asymmetry in the jet cross-sectional shape, for the jets shown in Figures 4.1(b) and 4.1(c), was possibly a result of the imperfection in alignment of the nozzle assembly. It was somewhat difficult to maintain true normal-to-the-wall nozzle alignment because the flexible PVC hose, which was connected to the nozzle assembly, applied stress to the nozzle assembly. This could slightly move the jet assembly and cause the nozzle to discharge at a slight angle from the normal.

Comparison between Figure 4.1(a) through Figure 4.1(e) shows that the jet attachment length became longer as the jet-to-ceiling distance increased. The cross-sectional images gave a rough estimate of the point of attachment for the jet. The location of the jet attachment, made using the cross-sectional images, was estimated to be accurate within about ±0.2 inches, since the cross-sectional images were located 0.4 in apart along the jet axis. Better jet attachment length estimates were made using the jet axial profile images. Figure 4.2 shows a longitudinal slice through the jet axis for each case of the five jet-to-ceiling heights. Coordinates of the jet in Figure 4.2 were explained in Figure 2.2(a). The jet in Figure 4.2 discharged from right to left. The top grid line coincided with the ceiling position and the left grid line coincided with the location of the vertical back wall of the test apparatus. The longitudinal images provided a direct measure of the apparent jet attachment point. Magnitudes of the uncertainty in the jet attachment point measurement, made using the axial image, varied between about ±0.12 inch and ±0.30 inch. Details of the uncertainty estimates in measuring the distance to the jet reattachment to the plate are found in Appendix C. It is seen from the jet axial profile images that the jet necks down near the point of attachment. Then it starts growing normal to the wall after the jet attachment to the wall. This “growth”, after deflection off the top wall downstream of the reattachment position, has the appearance of a hydraulic jump, similar to that which would be observed in a free water jet (in air) impinging on a flat surface. Vertical growth of the jet was not seen in the images due to the limited camera field of view.

4.1.2 Quantitative Results

Knowing the images horizontal and vertical scale factors of the images allowed quantitative extraction of the location of the point of attachment to the plate. Also, it was possible to somewhat quantify the jet trajectory and expansion for different jet-to-ceiling heights. Figure 4.3 shows the trajectory of the jet upper and lower edges, as extracted from the axial and cross-sectional images of the jet. Figure 4.3 suggests a similarity between shape of the jet upper and lower edges for the different jet-to-ceiling heights which was also shown by Sawyer (1960). The differences observed between the jet trajectory estimation made using the cross-sectional and axial jet images were due to a combination of variation in the test conditions, and the ability to resolve the location of the jet upper and lower boundaries from the images; especially for the cross-sectional images that had an asymmetrical jet. However, there is generally good agreement between apparent attachment locations determined from the cross-sectional and axial profile results. This gives some measure of the repeatability, since the cross-sectional and profile tests were generally run independently with an attempt to re-establish identical operating conditions. A list of the experimental conditions and attachment lengths for both cross-sectional and axial tests are given in Table I.1. Also, the data used for plotting Figure 4.3 is in Table I.2.

The relationship between the jet point of attachment and the jet-to-ceiling height is explained in Figure 4.4. Figure 4.4 shows a plot of the attachment point estimates, made from both axial and cross-sectional images of the laminar isothermal jet, versus the ceiling-to-nozzle height. The agreement between the two methods appears to be about 10%. Figure 4.4 also compares the jets attachment point measurements with some approximate theoretical predictions of the jet attachment length. The theoretical prediction of the jet attachment length was based on a simple theory that was developed for a plane turbulent isothermal jet issuing from a slot nozzle. This theory was introduced by Dodd's (1959) and evaluated by Sawyer (1960) and Newman (1960). It was found to be in good agreement with experimental results obtained by Sawyer (1960) and Newman (1960). In this theory an empirical constant σ, which is a measure of the turbulent jet entertainment, must be determined experimentally. Two values (12 and 15) of the constant σ were used to compare to the attachment length measurement made in the present study. This approximate theory was not expected to closely predict the attachment point measured in the present study because of the differences in the nozzle geometry and since the model is not specifically for laminar flow. However, this theory incorporates much of the essential physics, and shows a very similar trend to the measured attachment points. It gives predictions which are about 30% below the experimental measurements. Details of both model development and solution are found in Appendix D. As the jet-to-ceiling distance is increased, the jet attachment position moved further away from the nozzle exit. Some differences between the measured attachment point locations and the theoretically estimated values was expected since all the tests were somewhat buoyant. Also, differences existed between the real flow and the approximate model; the real flow is three-dimensional, while the model is two-dimensional. The cross-sectional image estimation of the jet attachment lengths were somewhat different from the axial image estimates because the tests were run under slightly different temperature conditions, as described above.

Figure 4.5 shows the scaled trajectory of the jet. The y-coordinates of the jet upper and lower boundaries was scaled with respect to the corresponding y-coordinates of the jet upper and lower boundaries at the nozzle exit. The x-coordinates of both boundaries of the jet were scaled with respect to the jet-to-ceiling attachment distance. It is seen from Figure 4.5 that the jet trajectories approximately collapse on the same curve as the jet is scaled. Figure 4.6 shows the growth of vertical and horizontal dimensions of the jet. It is clear that the jet grows much faster in the horizontal direction, particularly after attachment.

4.2. Effect of Temperature Variation on the Laminar Jet Deflection

Temperature difference between the jet discharge water and the ambient water induced a buoyancy force that acted on the jet. This force is a result of the temperature-dependent density of water; warmer water being less dense than warmer water. Negative temperature difference between the jet discharge water and the ambient water (i.e. jet discharge water temperature less than ambient water temperature) deflects the jet downward (downward buoyancy force) and positive temperature difference deflects the jet upward (upward buoyancy force). The buoyant jet cross-sectional images shown in Figure 4.7(a) demonstrate the effect of increasing the temperature difference between the jet discharge water and the ambient water from a negative to a positive value. The vertical location of the jet cross-section, which was imaged about 2 inch away form the nozzle exit, was shifted upward as the temperature difference moved toward a positive value. Coordinates of the cross-sectional images in Figure 4.7(a) were previously explained in Figure 2.2b. The jet flow rate was 0.023 GPM and the jet-to-ceiling height was 9/16 in for all images. The temperature difference between the jet discharge water and the ambient water was varied between -.8 °F and 1.7 °F in a quasi-steady manner. In the first image on the top left corner of Figure 4.7(a), the buoyant jet image had -0.8 °F temperature difference from the ambient water. The temperature difference between the jet discharge water and the ambient water was slowly increased toward a positive value in the rest of the buoyant cross-sectional jet images until it became about +1.7 °F. The temperature difference was increased roughly at the rate of 0.1 °F every six to seven minutes. This was done by slowly increasing the water temperature at the nozzle discharge, while the ambient water temperature remained relatively unchanged. As Figure 4.7(a) shows, the negatively buoyant jet cross-section moved about 0.25 inches for a +0.8 °F temperature increase in the temperature difference between the jet discharge water and the ambient water. Symmetry in the buoyant jet cross-section existed about its vertical axis only. Figure 4.7(a) suggests that the buoyancy effects induced an asymmetry about the jet horizontal axis. The buoyant jet cross-section became pointed downward , with an inverted tear-drop shape, when the jet discharge water was colder than the ambient water. The jet became more circular in cross-section as the temperature difference between the jet and the surroundings was increased to a less negative value. Decrease in the jet downward stretching is noticeable by comparing the images in Figure 4.7(a) for the cases in which the temperature differences between the jet discharge water and the ambient water varied between -0.8 °F, -0.6 °F, -0.4 °F, and -0.3 °F. As the temperature difference between the jet discharge water and the ambient water approached the isothermal 0.0 °F temperature difference, the jet became rounded with near symmetry in the jet about both vertical and horizontal axes (i.e. nearly circular cross-section). The buoyant jet cross-section became pointed upward with a distinct tear -drop shape when the jet discharge water was warmer than the ambient water. This is seen in Figure 4.7(a) by looking at the buoyant jet cross-sectional images for the cases in which the differences between jet discharge water temperature and the ambient water temperature was varied between +0.3 °F, +0.6 °F, +0.8 °F, and +1.0 °F . At +1.1 °F difference between the jet water discharge and the ambient water, the jet became attached to the wall at the prescribed axial location of the jet cross-section. As the temperature difference increased further, the jet moved closer to the wall and the shape of the jet cross-section became almost half a circle, which is seen in Figure 4.7(a) for the image having +1.7°F temperature difference between the jet discharge water and the ambient water. In comparison with the isothermal tests, there appears to be less lateral spreading of the jet at the attachment point. Figure 4.7(b) shows a traverse through the jet cross-sections as the temperature of the water at the jet discharge was reduced further below the ambient water inside the tank. These tests were processed by taking 35 mm still pictures of video taping (VCR tape), hence they exhibit horizontal scan lines associated with the monitor used to display the images. The extreme negatively buoyant tests show a significant double-lobe cross-section which persists far down stream. The tear-drop shape cross-section became sharply elongated to many times the initial jet diameter, while retaining the "double-lobe" shape. This shape has some similarities to the cross-section shape of a circular jet injected into a uniform flow stream normal to the jet axis. In this later case, a double-lobe cross-section is induced by a pair of counter-rotating vortices. The symmetry, stability (repeatability) of the negatively buoyant jet characteristics is quite good, considering the simplicity of the experimental setup. Figure 4.7(c) shows a traverse through the jet cross-sections for a positively buoyant jet. Here the jet cross-section is seen to spread laterally into an inverted mushroom shaped cross-section as the jet comes in contact with the upper wall. It has the appearance of two separate symmetrical lateral wall jets impinging on the wall surface, with a hydraulic jump effect similar to that observed in the profile images of the isothermal jet attachment.

Depending on the relative magnitude and direction of the buoyancy and Coanda forces acting on the jet , the jet may remain attached to the wall or it might detach itself completely from the wall. The jet becomes fully-detached when the ratio of the buoyancy force to the inertia force exceeds a certain critical value of the Archemides number, Ar_c, defined by Zhang (1991). After the cold jet detaches from the wall, random instability and periodic breaking up of the jet was observed. Figures 4.8(a) and 4.8(b) show axial images of the negatively buoyant circular jet having 0.023 GPM nozzle flow rate at two different sequential times, for temperature difference between the jet discharge water and ambient water equal to -0.6 °F and -0.8°F respectively. Figure 4.9 contains axial negatively buoyant jet images that demonstrate the jet moving closer to the ceiling as the jet becomes relatively warmer. The coordinate system of Figure 4.9 is the same coordinate system illustrated in Figure 2.2(a). The jet flow rate was 0.023 GPM and the jet-to-ceiling height was 9/16 in . As shown in Figure 4.10, the effect of positive temperature difference in the laminar jet was confined to decreasing the jet attachment length. Figure 4.10 shows axial images of the positively buoyant jet for temperature differences between the jet discharge water and the ambient water equal to 0.4 °F , 0.8, °F

,and 1.2 °F. The location of jet attachment point moved closer to the nozzle exit as the temperature difference between the jet discharge water and the ambient water increased, while the profile shape remained approximately the same as for the isothermal tests.

4.2. Effect of Changing the Flow Rate of the Jet

Changing the jet flow rate was also expected to influence the jet behavior. As the flow rate is increased, the jet has more momentum and the jet attachment point at the upper wall is expected to move further away from the nozzle exit. If the flow rate of the jet exceeds the flow rate associated with the transition Reynolds number, which is 1000 for the axisymmetric free jet , the shape of the jet becomes time dependent. Figures 4.11 shows cross-sectional images of the jet about 2.0 inch away from the nozzle exit and grabbed 0.3 second apart. The jet-to-ceiling height was 9/16 in. For the jet shown in Figure 4.11(a), the water flow rate was 0.062 GPM, and the jet shown in Figure 4.11(b) has a water flow rate equal to 0.078 GPM. It is obvious that the shape of the jet is changing more rapidly as the flow rate of the jet is increased. Figures 4.12(a) and 4.12(b) contain the axial images of the turbulent jet. The jet flow rates for these tests were 0.062 GPM and 0.078 GPM respectively, and the jet-to-ceiling height was the 9/16 in for the jet in both Figure 4.12(a) and Figure 4.12(b). As seen from Figures 4.12(a) and 4.12(b), the location of the jet attachment was not defined by a single point. The jet was oscillating and the location of the jet attachment to the wall was changing with time.

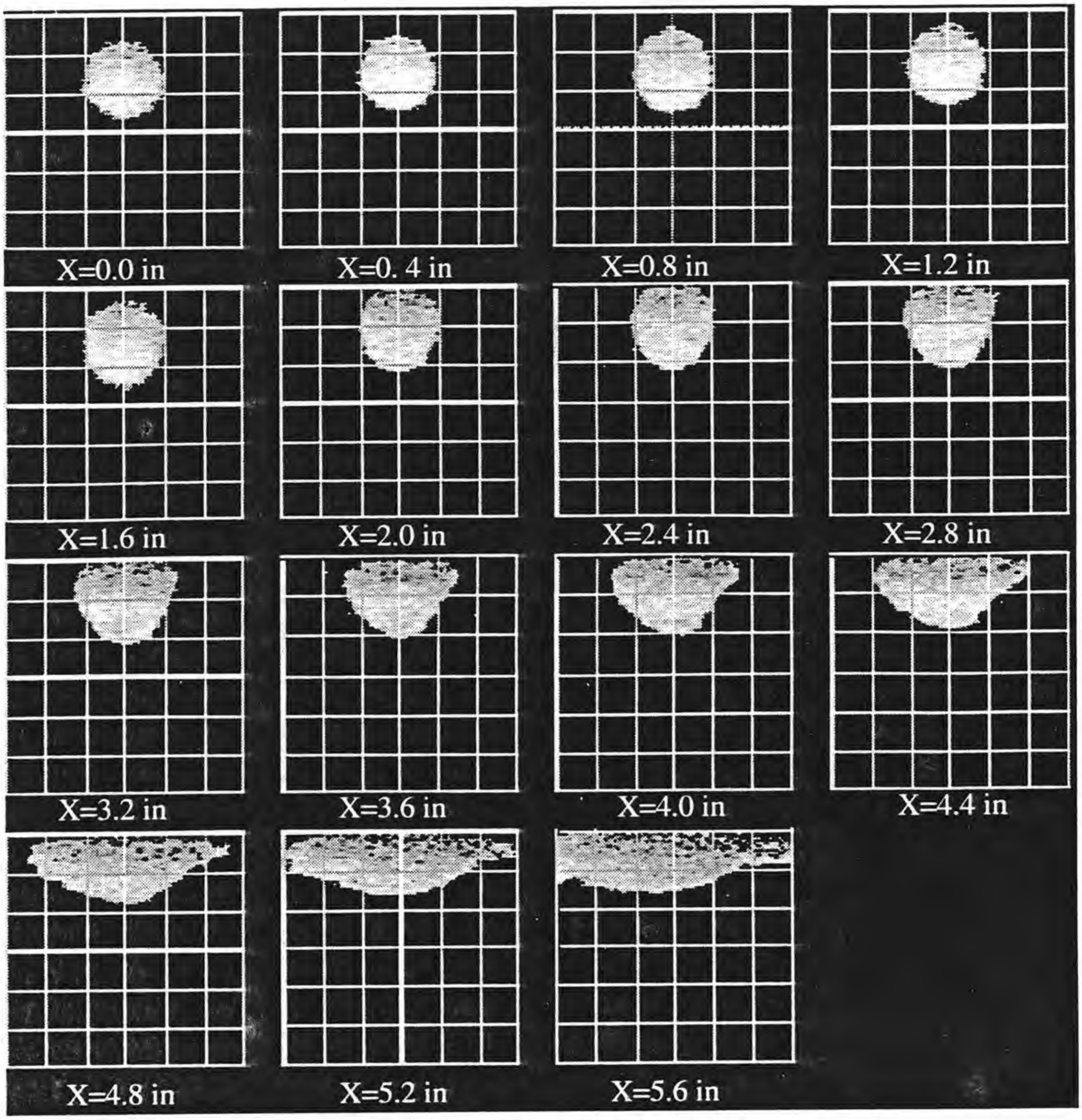

Figure 4.1 (a): Isothermal Laminar Jet cross-sectional Images

Ceiling-to-Nozzle Height, h = 6/16 in
Nozzle Inner Diameter, D = 0.473 in
Attachment length, L = 2.4 in
Grid = 0.25 in x 0.25 in
Camera-to-Tank distance : 7.375 in

Flow rate = 0.0230 GPM
Nozzle Reynolds Number, Re =163
Discharge Temperature, T_d = 71.4 °F
Ambient Temperature, T_∞= 71.1 °F
Temperature Difference, ΔT = 0.3 °F

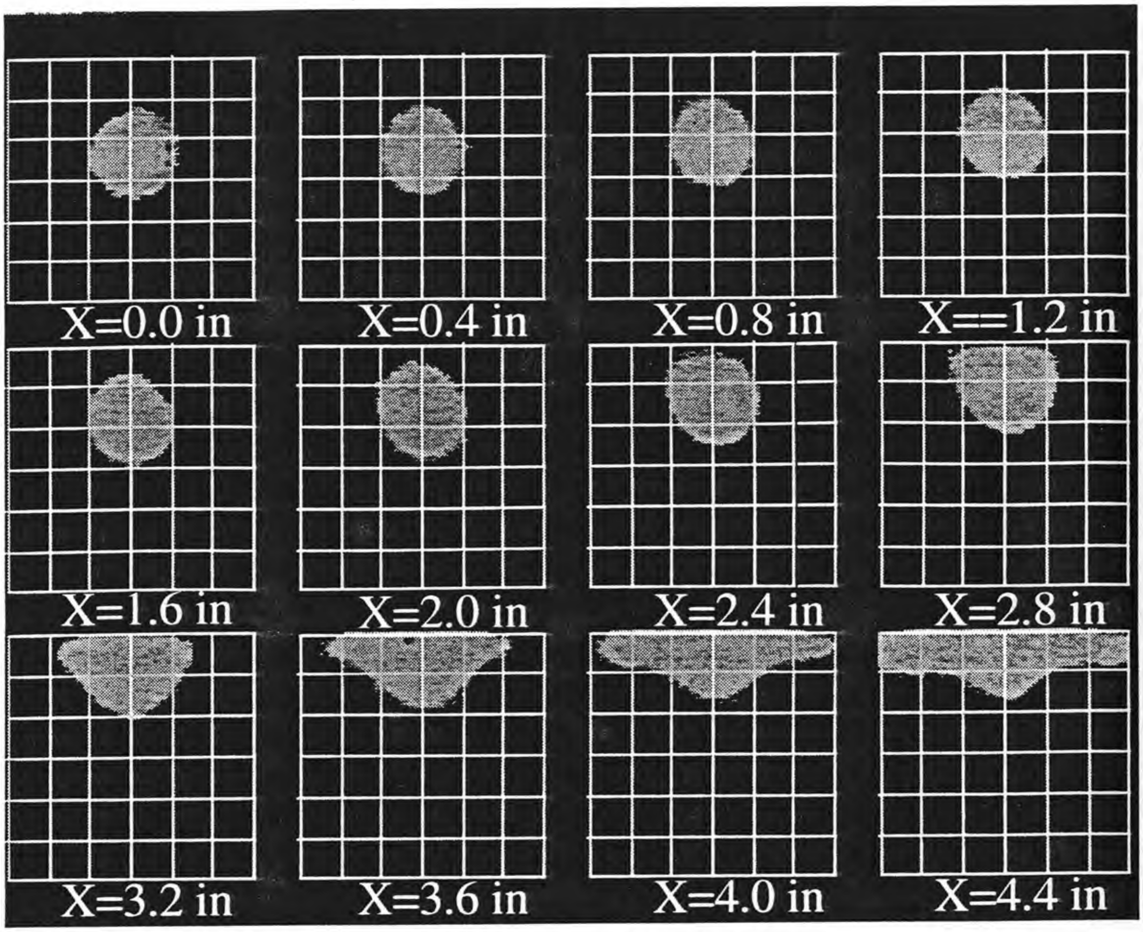

Figure 4.1 (b): Isothermal Laminar Jet cross-sectional Images

Ceiling-to-Nozzle Height, h = 9/16 in
Nozzle Inner Diameter, D = 0.473 in
Attachment length, L = 3.2 in
Grid = 0.25 in x 0.25 in
Camera-to-Tank distance : 7.375 in

Flow rate = 0.0230 GPM
Nozzle Reynolds Number, Re = 163
Discharge Temperature, T_d = 71.6 °F
Ambient Temperature, T_∞ = 71.3 °F
Temperature Difference, ΔT = 0.3 °F

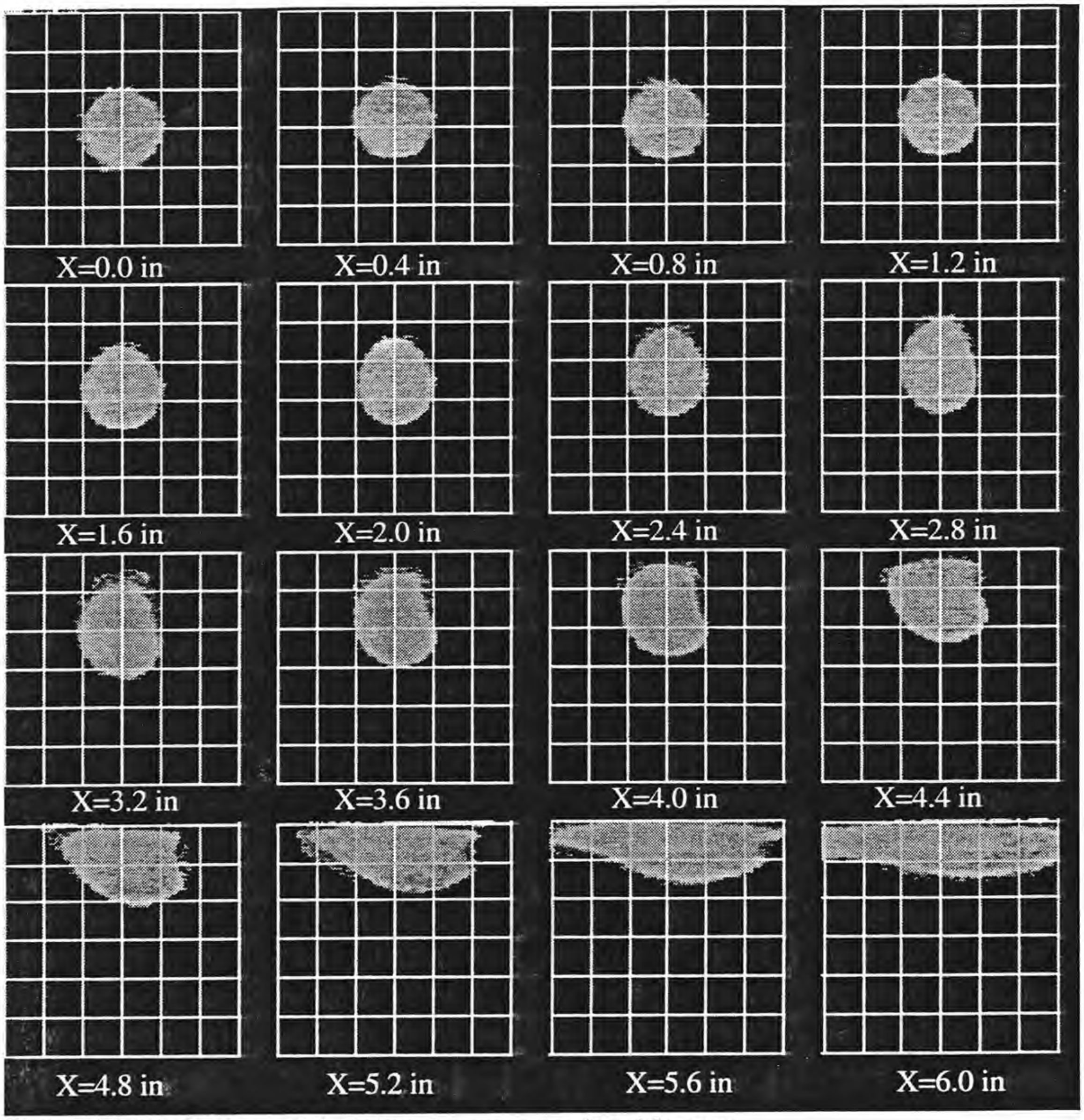

Figure 4.1 (c): Isothermal Laminar Jet cross-sectional Images

Ceiling-to-Nozzle Height, h = 12/16 in
Nozzle Inner Diameter, D = 0.473 in
Attachment length, L = 4.8 in
Grid = 0.25 in x 0.25 in
Camera-to-Tank distance : 7.375 in

Flow rate = 0.0230 GPM
Nozzle Reynolds Number, Re =163
Discharge Temperature, T_d = 72.0 °F
Ambient Temperature, T_∞= 71.8 °F
Temperature Difference, ΔT = 0.2 °F

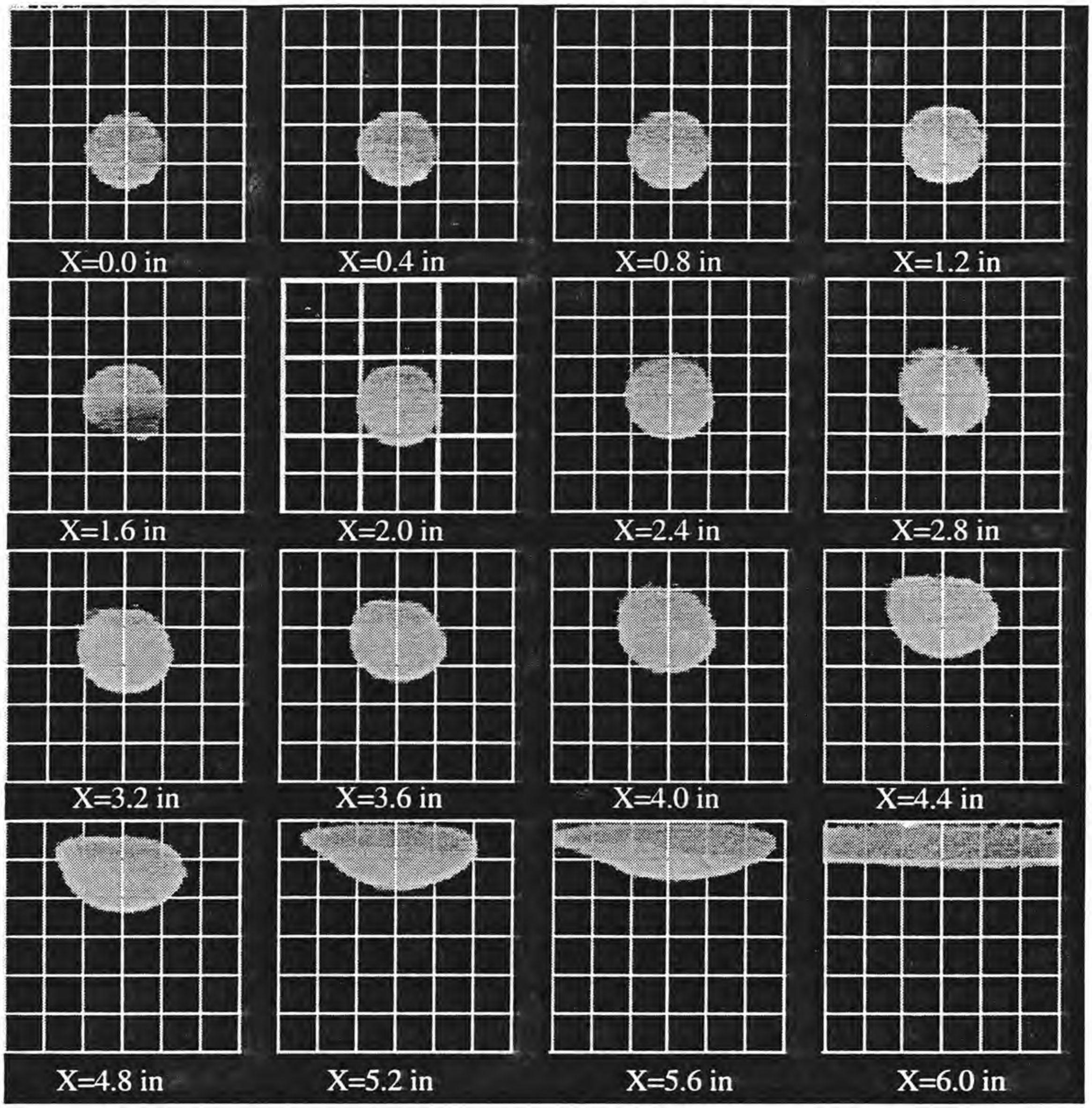

Figure 4.1 (d): Isothermal Laminar Jet cross-sectional Images

Ceiling-to-Nozzle Height, h = 15/16 in
Nozzle Inner Diameter, D = 0.473 in
Attachment length, L = 5.6 in
Grid = 0.25 in x 0.25 in
Camera-to-Tank distance : 7.375 in

Flow rate = 0.0230 GPM
Nozzle Reynolds Number, Re =163
Discharge Temperature, T_d = 73.4 °F
Ambient Temperature, T_∞ = 73.1 °F
Temperature Difference, ΔT = 0.3 °F

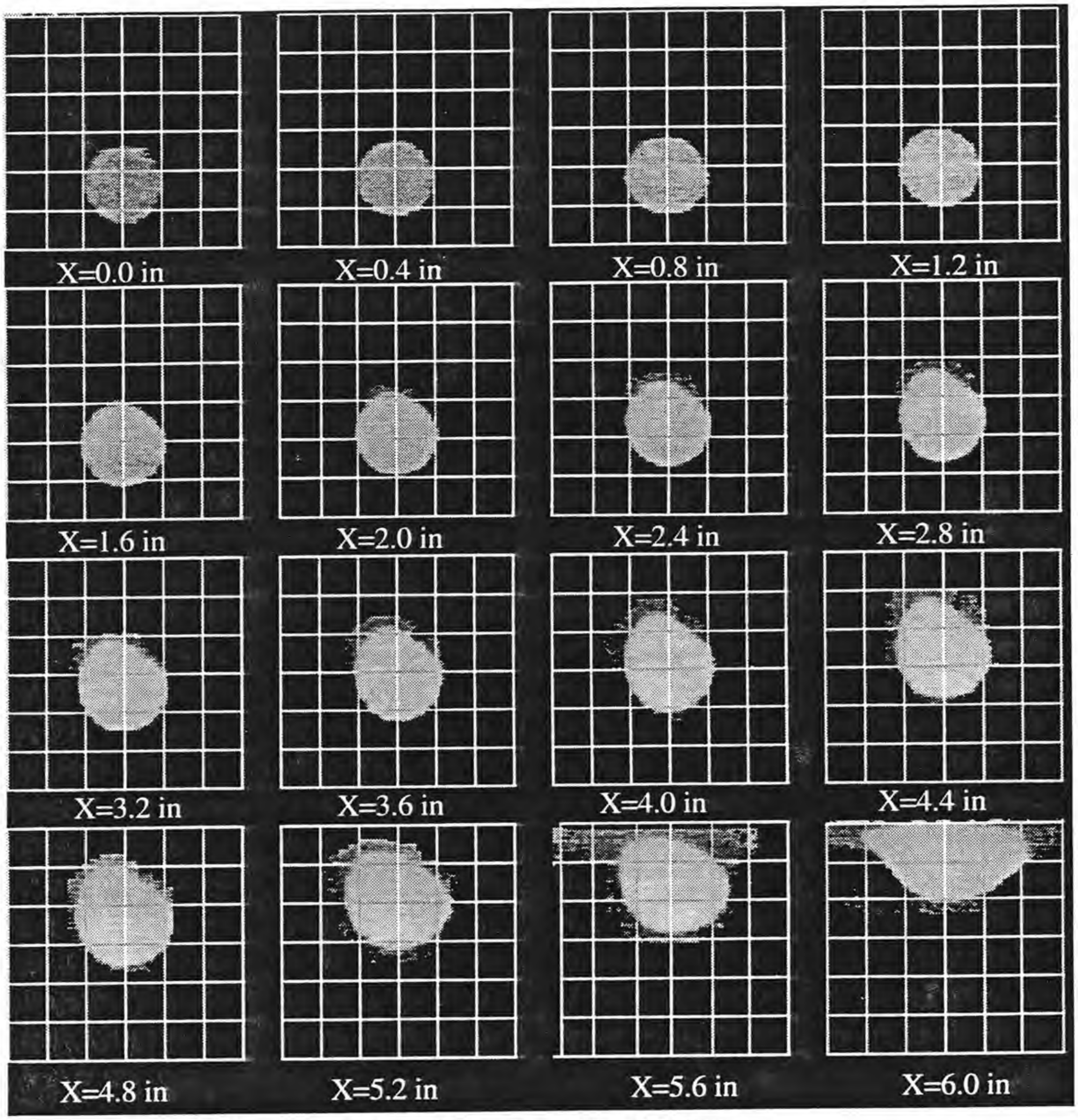

Figure 4.1 (e): Isothermal Laminar Jet cross-sectional Images

Ceiling-to-Nozzle Height, h = 18/16 in
Nozzle Inner Diameter, D = 0.473 in
Attachment length, L = 6.0 in
Grid = 0.25 in x 0.25 in
Camera-to-Tank distance : 7.375 in

Flow rate = 0.0230 GPM
Nozzle Reynolds Number, Re =163
Discharge Temperature, T_d = 75.8 °F
Ambient Temperature, T_∞ = 75.5 °F
Temperature Difference, ΔT = 0.3 °F

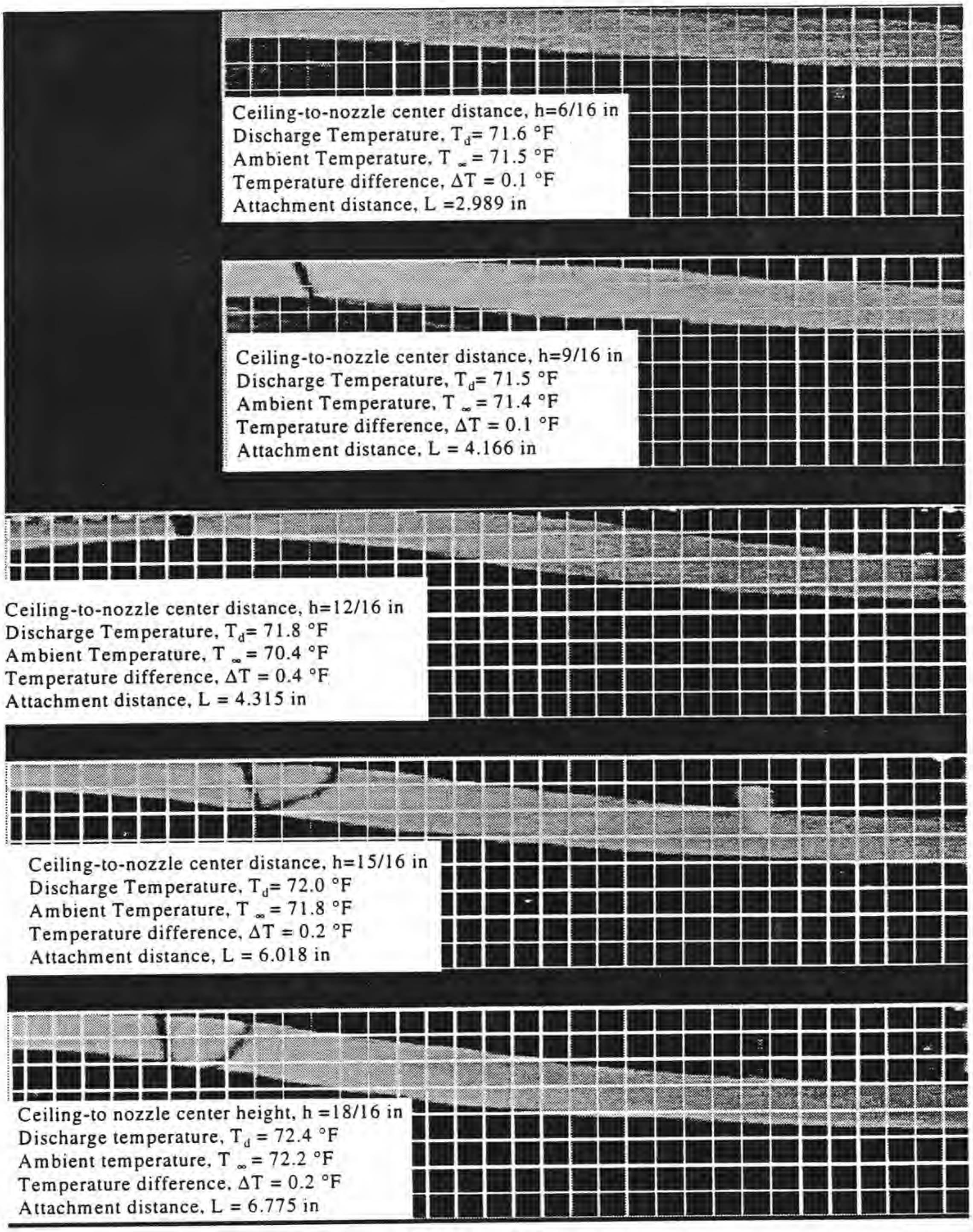

Figure 4.2: Axial Images of the Isothermal Laminar Jet for different Ceiling-to-Nozzle heights

Grid = 0.25 in x 0.25 in
Camera-to-Tank distance :
first 2 images: 12.5 in
Remaining 3 images: 15.75 in

Nozzle Inner Diameter D= 0.473 in
Water Flow Rate = 0.0230 GPM
Nozzle Reynolds Number, Re =163

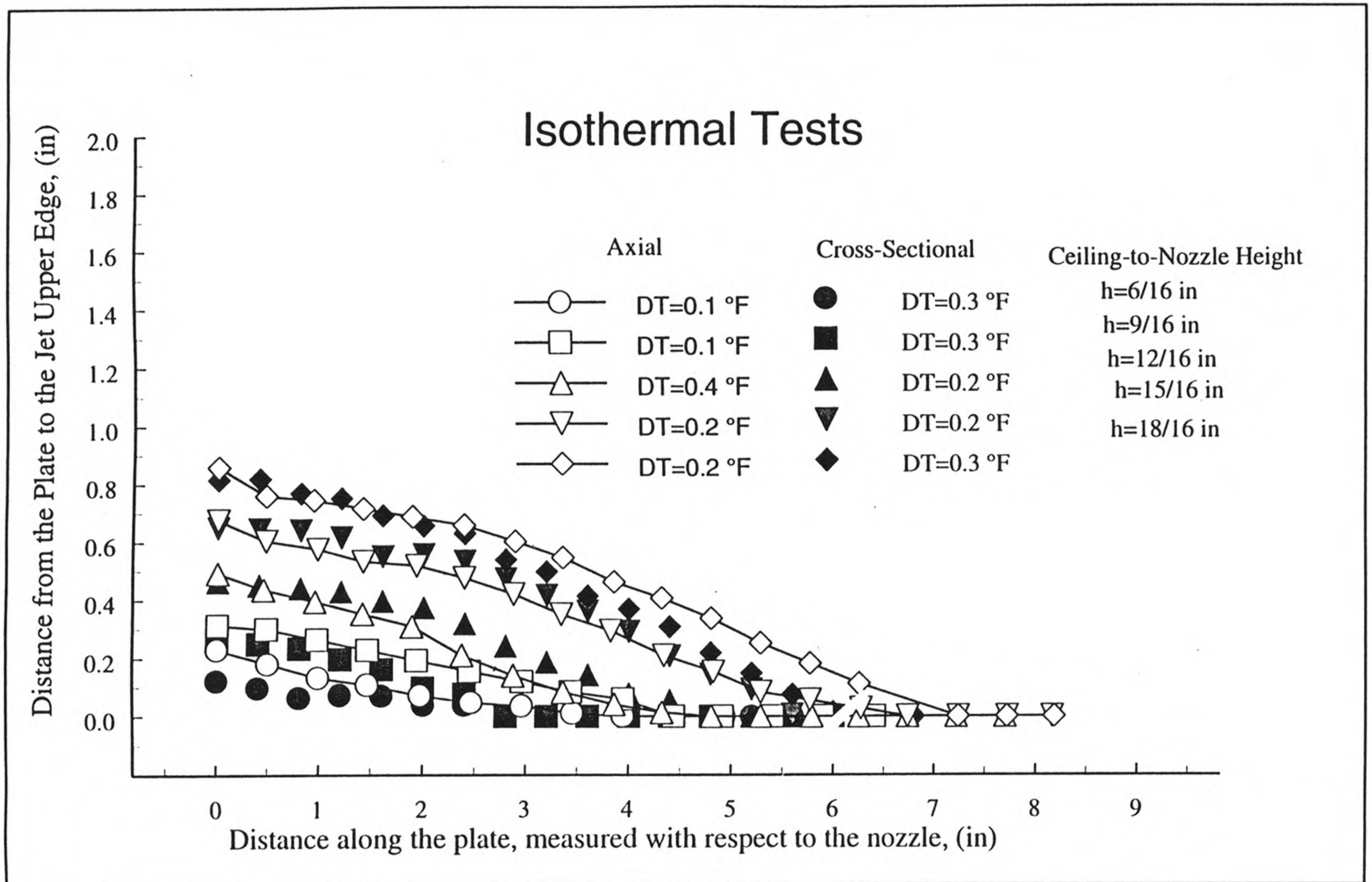

Figure 4.3: Trajectory of the Jet Upper and Lower Edges
(a) Upper Edge Trajectory

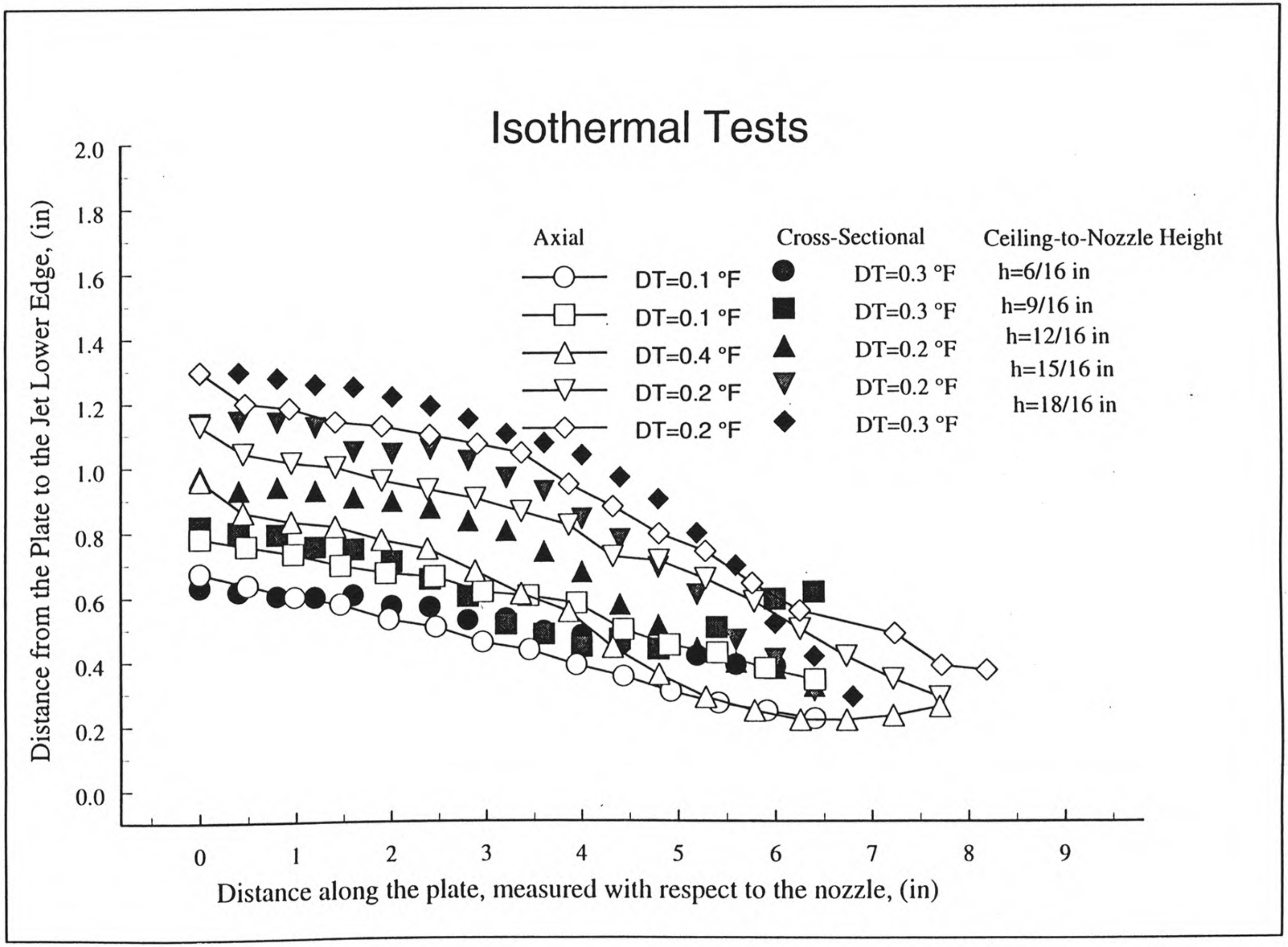

(b) Lower Edge Trajectory

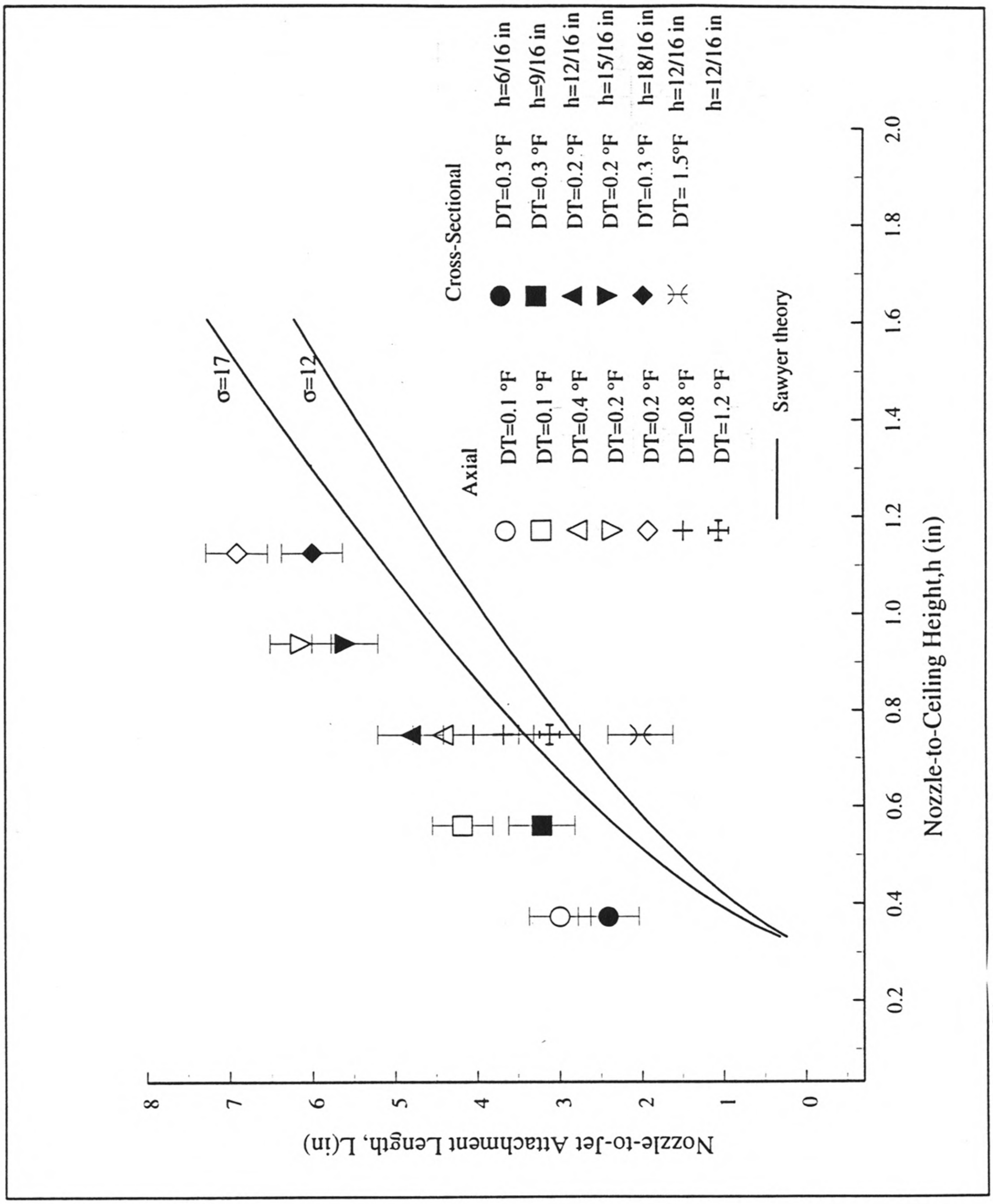

Figure 4.4: Jet Attachment versus Nozzle-to-Ceiling Height

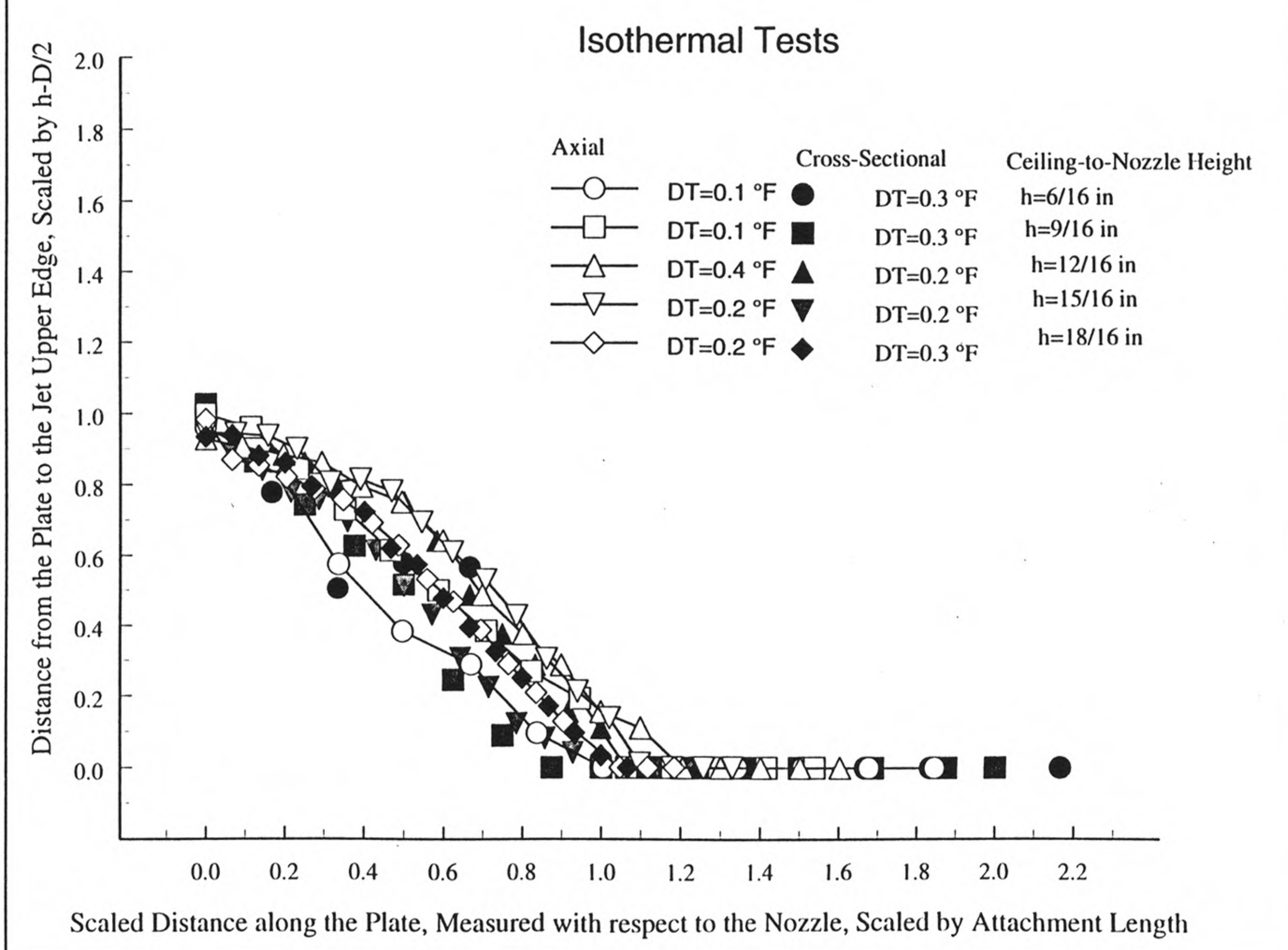

Figure 4.5: Scaled Trajectory of the Jet
(a) Scaled Trajectory of the Jet Upper Edge

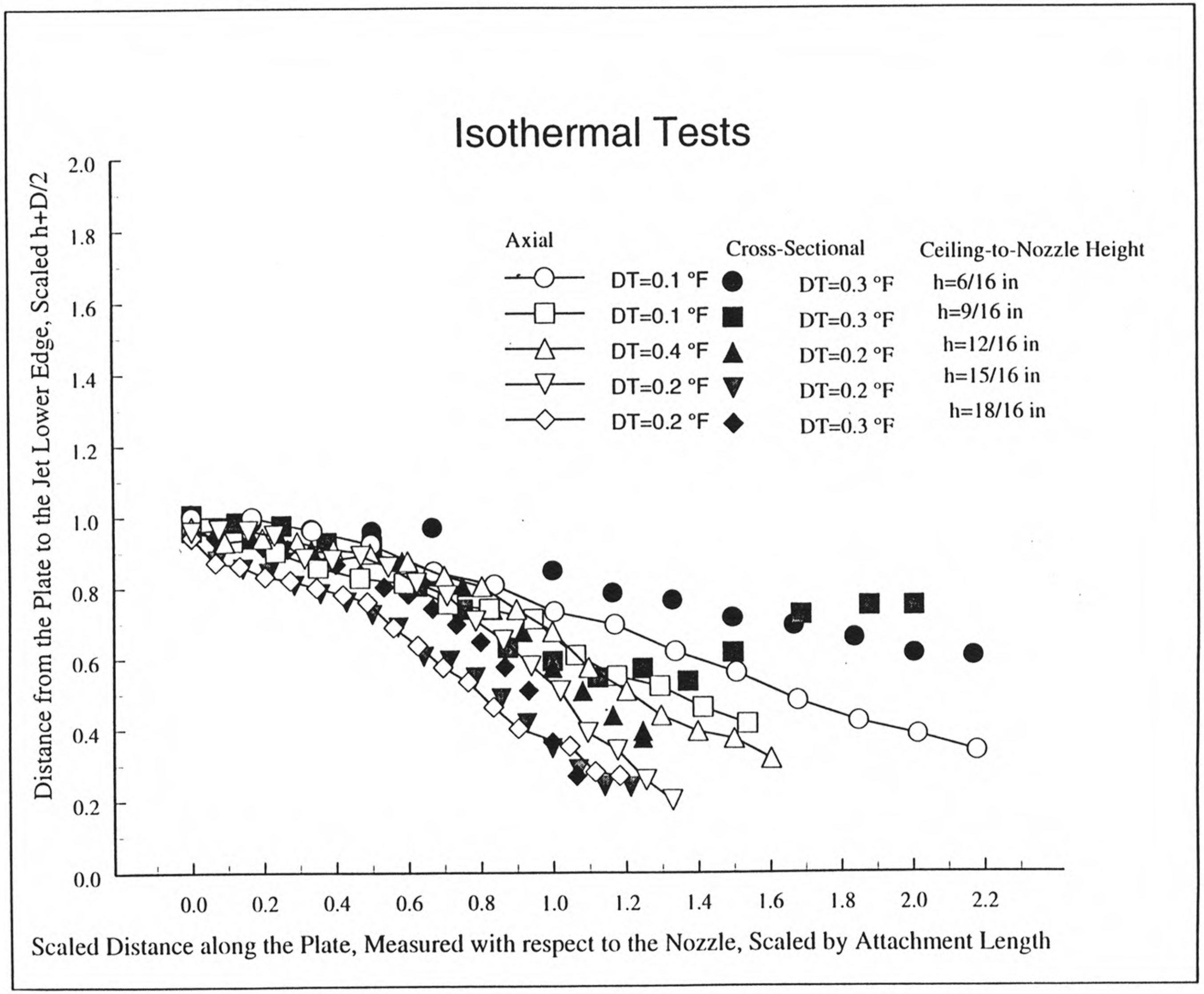

(b) Scaled Trajectory of the Jet Lower Edge

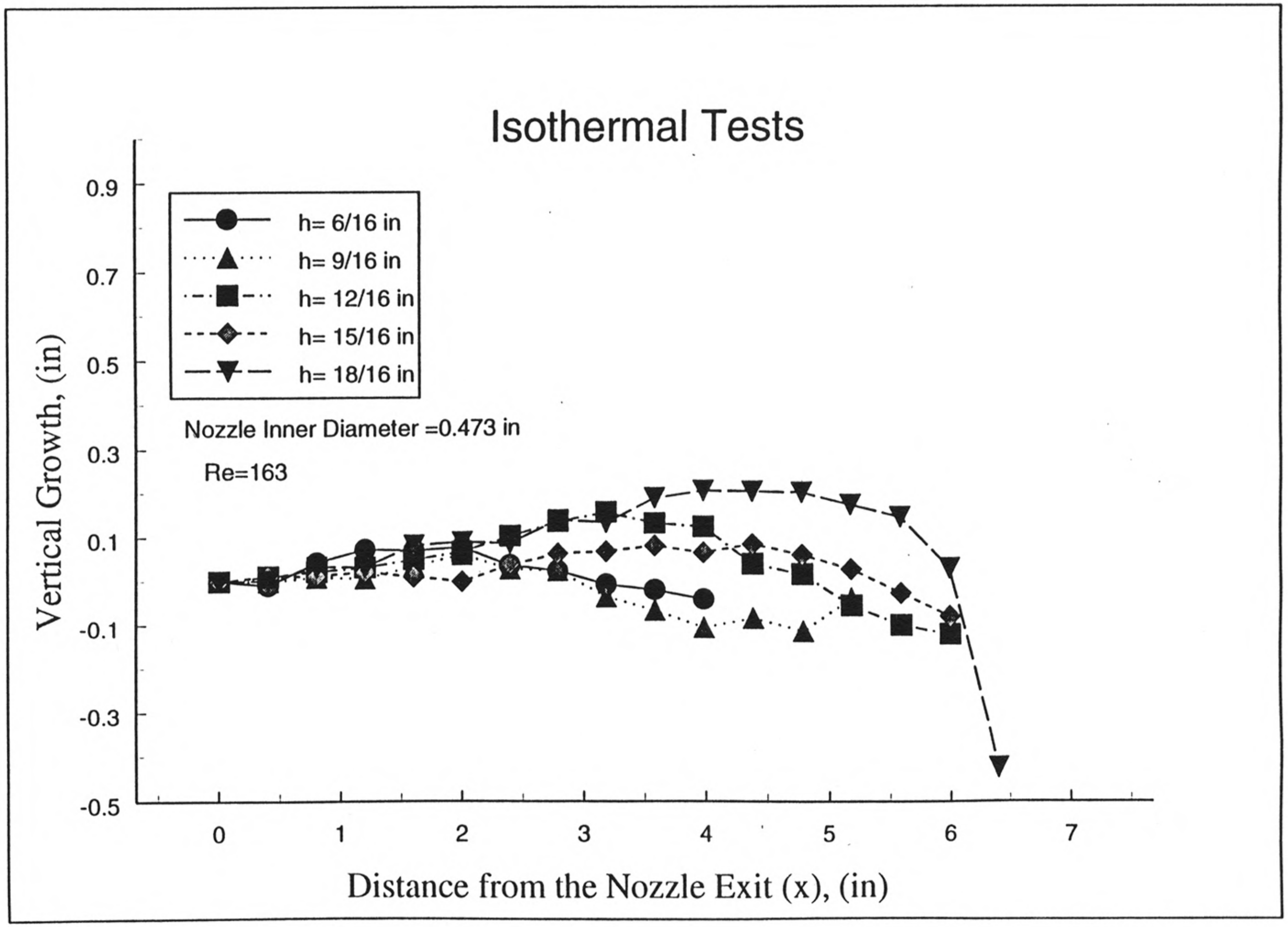

Figure 4.6: Horizontal and Vertical Growth of the Jet
(a) Vertical Growth Scale of the Jet

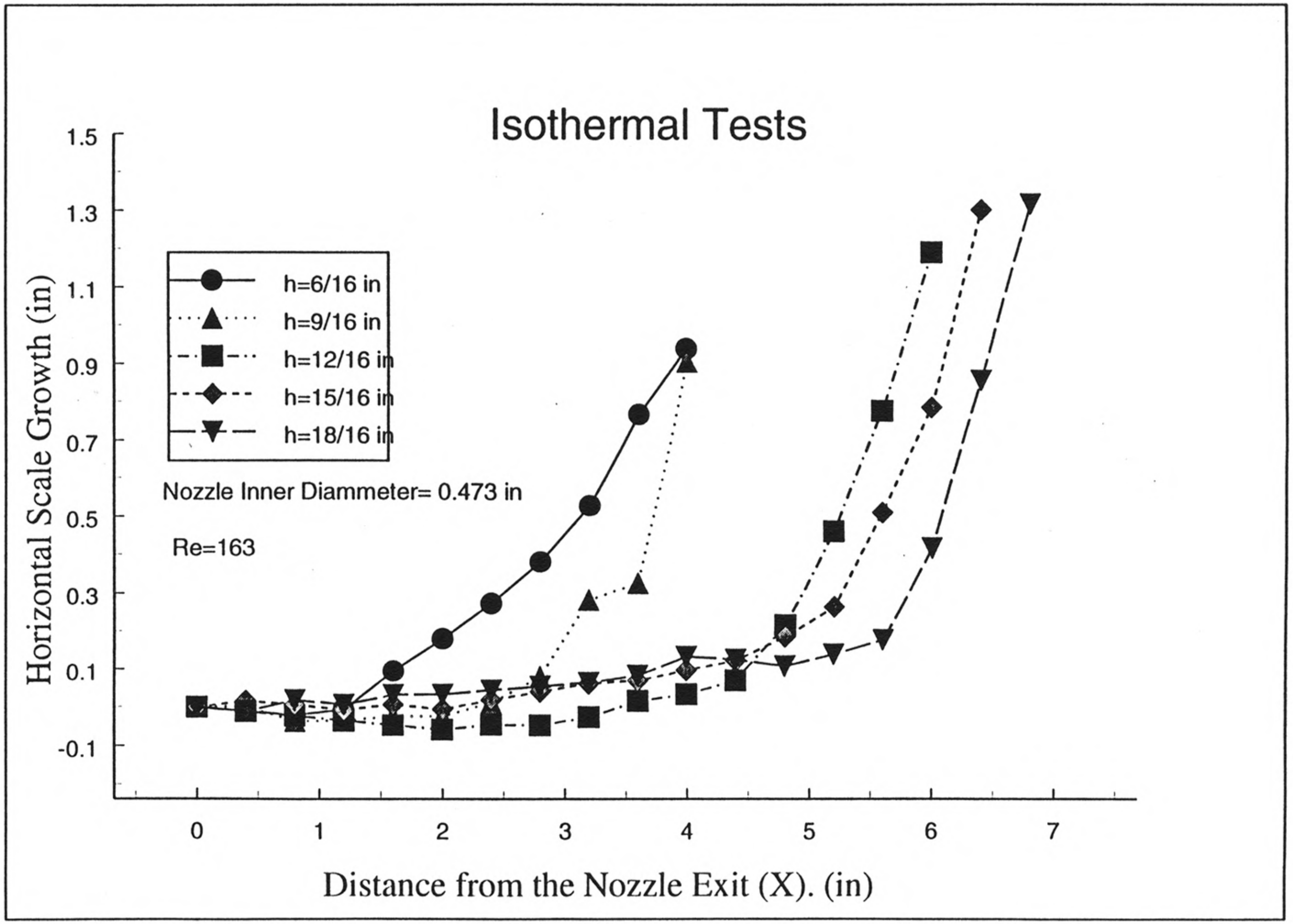

(b) Horizontal Growth Scale of the Jet

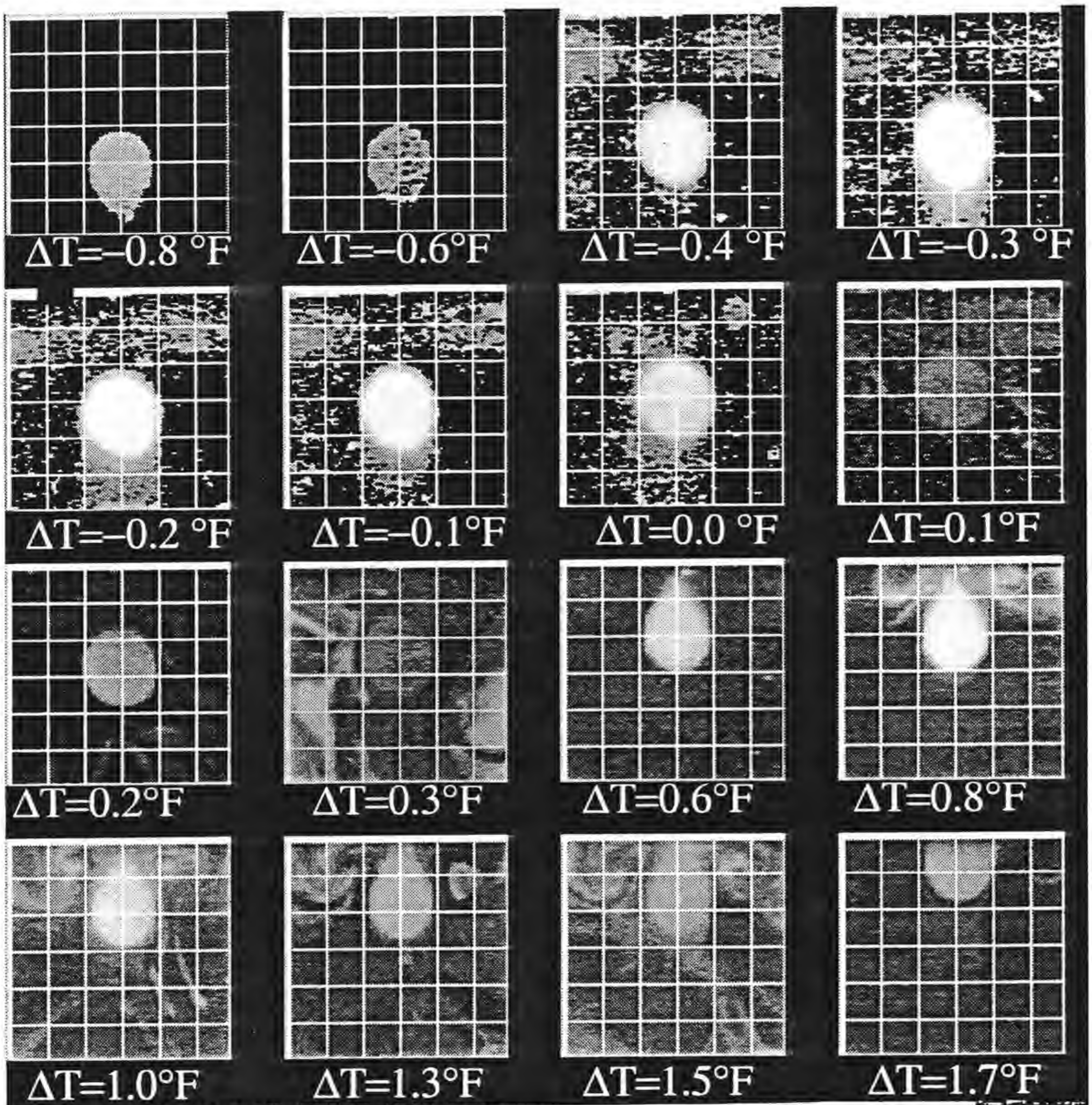

Figure 4.7: Cross-Sectional Images of the Buoyant Laminar Jet for
(a) Relatively Small Jet-to-Ambient Temperature Difference

Ceiling-to-nozzle height, h = 12/16 in
Grid = 0.25 in x 0.25 in
Camera-to-Tank distance : 7.375 in
Cross-section away from the Nozzle, X= 2.0 in

Nozzle Inner Diameter, D = 0.473 in
Water Flow Rate = 0.0230 GPM
Nozzle Reynolds Number, Re =163

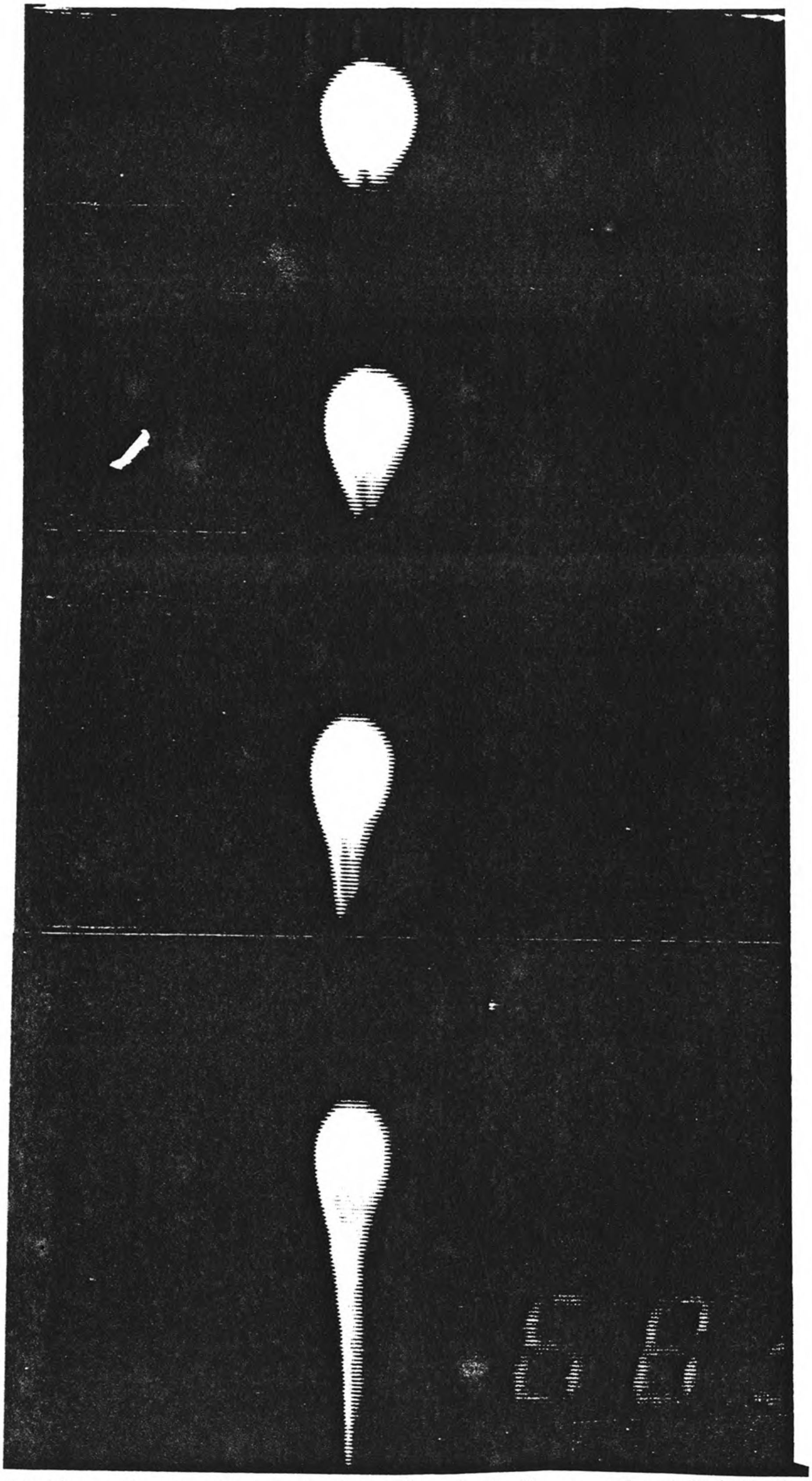

(b): Cross-Sectional Images of the Negatively Buoyant Jet at Relatively Higher Jet-to-Ambient Temperature Difference (VCR Photos)

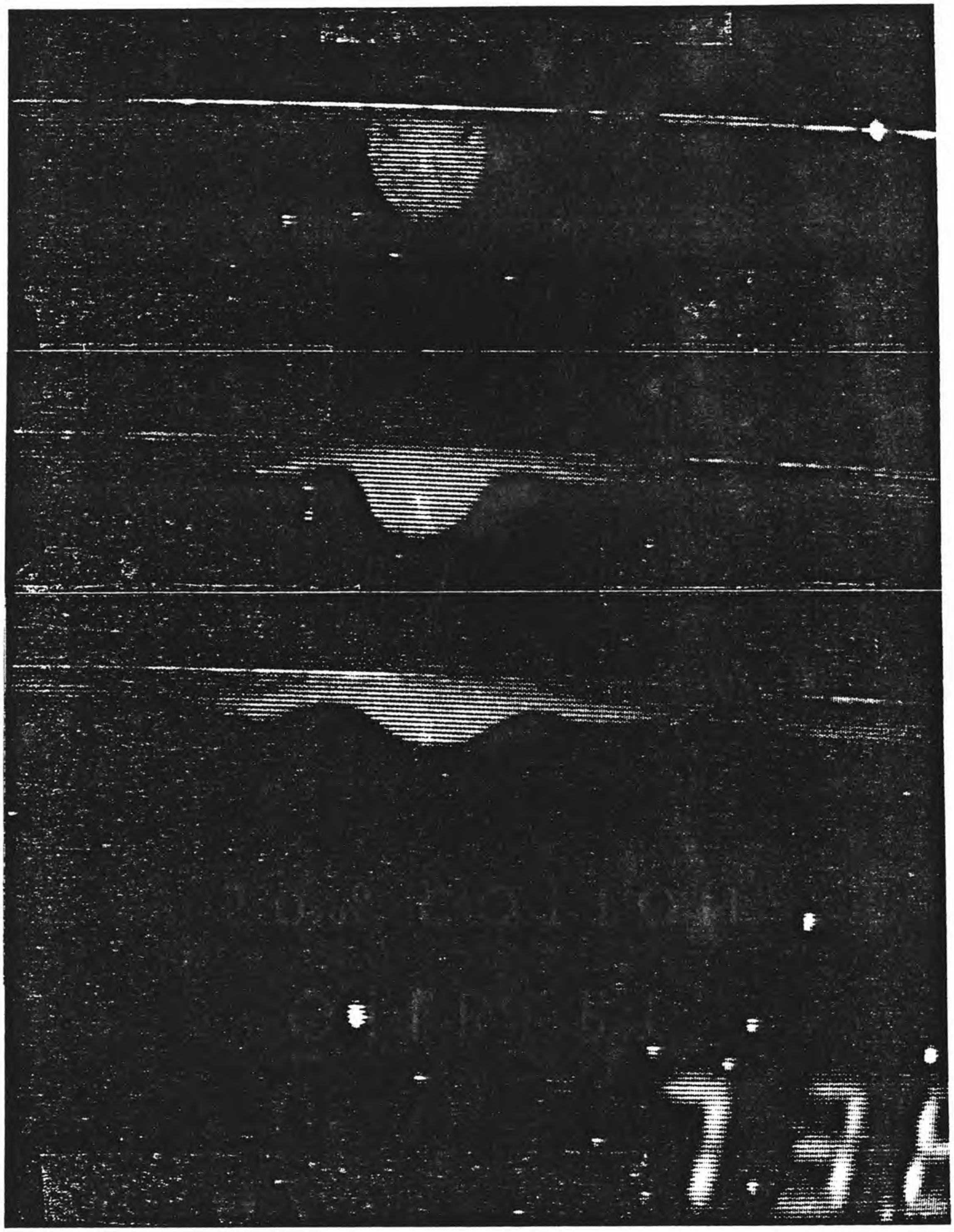

(c): Cross-Sectional Images of the Positively Buoyant Jet at Relatively Higher Jet-to-Ambient Temperature Difference (VCR Photos)

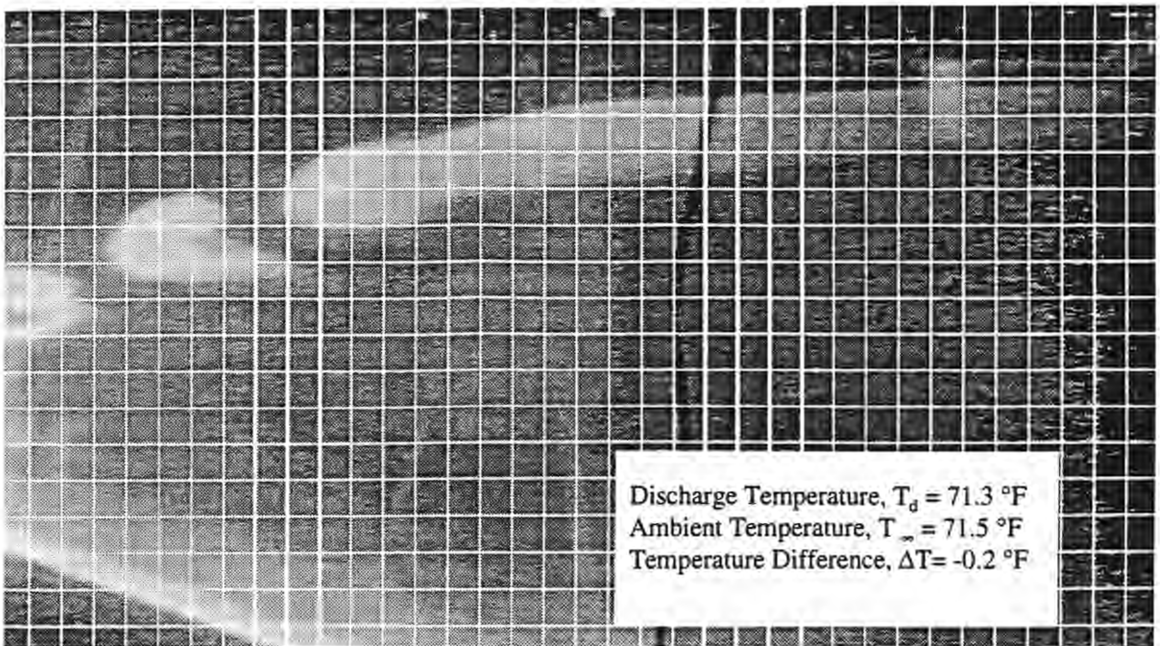

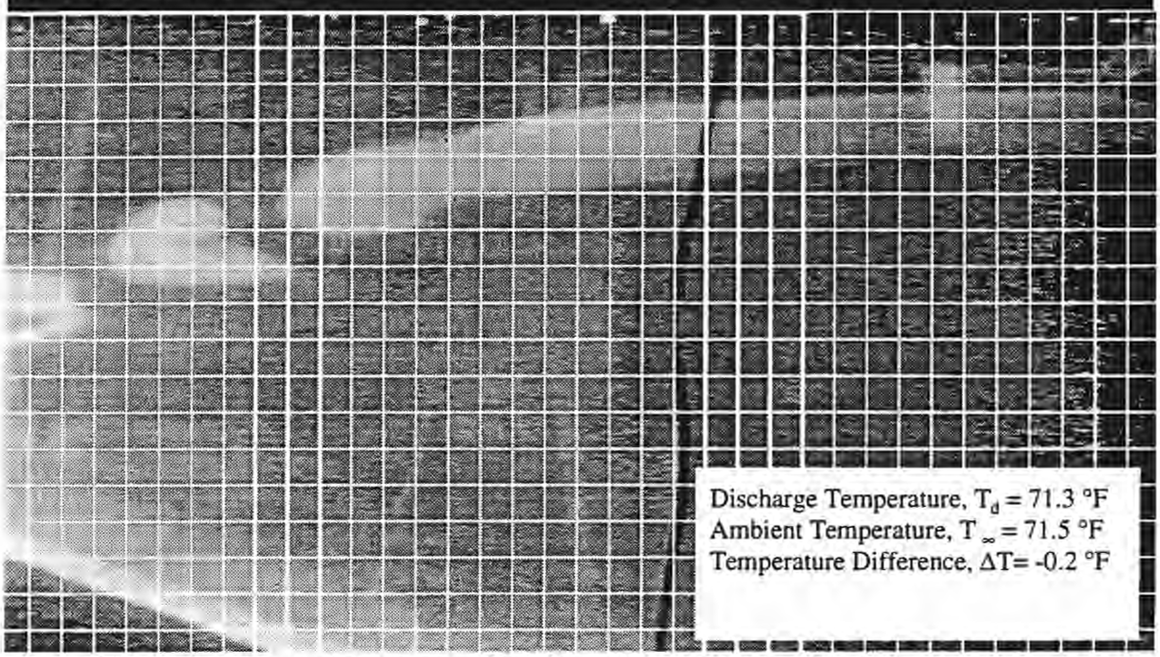

Figure 4.8 (a): Axial Images of the Negatively Buoyant Jet for same Discharge-to-Surrounding Temperature Difference

Ceiling-to-nozzle height, h = 12/16 in
Grid = 0.25 in x 0.25 in
Camera-to-Tank distance : 15.75 in

Water Flow Rate = 0.0230 GPM
Nozzle Inner Diameter D= 0.473 in
Nozzle Reynolds Number, Re =163

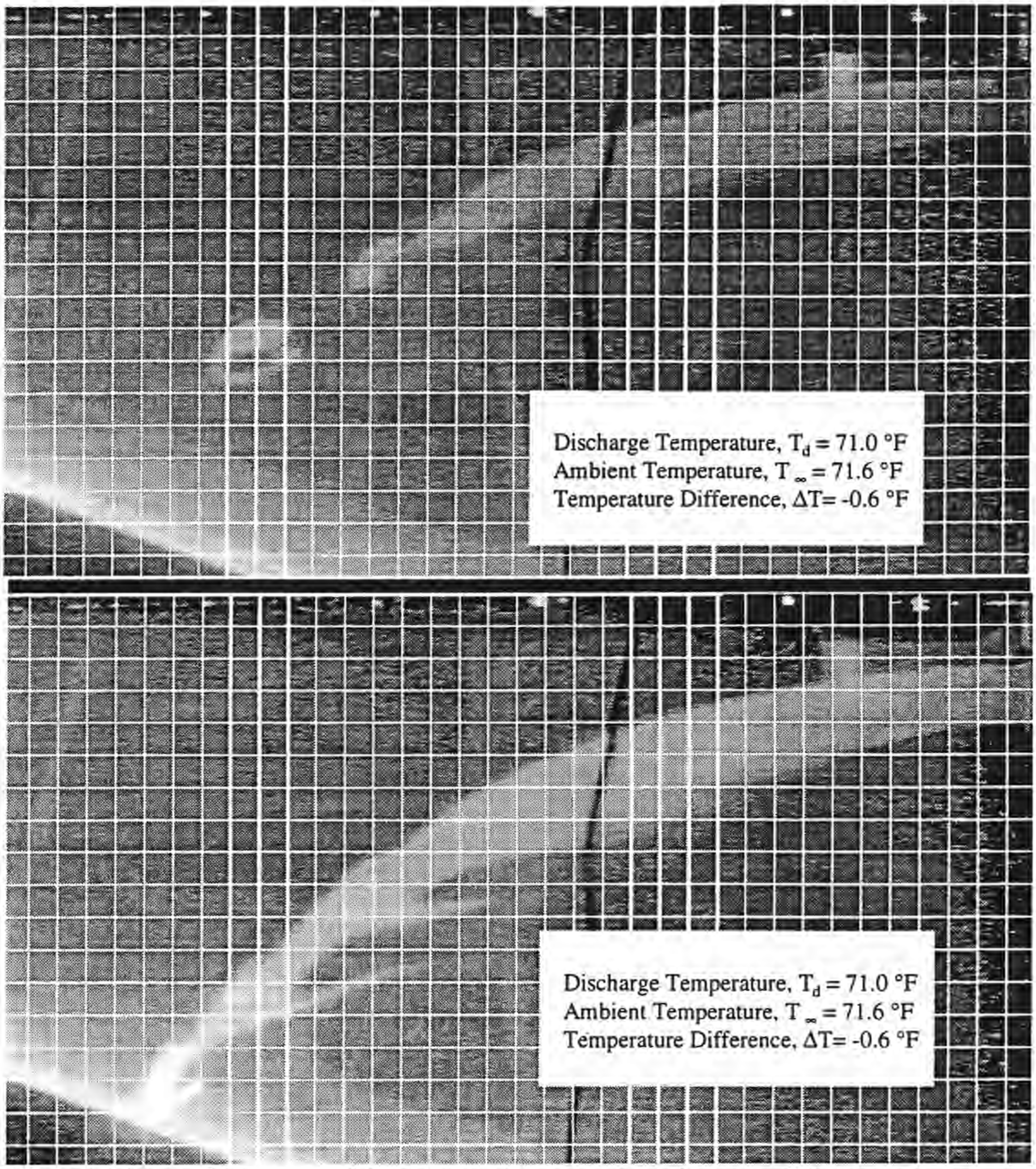

Figure 4.8 (b): Axial Images of the Negatively Buoyant Jet for same Discharge-to-Surrounding Temperature Difference

Ceiling-to-nozzle height, h = 12/16 in
Grid = 0.25 in x 0.25 in
Camera-to-Tank distance : 15.75 in

Water Flow Rate = 0.0230 GPM
Nozzle Inner Diameter D= 0.473 in
Nozzle Reynolds Number, Re =163

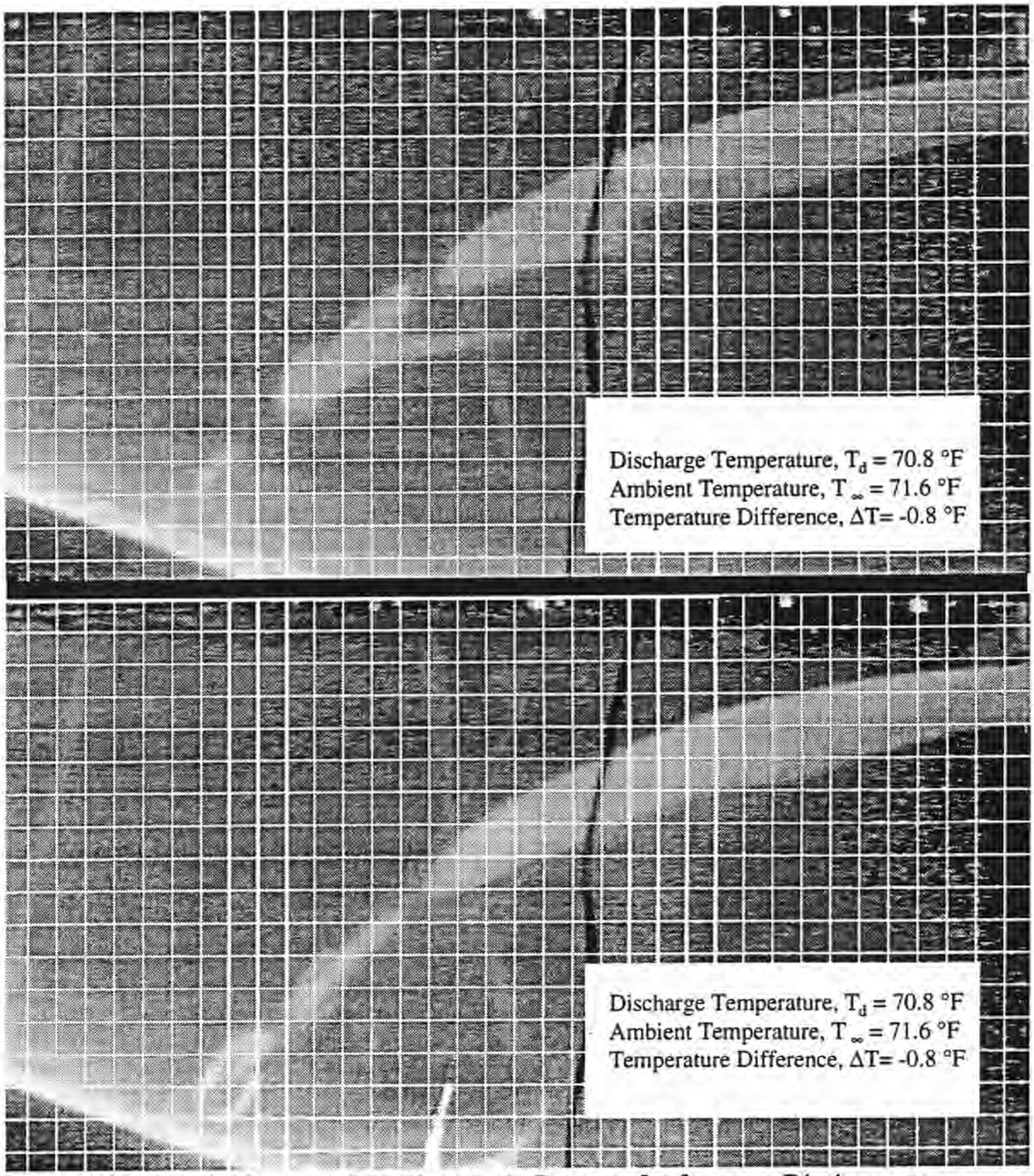

Figure 4.8 (c): Axial Images of the Negatively Buoyant Jet for same Discharge-to-Surrounding Temperature Difference

Ceiling-to-nozzle height, h = 12.6 in
Grid = 0.25 in x 0.25 in
Camera-to-Tank distance : 15.75 in

Water Flow Rate = 0.0230 GPM
Nozzle Inner Diameter D= 0.473 in
Nozzle Reynolds Number, Re =163

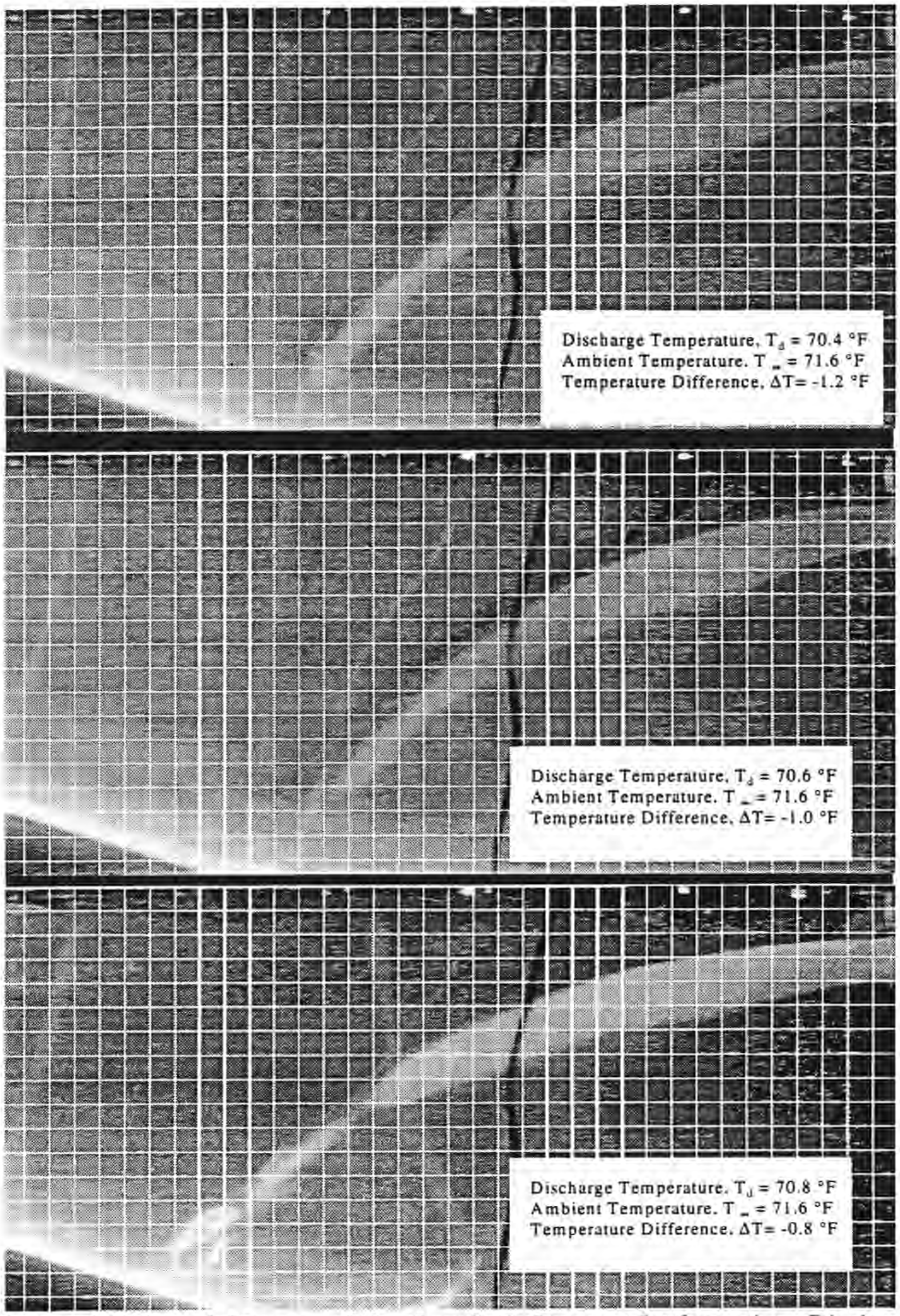

Figure 4.9 (a): Axial Images of the Negatively Buoyant Jet for various Discharge-to-Surrounding Temperature Difference

Ceiling-to-nozzle height, h = 12/16 in
Grid = 0.25 in x 0.25 in
Camera-to-Tank distance : 15.75 in

Water Flow Rate = 0.0230 GPM
Nozzle Inner Diameter D= 0.473 in
Nozzle Reynolds Number, Re =163

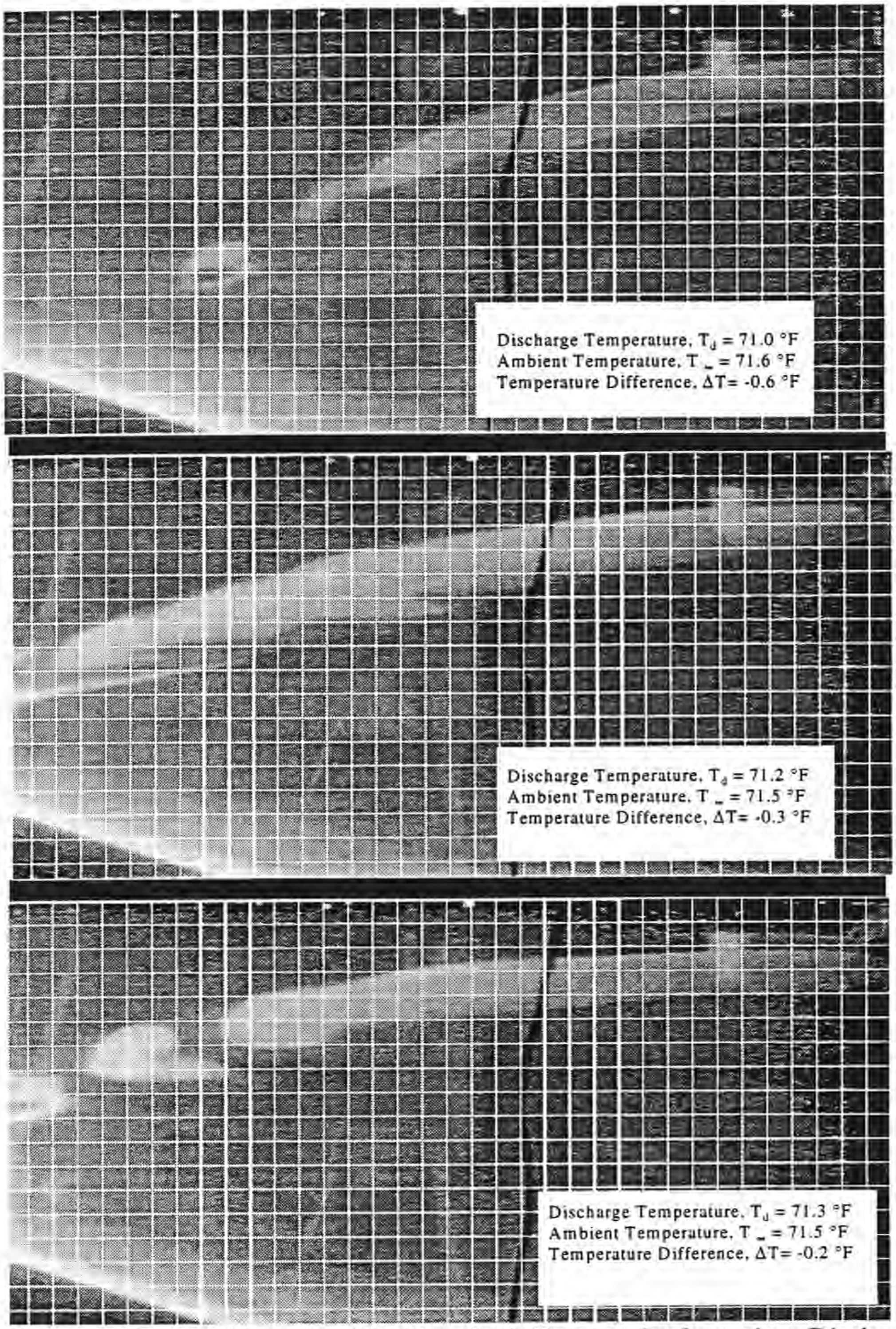

Figure 4.9 (b): Axial Images of the Negatively Buoyant Jet for various Discharge-to-Surrounding Temperature Difference

Ceiling-to-nozzle height, h = 12/16 in
Grid = 0.25 in x 0.25 in
Camera-to-Tank distance : 15.75 in

Water Flow Rate = 0.0230 GPM
Nozzle Inner Diameter D= 0.473 in
Nozzle Reynolds Number, Re =163

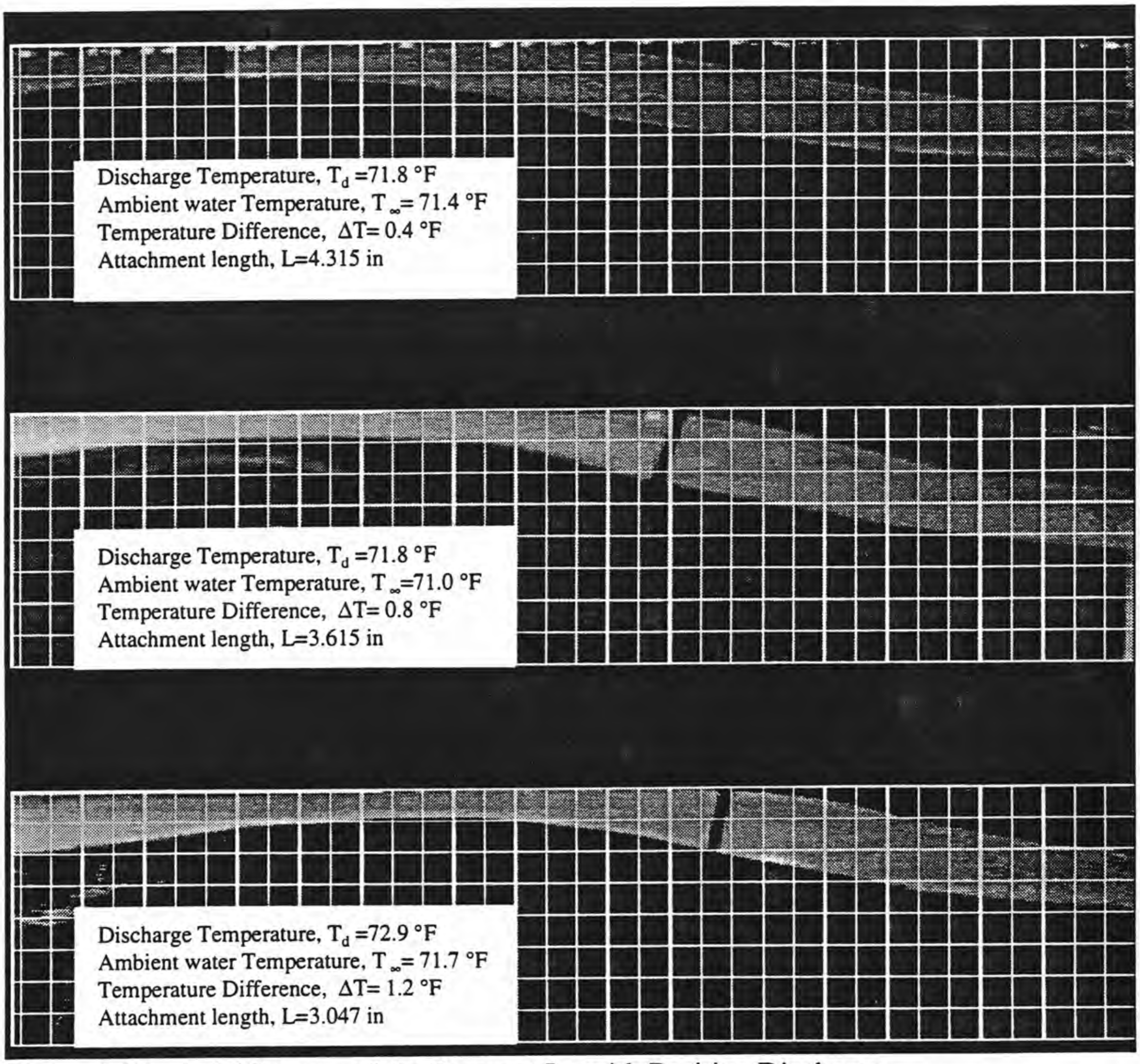

Figure 4.10: Axial Images of the Buoyant Jet with Positive Discharge-to-Surrounding Temperature Difference

Ceiling-to-nozzle height, h = 12/16 in
Grid = 0.25 in x 0.25 in
Camera-to-Tank distance : 15.75 in

Water Flow Rate = 0.0230 GPM
Nozzle Inner Diameter D= 0.473 in
Nozzle Reynolds Number, Re =163

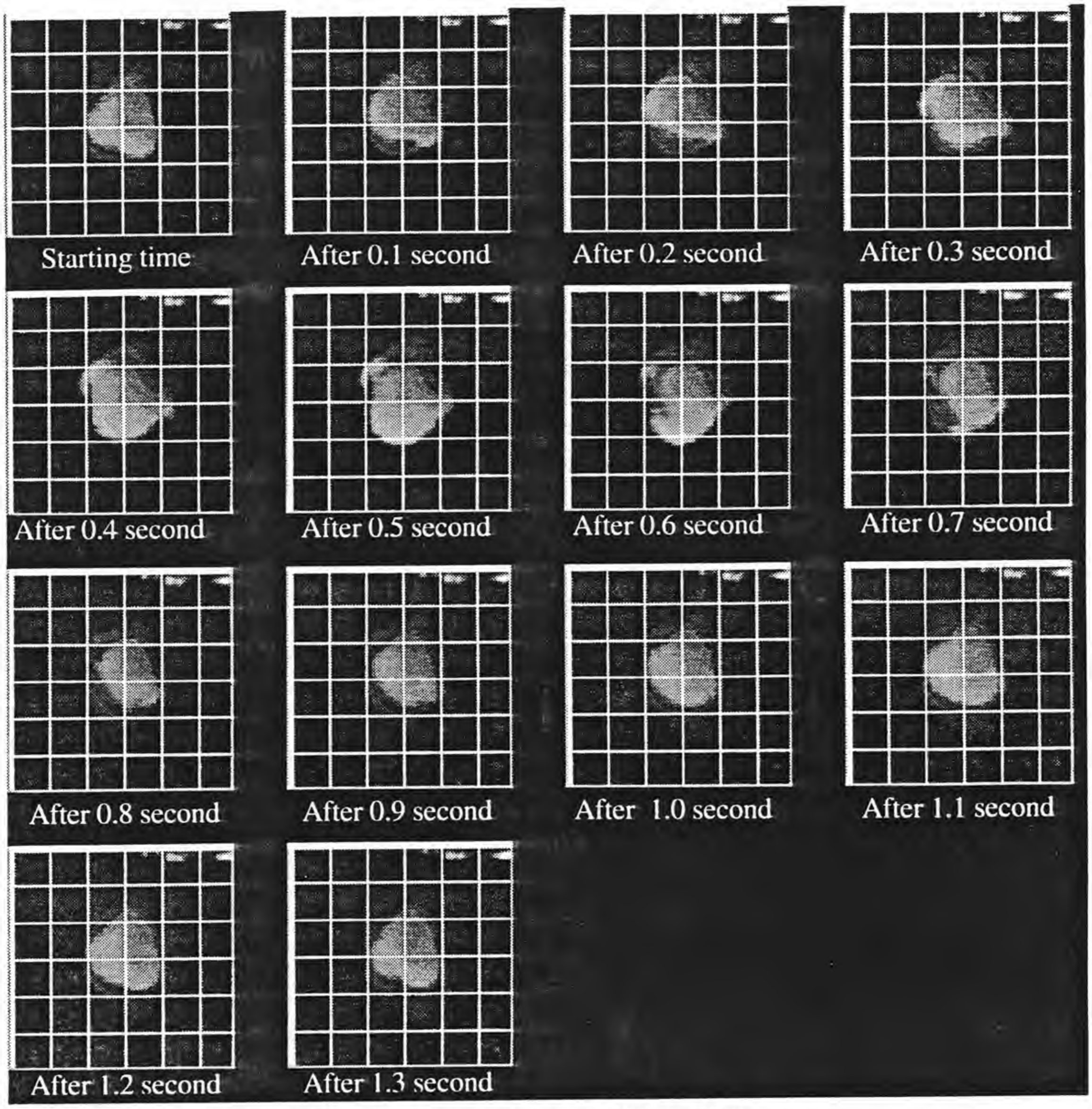

Figure 4.11 (a): Cross-sectional Images of Jet at Higher Flow rate

Ceiling-to-nozzle height, h = 12/16 in
Nozzle Inner Diameter, D = 0.473 in
Grid = 0.25 in x 0.25 in
Camera-to-Tank distance : 7.375 in
Cross-section away from the Nozzle, X= 2.0 in.

Nozzle Reynolds Number, Re = 431
Water Flow Rate = 0.0230 GPM
Discharge Temperature, T_d = 72.1 °F
Ambient Temperature, T_∞ = 70.6 °F
Temperature Difference, ΔT = 1.5 °F

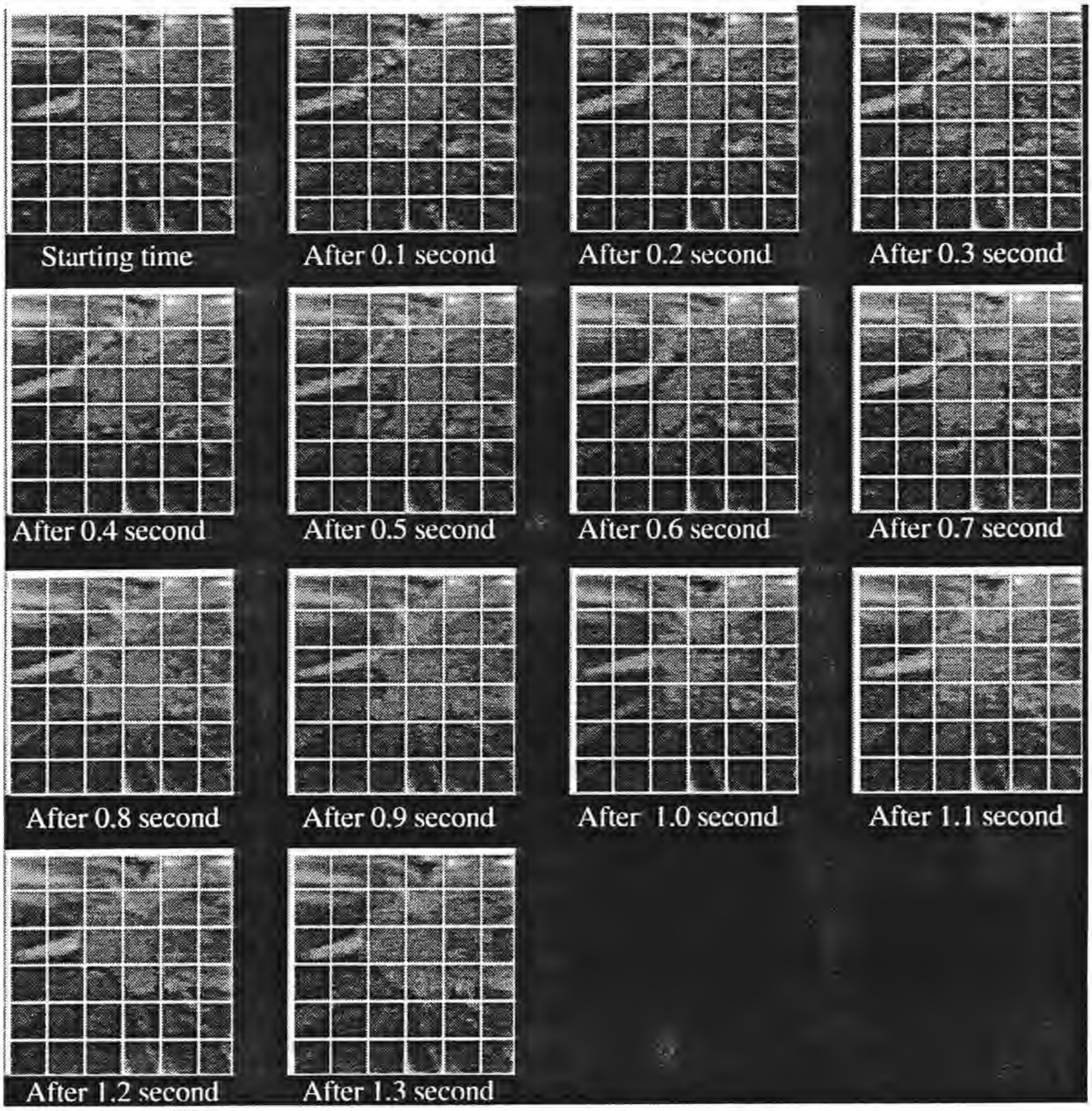

Figure 4.11 (b): Cross-sectional Images of Jet at Higher Flow rate

Ceiling-to-nozzle height, h = 12/16 in	Nozzle Reynolds Number, Re = 543
Nozzle Inner Diameter, D = 0.473 in	Water Flow Rate = 0.78 GPM
Grid = 0.25 in x 0.25 in	Discharge Temperature, T_d = 72.8 °F
Camera-to-Tank distance : 7.375 in	Ambient Temperature, T_∞ = 70.8 °F
Cross-section away from the Nozzle, X= 2.0 in.	Temperature Difference, ΔT = 2.0 °F

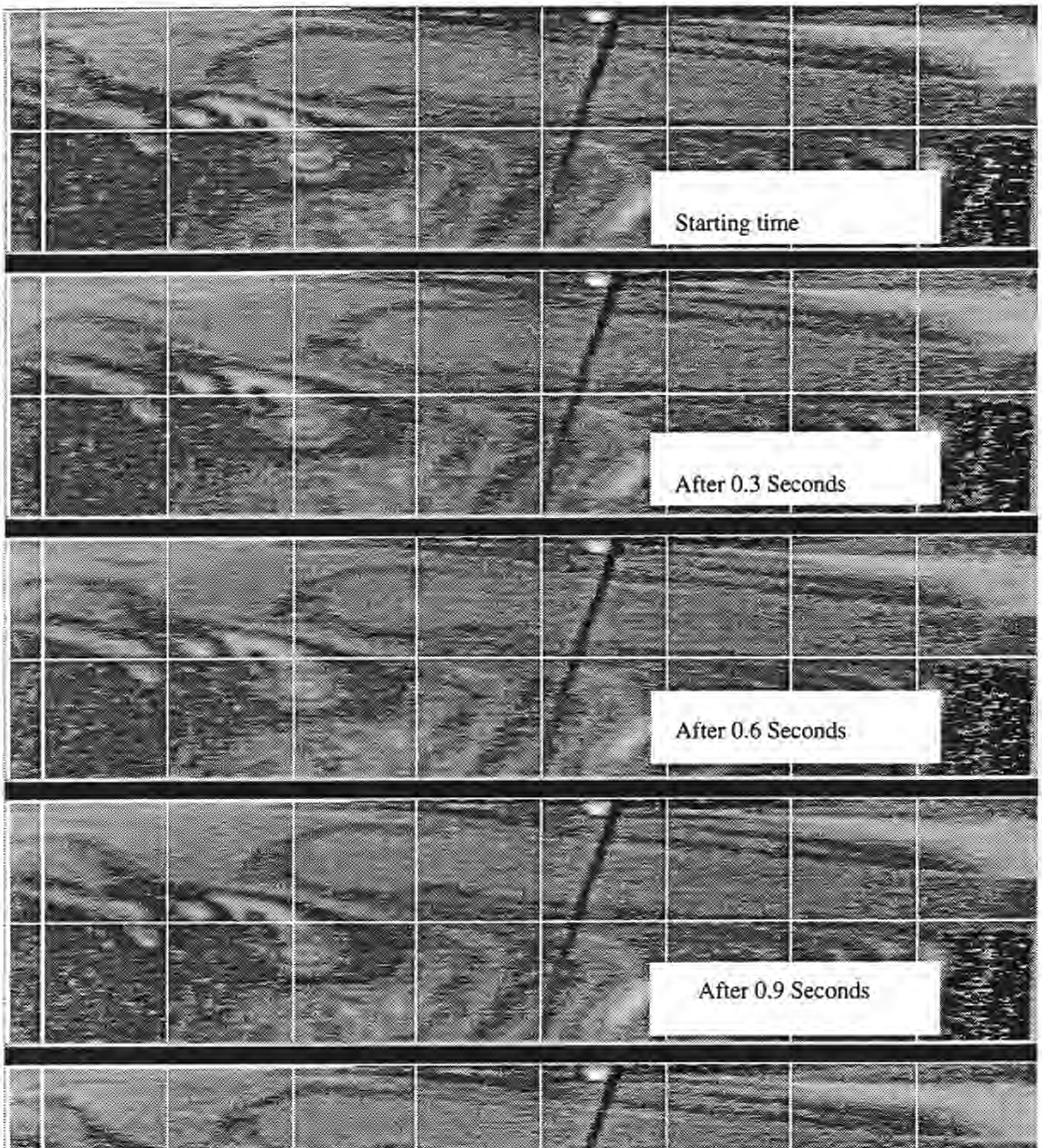

Figure 4.12 (a): Axial Images of Jet at Higher Flow rate

Ceiling-to-nozzle height, h = 12/16 in
Nozzle Inner Diameter D= 0.473 in
Grid = 1.0 in x 1.0 in
Camera-to-Tank distance : 15.75 in

Nozzle Reynolds Number, Re =431
Discharge Temperature, T_d = 72.1 °F
Ambient Temperature, T_∞= 70.6 °F
Temperature Difference, ΔT= 1.5 °F

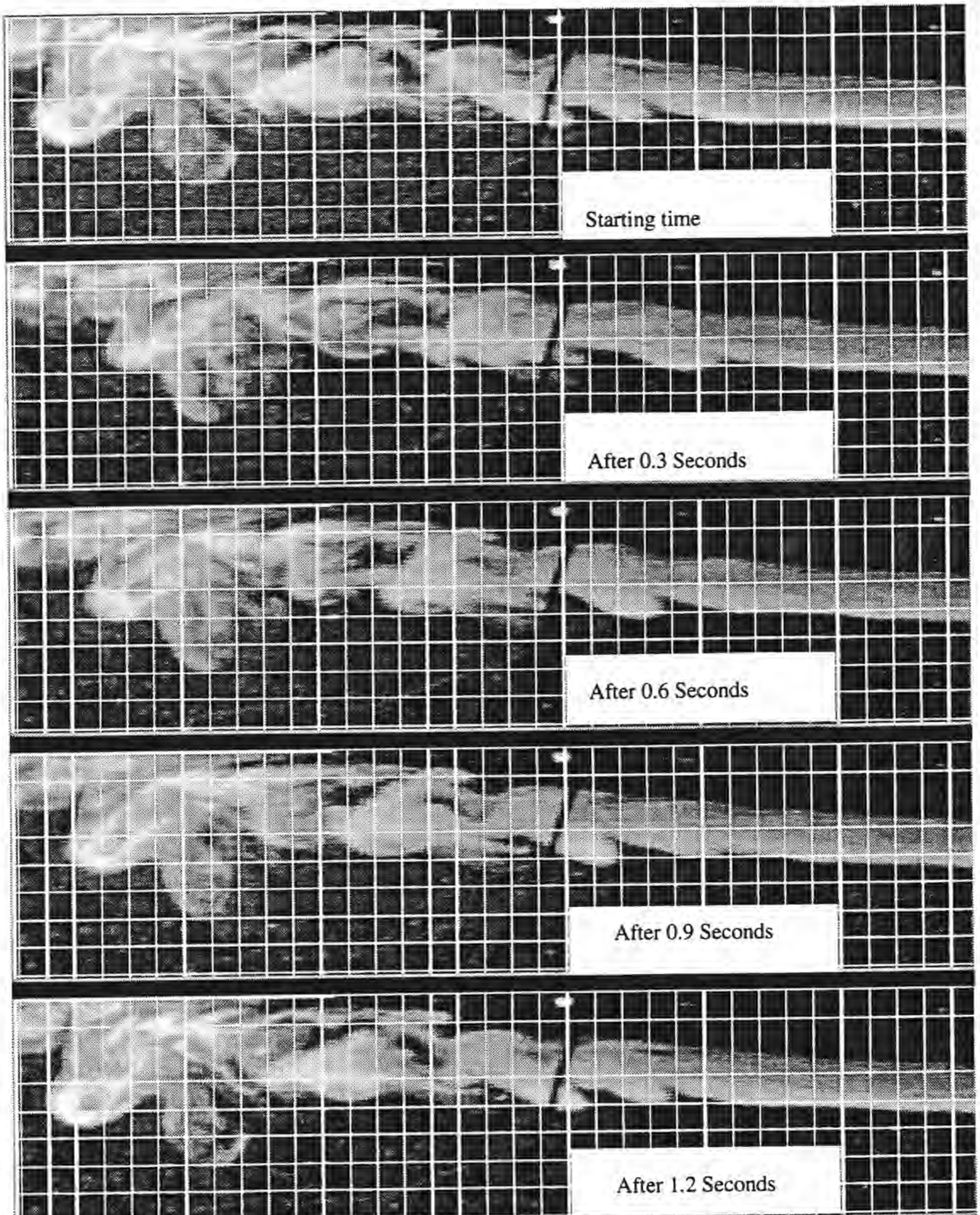

Figure 4.12 (b): Axial Images of Jet at Higher Flow rate

Ceiling-to-nozzle height, h = 12/16 in
Nozzle Inner Diameter D= 0.473 in
Grid = 0.25 in x .25 in
Camera-to-Tank distance : 15.75 in

Nozzle Reynolds Number, Re =543
Discharge Temperature, T_d = 72.8 °F
Ambient Temperature, T_∞= 70.8 °F
Temperature Difference, ΔT= 2.0 °F

Chapter 5

Conclusion and Recommendations

5.1 Summary and Conclusions

This study included an experimental investigation of a laminar circular corner wall jet of water. Flow visualization of an approximately isothermal jet was obtained to provide qualitative and quantitative information about the laminar circular wall jet. The main focus of this study was to look at the effect of varying the jet-to-ceiling spacing on the jet trajectory and attachment to the upper wall. In addition, the effect of buoyancy on the circular wall jet was investigated. Images of both axial and cross-sectional profiles of the jet were obtained for five ceiling-to-nozzle spacing. Approximately neutral buoyant Titanium dioxide (Tio_2) seed particles were injected into the flow to make the jet visible. From the jet images, it was possible to investigate the location of the jet attachment to the upper wall. The results of the measured point of jet attachment to the upper wall were compared with a simple theory based on a modification of a two-dimensional isothermal jet. The theory was not intended to represent the three dimensional wall jet under investigation accurately; however, predictions of the wall attachment length were only about 30% below experimental measurements. Buoyancy effects on the jet were investigated by introducing the jet with different discharge temperatures from that of the surrounding ambient water. Effects of changing the jet flow rate were also investigated. Cross-sectional and axial profile images of the jet were obtained for two flow rates (0.062 GPM and 0.078 GPM). Based on the observations made in this study, the following conclusions were made:

- The jet spreads in the pre-attachment region. After the jet attachment to the upper wall, jet lateral growth becomes much higher than the vertical growth.
- The isothermal jet attachment point moves further away from the nozzle as the nozzle-to-ceiling spacing is increased.
- The jet had a curved trajectory. For the approximately isothermal jet, the jet cross-section started circular then it became elliptical, and flattened before it actually attached to the wall.
- Measurements of the jet to wall attachment length made using the cross-sectional and axial profiles of the jet were in a good agreement.
- The negatively-buoyant water jet had an inverted eye-drop cross-sectional shape. The positively buoyant water jet had an eye-drop cross-sectional shape, and it attached at shorter distances to the wall, depending on the magnitude of the jet-to-ambient temperature difference.
- The negatively buoyant jet, at higher ambient-to-discharge temperature difference, had a two-lobe elongated cross-sectional shape.
- The negatively-buoyant jet necked down and periodic instabilities and breaking up of the jet were observed at large distance from the nozzle exit.

- For high positive jet-to-ambient temperature differences, at the attachment point the jet appeared to split into two lateral streams impinging on the wall, and it had a mushroom shape cross-sectional profile.
- Measured attachment lengths were about 30% higher than predicted by the simple theory of Sawyer (1960) for the turbulent isothermal two-dimensional jet.

5.2 Recommendations:

The following is a list of recommendations for future research

- Extend the flow rate into the turbulent range and more fully investigate the behavior of the jet.
- Make quantitative velocity distribution profiles using LDV or PIV to more accurately determine cross-sectional flow distribution and the location of the attachment streamline.
- Use a more precise temperature control, and use a bigger tank to both minimize adjacent wall influence, and to maintain steady ambient conditions for a longer period of time..
- Develop a more representative three-dimensional model of the jet velocity distribution to better compare with experimental results.
- Investigate the effects of using air in a scaled geometry.
- Use an improved nozzle geometry and take into account the effect of developing and fully-developed inlet flows.

- Use time-averaging to statistically determine the shape of the turbulent jet profiles, and cross-sections.
- Develop a more physically representative model of the jet attachment point which takes into account the three-dimensional characteristics of the jet and the effect of buoyancy.

REFERENCES

- Ayukawa, kyozo and Toshihiko Shakochi. "Analysis of a Jet Attaching to an Offset Parallel Plate". Bulletin of the JSME, vol. 19, No. 130, April 1976. PP. 395-401.
- Blevins, R., Applied Fluid Dynamics Handbook, Van Nostrand Reinhold Company Inc., New York, 1984.
- Borque, C. and Newman, B.G. "Reattachment of a Two-Dimensional, Incompressible Jet to an Adjacent Flat Plate". The Aeronautical Quarterly, Vol. XI, August 1960 PP. 201-231.
- Davis, M.R. and H. Winarto "Jet Diffusion from a Circular Nozzle above a Solid Plane". Journal of Fluid Mechanics Vol. 101, Part 1, 1980 PP. 201-221.
- Dodds, J.I. 1960 Ph.D. Thesis. Cambridge University.
- El-Taher R., M." Attachment of Ventilated Jets to Rough Boundaries". Aeronautical Journal, December 1982 PP 380-383.
- El-Taher R., M. "Experimental Investigation of Curvature effects on Ventilated Wall Jets". AIAA Journal, Vol. 21, No. 11, November 1983 PP. 1505-1511.
- El-Taher R., M. "Similarity in Ventilated Wall Jets". AIAA Journal, 1982. PP. 161-166.

- Gregory-Smith, D.G. and M.J. Hawkins. "The Development of an Axisymmetric Curved Turbulent Wall Jet". Int. Journal of Heat and Fluid Flow, Vol. 12 , No. 4, December 1991.
- Hawkins, A. 1994. "Fluid Dynamics Characteristics of Air Distribution in a Full Size Test Chamber Using a High Side-Wall Grille and a Linear Ceiling Diffuser for Isothermal and Nonisothermal Conditions.", MS. Thesis, Kansas State University.
- Hoch, J. and L.M. Jiji." Two-Dimensional Turbulent Offset Jet-Boundary Interaction". Journal of Fluid Engineering, Vol. 103, March 1981 PP 154-161.
- Marster, G.F. "The Attachment of A Ventilated Jet to an Inclined Plane Wall". Aeronautical Quarterly, Vol. 29, May 1978.
- Newman, B.G., R.P. Patel, S.B. Savage, and H.K. Tjio. "Three Dimensional Wall Jet Originating from a Circular Orifice". Aeronautical Quarterly Vol. 23, 1972 PP. 188-200.
- Sawyer R.A." The Flow Due to 2-Dimensional Jet Issuing Parallel to a Flat Plate". Journal of Fluid Mechanics, Vol. 9, Part 4, 1960. PP. 543-561.
- Sawyer R.A." Two-Dimensional Reattaching Jet Flows Including the Effects of Curvature on Entrainment". Journal of Fluid Mechanics, Vol. 17, 1963. PP. 481-498.

* Schlichting, H., Boundary Layer Theory, 7th Ed., McGraw-Hill, New York, 1979.
* Shakouchi, Toshihiko, Yoshinori Onohara, and Seizo Kato. "Analysis of a Two- Dimensional, Turbulent Wall Jet Along a Circular cylinder (Velocity and Pressure Distributions)". JSME International Journal, Series II, Vol. 32, NO. 3, 1989 PP. 332-339.
* Vaddepally, R., 1995. "Dynamic Characteristics of A Laser-Based Optical Position Sensor with Applications to Endpoint Measurement. ",MS. Thesis, Kansas State University.

APPENDIX A

Camera Calibration

It was necessary to determine the number of pixels per inch for the image of an object which was located at a certain distance away from the camera. To allow extracting the actual size of an object from its image, the scale factor was defined as the inverse of the number of pixels per inch, and was determined experimentally and verified theoretically. This permitted determination of the image size in inches by multiplying the number of image pixels by the appropriate scale factor. The pixels were rectangular in shape, hence the number of pixels per inch in the horizontal direction was different from the number of pixels per inch in the vertical direction. Therefore every image had two scale factors, a horizontal scale factor defining the number of horizontal pixels per inch, and a vertical scale factor specifying the number of vertical pixels per inch. This Appendix contains the calibration procedures and the calculation of the horizontal and vertical scale factors.

Since the camera/tank orientation was different in the cross sectional and longitudinal jet profiling tests, the camera calibration was made independently for each set of tests. For the cross sectional profiling calibration, the camera was aligned such that the optical axis of the camera coincided with the centerline of the jet exit opening. A typical picture showing the alignment of the camera for the cross-sectional calibration is given in Figure A.1(a). The camera-to-glass spacing was fixed at 7.25 in; hence, the only variable spacing left was the distance between the object of interest and the glass-water interface. The purpose of the cross-sectional profiling was to image the jet cross section at different locations away from the plane of the jet discharge. Therefore, the cross-sectional calibration was based on the distance along the nozzle axis measured away from the back wall of the test chamber. A transparent plastic scale, with horizontal and vertical grids, was mounted on a half inch diameter, one foot long, brass tube that protruded up to ten inches from the jet opening. The scale was illuminated with a laser-generated light sheet, and an image of the scale was grabbed for 8 positions along the jet axis. A typical image of the scale is shown in Figure A.1(b). The scale location in the first image was initially flush with the back wall of the test chamber. It was then incremented by one inch increments toward the camera for the remainder of the images. For the longitudinal profiling calibration, two separate calibrations were made. In the first calibration, the camera was positioned 12.5 inches away from the tank wall. The camera field of view covered about 6.5 inches in front of the back wall of the test chamber along the nozzle axis. For the second calibration, the field of view covered about 8.5 inches and the camera-to-glass spacing was 15.75 inches. The scale was glued to a 90° ,0.25 in x0.25 in extended plastic angle. The plastic angle was clamped by a paper clip and a C-clamp to the Plexiglas plate simulating the ceiling of the apparatus. A typical picture of the scale for the longitudinal calibration is in Figure A.1(c). In each case three images of the scale were grabbed. In one of the images, the scale was vertically positioned in the same plane as the centerline of the jet. For the other images, the scale was positioned vertically at the outer edges of the jet opening area (about one radius on either side of the central plane of the jet).

Calculating the horizontal and vertical scale factors of an image, when the object was at a certain location along the optical axis, involved the following procedure: Due to imperfect camera/tank alignment, some small slope of the pixel array was likely to occur. An attempt was made to account for any slope in the pixel array during calibration. On a calibration image, a horizontal scale line close to the optical axis was chosen as a reference line. The vertical and horizontal pixel locations of the 1/2 inch marks along this line were identified manually using the XView[1] image editor. The pixel identification process was repeated for a vertical scale line located in the vicinity of the optical axis. Since the square of the distance along a scale line equals the sum of the squares of the horizontal and vertical distances, a distance along the scale can be expressed according to the following equation:

$$d^2 = k_x^{\,2} \cdot \Delta x^2 + k_y^{\,2} \cdot \Delta y^2 \qquad \text{(A.1)}$$

where d is actual scale distance in inches either horizontal or vertical, k_x and k_y are the horizontal and vertical scale factors in inches per pixel, and Δx and Δy are the horizontal and vertical number of pixels corresponding to the distance d. The scale factors are assumed to be constant at a given distance from the camera which is consistent with the paraxial approximation used in Appendix B to verify the measured scale factors theoretically. Dividing the above equation by Δx for the horizontal reference line, and by Δy for the vertical reference line gives the following two equations:

[1] Xview is an image editing software available on the KSU UNIX Network

$$\left(\frac{d_h}{\Delta x}\right)^2 = k_x^2 + k_y\left(\frac{\Delta y}{\Delta x}\right)^2 \qquad (A.2)$$

$$\left(\frac{d_v}{\Delta y}\right)^2 = k_y^2 + k_x\left(\frac{\Delta x}{\Delta y}\right)^2 \qquad (A.3)$$

where d_v is a distance along the vertical reference line, and d_h is a distance along the horizontal reference line. The ratio of d_h to Δx in Equation(A.2) is the slope of the horizontal reference line which will be denoted by m_h. Similarly the ratio of d_v to Δy in Equation(A.3) is the slope of the vertical reference line and it is going to be denoted by m_v. The ratio of Δy to Δx in Equation(A.2) is the slope of the vertical pixel location on for the horizontal scale line, denoted by m_{yx}. In Equation(A.3), the ratio of Δx to Δy is the slope of the horizontal pixel location on for the vertical scale line, denoted by m_{xy}. Substituting the slope of the horizontal scale line (m_h) and the slope of the vertical pixel locations for the horizontal scale line m_{yx} into Equation (A.2), yields for the horizontal scale factor

$$k_x^2 = m_h^2 - (m_{yx}k_y)^2, \quad m_h = \frac{d}{\Delta x}, \quad m_{yx} = \frac{\Delta y}{\Delta x} \qquad (A.4)$$

Similarly, substituting the slope of the vertical scale line (m_v) and the slope of the horizontal pixel locations for the vertical scale line m_{xy} into Equation (A.3), the vertical scale factor becomes

$$k_y^2 = m_v^2 - (m_{xy}k_x)^2, \quad m_v = \frac{d}{\Delta y}, \quad m_{xy} = \frac{\Delta x}{\Delta y} \qquad (A.5)$$

The slope of the horizontal scale line m_h was determined by least square fit between the distance measured on the scale along the horizontal scale line in inches and the horizontal pixel locations measured on the screen. The slope of the vertical scale line m_v was determined by linear least square fit to the distance measured on the scale along the vertical scale line (in inches) and the vertical pixels locations measured on the screen. The slope of the change in the vertical pixel location along the horizontal scale line m_{yx} was determined by least fit between the change in the vertical and horizontal pixel locations along the horizontal scale line. The slope of the change in the horizontal pixel location along the vertical scale line m_{xy} was determined by a linear least fit to the change in the horizontal and vertical pixel locations along the vertical scale line. The linear fit through the measured horizontal and vertical scale factor for the cross-sectional defines a linear expression for the scale factor as a function of the distance along the optical axis measured away from the nozzle exit (X). The best fit relations for horizontal and vertical scale factors (kx and ky) respectively become

$$k_x(X) = 0.0137786 - 0.000746\,X \tag{A.6}$$

$$k_y(X) = 0.0110514 - 0.000605\,X \tag{A.7}$$

Figure A.2 compares the scale factors for the longitudinal and cross sectional calibration with simple linear optics theory developed in Appendix B. The data for the cross-sectional calibration is presented in Table A.1 and Table A.2. The longitudinal calibration data is in Table A.3 and Table A.4.

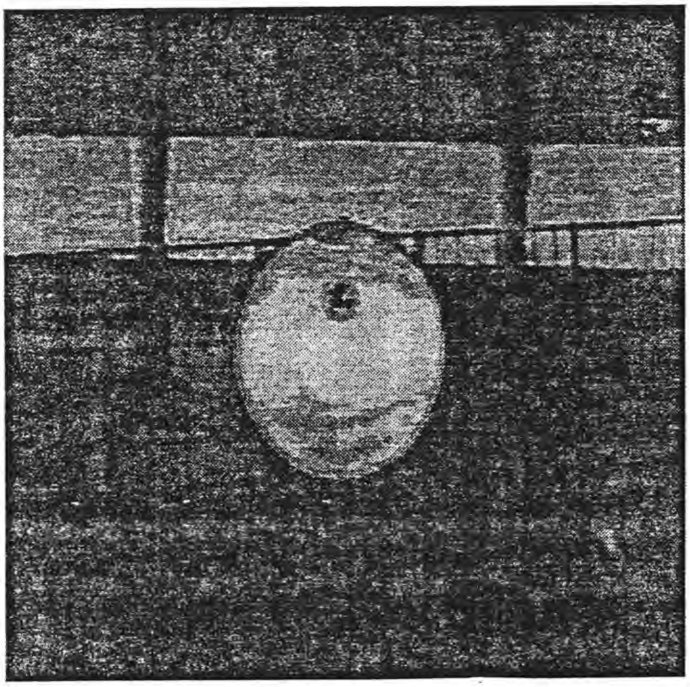

Figure A.1(a): Cross-Sectional Calibration Camera Alignment

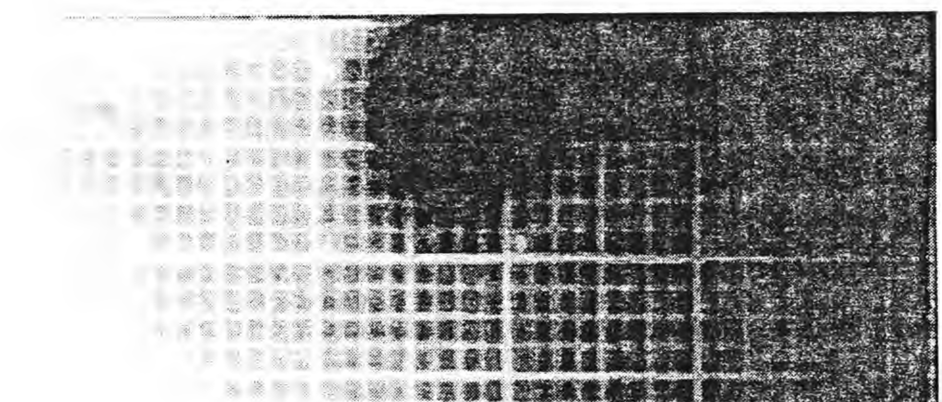

Figure A.1(b): Typical Scale Image of the Cross-Sectional Calibration

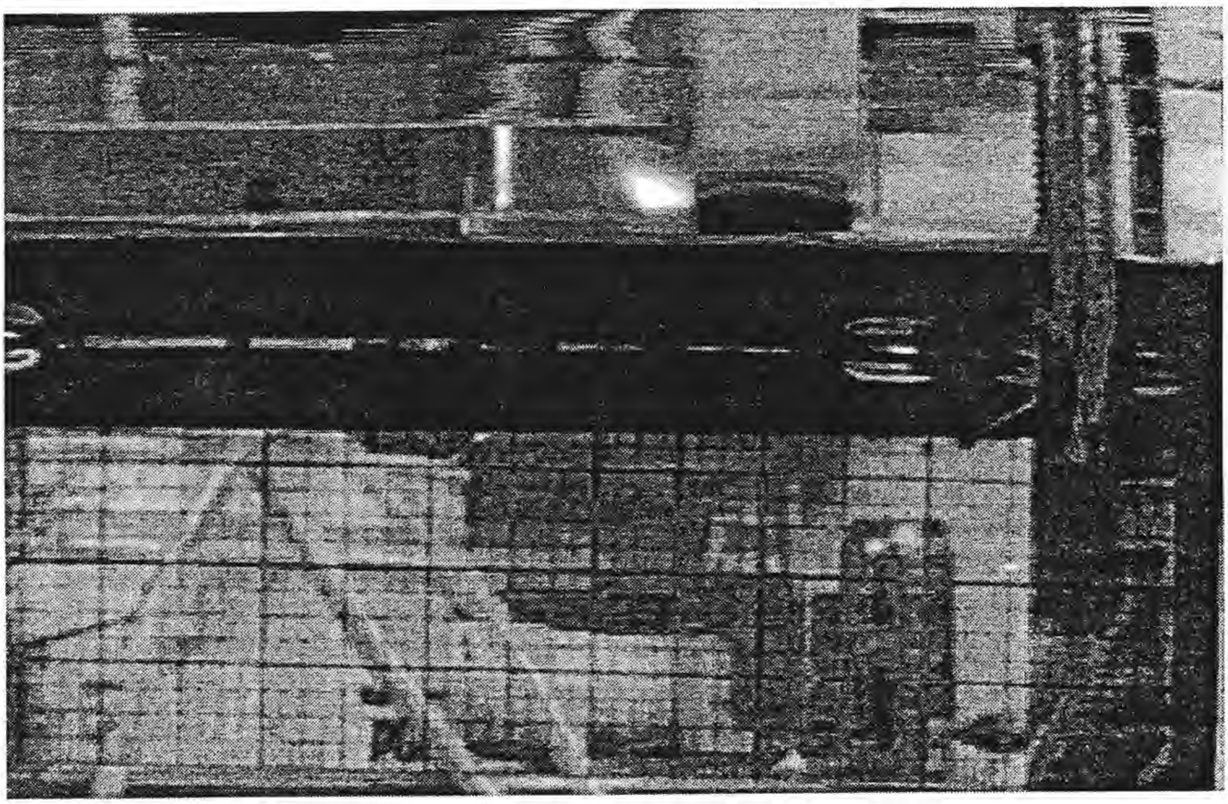

Figure A.1(c): Typical Scale Image of the Axial Calibration

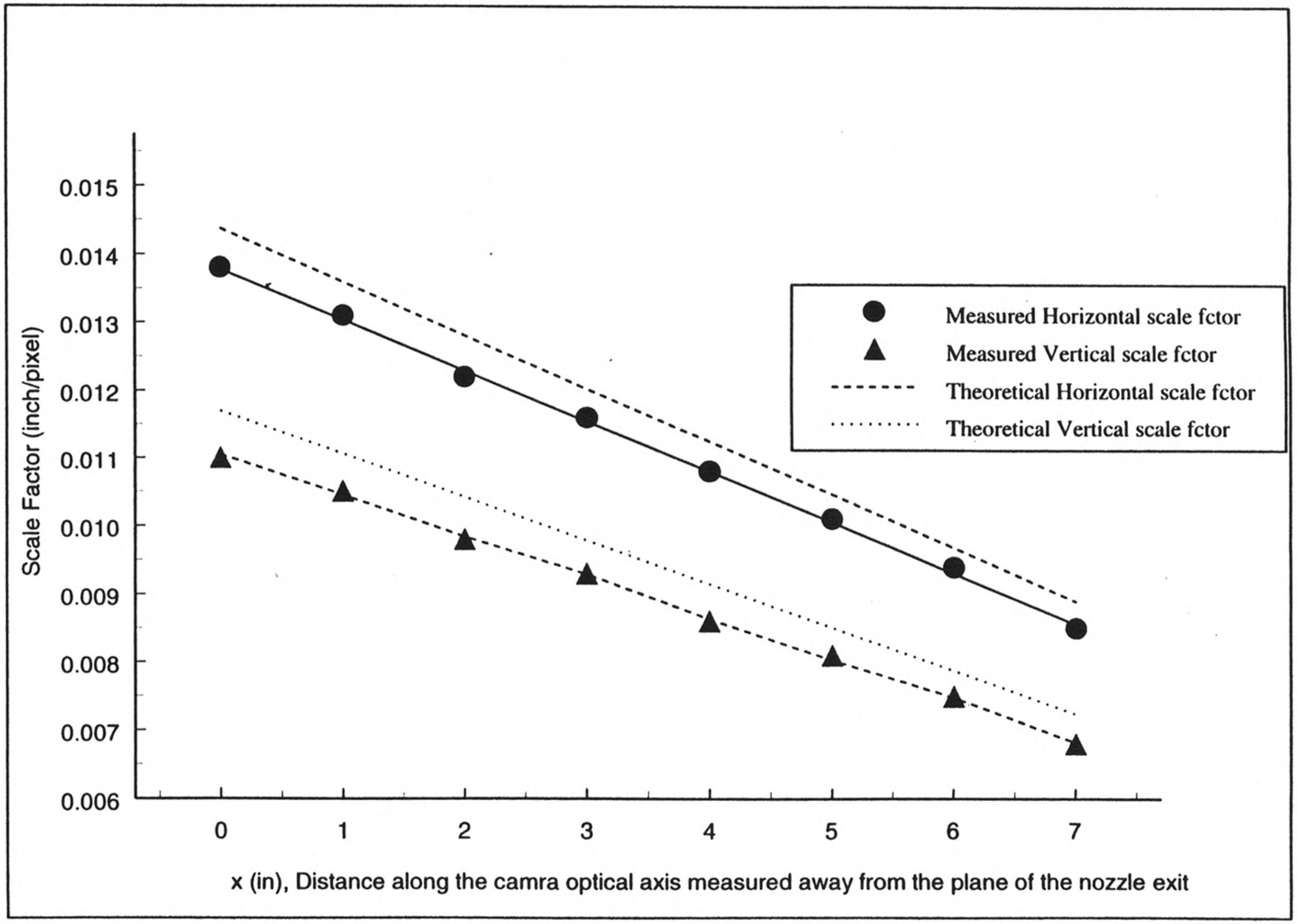

Figure A.2: Verifying Measured Cross-Sectional Scale Factors with Theoretical Prediction

Scale Distance	Screen Coordinates		Screen Distance		Calculated Distance	
d	x	y	Δx	Δy	d	Δy
inch	Pixel	Pixel	Pixel	Pixel	inch	Pixel
0.00	92	375	0	0	0.000	0.000
0.25	110	375	18	0	0.248	0.156
0.50	127	376	35	1	0.483	0.304
0.75	146	376	54	1	0.745	0.468
1.00	164	376	72	1	0.994	0.625
1.25	182	376	90	1	1.242	0.781
1.50	200	376	108	1	1.491	0.937
1.75	219	376	127	1	1.753	1.102
2.00	236	376	144	1	1.987	1.249
2.25	255	377	163	2	2.250	1.414
2.50	273	377	181	2	2.498	1.570
2.75	291	377	199	2	2.747	1.726
3.00	309	377	217	2	2.995	1.883
3.25	327	377	235	2	3.243	2.039
3.50	346	377	254	2	3.506	2.204
3.75	364	377	272	2	3.754	2.360
4.00	382	377	290	2	4.002	2.516
horizontal scale line slope, m_h					0.01380 in/pixel	
vertical pixel distance slope, m_{yx}					0.00868 pixel/pixel	
horizontal scale factor, k_x					0.01380 in/pixel	

Table a.1 (a): Scale Positioned at the Nozzle Exit, (X = 0 in)

Scale Distance	Screen Coordinates		Screen Distance		Calculated Distance	
d	x	y	Δx	Δy	d	Δy
inch	Pixel	Pixel	Pixel	Pixel	inch	Pixel
0.00	81	375	0	0	0.000	0.000
0.25	100	375	19	0	0.249	0.431
0.50	119	376	38	1	0.497	0.862
0.75	138	376	57	1	0.746	1.292
1.00	156	380	75	5	0.981	1.701
1.25	176	380	95	5	1.243	2.154
1.50	195	380	114	5	1.491	2.585
1.75	214	380	133	5	1.740	3.016
2.00	233	380	152	5	1.988	3.447
2.25	253	380	172	5	2.250	3.900
2.50	272	380	191	5	2.498	4.331
2.75	291	380	210	5	2.747	4.762
3.00	310	380	229	5	2.995	5.193
3.25	330	380	249	5	3.257	5.646
3.50	349	380	268	5	3.505	6.077
horizontal scale line slope, m_h					0.01308 in/pixel	
vertical pixel Distance slope, m_{yx}					0.00028 pixel/pixel	
horizontal scale factor, k_x					0.01038 in/pixel	

Table a.1 (b): Scale Positioned 1 inch away from the Nozzle Exit, (X = 1 in)

Table A.1: Cross-Sectional Tests Camera Calibration:
Horizontal Scale Factor Data

Scale Distance	Screen Coordinates		Screen Distance		Calculated Distance	
d	x	y	Δx	Δy	d	Δy
inch	Pixel	Pixel	Pixel	Pixel	inch	Pixel
0.00	70	388	0	0	0.000	0.000
0.25	91	387	21	-1	0.256	-0.577
0.50	111	387	41	-1	0.501	-1.126
0.75	131	386	61	-2	0.745	-1.675
1.00	151	386	81	-2	0.989	-2.224
1.25	172	385	102	-3	1.246	-2.800
1.50	193	385	123	-3	1.502	-3.377
1.75	213	384	143	-4	1.746	-3.926
2.00	233	384	163	-4	1.991	-4.475
2.25	254	383	184	-5	2.247	-5.052
2.50	275	382	205	-6	2.504	-5.628
2.75	295	382	225	-6	2.748	-6.177
3.00	316	381	246	-7	3.004	-6.754
horizontal scale line slope, m_h					0.01221 in/pixel	
vertical pixel Distance slope, m_{yx}					-0.02750 pixel/pixel	
horizontal scale factor, k_x					0.01221 in/pixel	

Table A.1 (c): Scale Positioned 2 inch away from the Nozzle Exit, (X = 2 in)

Scale Distance	Screen Coordinates		Screen Distance		Calculated Distance	
d	x	y	Δx	Δy	d	Δy
inch	Pixel	Pixel	Pixel	Pixel	inch	Pixel
0.00	57	393	0	0	0.000	0.000
0.25	78	392	21	-1	0.244	-0.336
0.50	100	392	43	-1	0.499	-0.687
0.75	121	392	64	-1	0.742	-1.023
1.00	143	392	86	-1	0.997	-1.374
1.25	163	392	106	-1	1.229	-1.694
1.50	185	391	128	-2	1.485	-2.046
1.75	207	391	150	-2	1.740	-2.397
2.00	228	390	171	-3	1.983	-2.733
2.25	250	390	193	-3	2.238	-3.085
2.50	272	390	215	-3	2.494	-3.436
2.75	294	389	237	-4	2.749	-3.788
3.00	316	389	259	-4	3.004	-4.139
3.25	338	388	281	-5	3.259	-4.491
3.50	359	388	302	-5	3.503	-4.827
horizontal scale line slope, m_h					0.01160 in/pixel	
vertical pixel Distance slope, m_{yx}					0.01600 pixel/pixel	
horizontal scale factor, k_x					0.01160 in/pixel	

Table A.1 (d): Scale Positioned 3 inch away from the Nozzle Exit, (X = 3 in)

Table A.1 Cross-Sectional Tests Camera Calibration:
Horizontal Scale Factor Data

Scale Distance	Screen Coordinates		Screen Distance		Calculated Distance	
d	x	y	Δx	Δy	d	Δy
inch	Pixel	Pixel	Pixel	Pixel	inch	Pixel
0.00	45	400	0	0	0.000	0.000
0.25	68	399	23	-1	0.248	-0.506
0.50	91	399	46	-1	0.496	-1.012
0.75	114	399	69	-1	0.744	-1.518
1.00	136	398	91	-2	0.982	-2.002
1.25	160	398	115	-2	1.241	-2.530
1.50	183	397	138	-3	1.489	-3.036
1.75	207	397	162	-3	1.748	-3.564
2.00	230	396	185	-4	1.996	-4.070
2.25	253	395	208	-5	2.244	-4.576
2.50	277	395	232	-5	2.503	-5.104
2.75	300	394	255	-6	2.751	-5.610
3.00	323	394	278	-6	2.999	-6.116
3.25	346	393	301	-7	3.247	-6.623
3.50	370	393	325	-7	3.506	-7.151
horizontal scale line slope, m_h					0.01079 in/pixel	
vertical pixel Distance slope, m_{yx}					-0.02200 pixel/pixel	
horizontal scale factor, k_x					0.01079 in/pixel	

Table A.1 (e): Scale Positioned 4 inch away from the Nozzle Exit, (X = 4 in)

Scale Distance	Screen Coordinates		Screen Distance		Calculated Distance	
d	x	y	Δx	Δy	d	Δy
inch	Pixel	Pixel	Pixel	Pixel	inch	Pixel
0.00	32	416	0	0	0.000	0.000
0.25	56	415	24	-1	0.242	-1.553
0.50	81	414	49	-2	0.494	-3.172
0.75	106	412	74	-4	0.746	-4.790
1.00	130	410	98	-6	0.988	-6.343
1.25	155	408	123	-8	1.240	-7.962
1.50	180	407	148	-9	1.492	-9.580
1.75	205	405	173	-11	1.744	-11.198
2.00	229	404	197	-12	1.986	-12.751
2.25	255	402	223	-14	2.249	-14.434
2.50	280	400	248	-16	2.501	-16.053
2.75	305	398	273	-18	2.753	-17.671
3.00	329	396	297	-20	2.995	-19.224
3.25	354	395	322	-21	3.247	-20.843
3.50	380	393	348	-23	3.509	-22.525
horizontal scale line slope, m_h					0.01008 in/pixel	
vertical pixel Distance slope, m_{yx}					-0.06470 pixel/pixel	
horizontal scale factor, k_x					0.01007 in/pixel	

Table A.1 (f): Scale Positioned 5 inch away from the Nozzle Exit, (X = 5 in)

Table A.1: Cross-Sectional Tests Camera Calibration:
Horizontal Scale Factor Data

Scale Distance	Screen Coordinates		Screen Distance		Calculated Distance	
d inch	x Pixel	y Pixel	Δx Pixel	Δy Pixel	d inch	Δy Pixel
0.00	13	405	0	0	0.000	0.000
0.25	39	406	26	1	0.244	0.479
0.50	66	407	53	2	0.498	0.976
0.75	92	408	79	3	0.742	1.455
1.00	118	408	105	3	0.986	1.933
1.25	144	408	131	3	1.231	2.412
1.50	171	409	158	4	1.484	2.909
1.75	199	409	186	4	1.747	3.425
2.00	225	409	212	4	1.991	3.903
2.25	251	410	238	5	2.236	4.382
2.50	279	410	266	5	2.499	4.898
2.75	306	410	293	5	2.752	5.395
3.00	333	410	320	5	3.006	5.892
3.25	359	411	346	6	3.250	6.371
3.50	386	411	373	6	3.504	6.868
horizontal scale line slope, m_h					0.00939	in/pixel
vertical pixel Distance slope, m_{yx}					0.01841	pixel/pixel
horizontal scale factor, k_x					0.00939	in/pixel

Table A.1 (g): Scale Positioned 6 inch away from the Nozzle Exit, (X =6 in)

Scale Distance	Screen Coordinates		Screen Distance		Calculated Distance	
d inch	x Pixel	y Pixel	Δx Pixel	Δy Pixel	d inch	Δy Pixel
0.00	57	427	0	0	0.000	0.000
0.25	86	427	29	0	0.247	-0.978
0.50	114	426	57	-1	0.485	-1.922
0.75	143	425	86	-2	0.731	-2.900
1.00	173	424	116	-3	0.987	-3.911
1.25	203	423	146	-4	1.242	-4.923
1.50	231	422	174	-5	1.480	-5.867
1.75	261	421	204	-6	1.735	-6.878
2.00	291	420	234	-7	1.990	-7.890
2.25	322	419	265	-8	2.254	-8.935
2.50	350	418	293	-9	2.492	-9.879
2.75	381	417	324	-10	2.756	-10.924
3.00	410	416	353	-11	3.002	-11.902
3.25	439	411	382	-16	3.249	-12.880
3.50	469	411	412	-16	3.504	-13.892
horizontal scale line slope, m_h					0.00900	in/pixel
vertical pixel Distance slope, m_{yx}					-0.03400	pixel/pixel
horizontal scale factor, k_x					0.00900	in/pixel

Table A.1 (h): Scale Positioned 7 inch away from the Nozzle Exit, (X =7 in)

Table A.1: Cross-Sectional Tests Camera Calibration:
Horizontal Scale Factor Data

Scale Distance	Screen Coordinates		Screen Distance		Calculated Distance	
d	x	y	Δy	Δx	d	Δx
inch	Pixel	Pixel	Pixel	Pixel	inch	Pixel
0.00	201	285	0	0	0.000	0.000
0.25	200	309	24	-1	0.264	-0.187
0.50	200	332	47	-1	0.518	-0.366
0.75	200	354	69	-1	0.760	-0.537
1.00	200	376	91	-1	1.002	-0.708
1.25	200	399	114	-1	1.255	-0.887
1.50	200	422	137	-1	1.509	-1.066
1.75	200	444	159	-1	1.751	-1.237
2.00	200	466	181	-1	1.993	-1.408
vertical scale line slope, m_v					0.01101	in/pixel
horizontal pixel distance slope, m_{xy}					-0.00778	pixel/pixel
vertictal scale factor, k_v					0.01101	in/pixel

Table A.2 (a): Scale Positioned at the Nozzle Exit, (X =0 in)

Scale Distance	Screen Coordinates		Screen Distance		Calculated Distance	
d	x	y	Δy	Δx	d	Δx
inch	Pixel	Pixel	Pixel	Pixel	inch	Pixel
0.00	156	285	0	0	0.000	0.000
0.25	156	309	24	0	0.253	0.104
0.50	156	333	48	0	0.505	0.208
0.75	156	357	72	0	0.758	0.311
1.00	156	380	95	0	1.000	0.411
1.25	156	404	119	0	1.252	0.515
1.50	157	428	143	1	1.505	0.619
1.75	157	451	166	1	1.747	0.718
2	157	475	190	1	1.99923	0.821898
vertical scale line slope, m_v					0.01052	in/pixel
horizontal pixel distance slope, m_{xy}					0.00000	pixel/pixel
vertictal scale factor, k_v					0.01052	in/pixel

Table A.2 (b): Scale Positioned 1inch away from the Nozzle Exit, (X =1 in)

Scale Distance	Screen Coordinates		Screen Distance		Calculated Distance	
d	x	y	Δy	Δx	d	Δx
inch	Pixel	Pixel	Pixel	Pixel	inch	Pixel
0.00	149	284	0	0	0.000	0.000
0.25	149	310	26	0	0.256	0.584
0.50	150	336	52	1	0.512	1.168
0.75	150	361	77	1	0.758	1.729
1.00	151	386	102	2	1.005	2.290
1.25	152	411	127	3	1.251	2.852
1.50	153	437	153	4	1.507	3.436
1.75	153	461	177	4	1.743	3.975
vertical scale line slope, m_v					0.00900	in/pixel
horizontal pixel distance slope, m_{xy}					0.02534	pixel/pixel
vertictal scale factor, k_v					0.00861	in/pixel

Table A.2 (c): Scale Positioned 2inch away from the Nozzle Exit, (X =2 in)

Table A.2 Cross-Sectional Tests Camera Calibration:
Vertical Scale Factor Data

Scale Distance d inch	Screen Coordinates x Pixel	y Pixel	Screen Distance Δy Pixel	Δx Pixel	Calculated Distance d inch	Δx Pixel
0.00	184	283	0	0	0.000	0.000
0.25	184	311	28	0	0.259	0.318
0.50	184	338	55	0	0.509	0.624
0.75	185	365	82	1	0.759	0.931
1.00	185	391	108	1	1.000	1.226
1.25	186	418	135	2	1.250	1.532
1.50	186	445	162	2	1.500	1.839
1.75	186	472	189	2	1.749	2.145
vertical scale line slope, m_v					0.00926 in/pixel	
horizontal pixel distance slope, m_{xy}					0.01135 pixel/pixel	
vertictal scale factor, k_v					0.00926 in/pixel	

Table A.2 (d): Scale Positioned 3 inch away from the Nozzle Exit, (X =3 in)

Scale Distance d inch	Screen Coordinates x Pixel	y Pixel	Screen Distance Δy Pixel	Δx Pixel	Calculated Distance d inch	Δx Pixel
0.00	180	281	0	0	0.000	0.000
0.25	181	311	30	1	0.258	0.760
0.50	182	340	59	2	0.508	1.495
0.75	182	369	88	2	0.758	2.230
1.00	183	397	116	3	0.999	2.939
1.25	184	426	145	4	1.249	3.674
1.50	184	455	174	4	1.499	4.409
vertical scale line slope, m_v					0.00900 in/pixel	
horizontal pixel distance slope, m_{xy}					0.02534 pixel/pixel	
vertictal scale factor, k_v					0.00861 in/pixel	

Table A.2 (e): Scale Positioned 4 inch away from the Nozzle Exit, (X =4 in)

Scale Distance d inch	Screen Coordinates x Pixel	y Pixel	Screen Distance Δy Pixel	Δx Pixel	Calculated Distance d inch	Δx Pixel
0.00	174	283	0	0	0.000	0.000
0.25	176	315	32	2	0.258	1.541
0.50	177	346	63	3	0.508	3.034
0.75	179	376	93	5	0.750	4.479
1.00	180	407	124	6	1.000	5.972
1.25	181	438	155	7	1.250	7.465
1.50	183	469	186	9	1.500	8.958
vertical scale line slope, m_v					0.00800 in/pixel	
horizontal pixel distance slope, m_{xy}					0.04816 pixel/pixel	
vertictal scale factor, k_v					0.00805 in/pixel	

Table A.2 (f): Scale Positioned 5 inch away from the Nozzle Exit, (X =5 in)

Table A.2 Cross-Sectional Tests Camera Calibration:
Vertical Scale Factor Data

Scale Distance d inch	Screen Coordinates x Pixel	y Pixel	Screen Distance Δy Pixel	Δx Pixel	Calculated Distance d inch	Δx Pixel
0.00	171	275	0	0	0.000	0.000
0.25	171	310	35	0	0.262	0.069
0.50	171	343	68	0	0.509	0.133
0.75	171	376	101	0	0.756	0.198
1.00	171	409	134	0	1.003	0.263
1.25	171	442	167	0	1.250	0.328
1.50	172	475	200	1	1.498	0.393
vertical scale line slope, m_v					0.00700 in/pixel	
horizontal pixel distance slope, m_{xy}					0.00196 pixel/pixel	
vertictal scale factor, k_y					0.00749 in/pixel	

Table A.2 (g): Scale Positioned 6 inch away from the Nozzle exit, (X =6 in)

Scale Distance d inch	Screen Coordinates x Pixel	y Pixel	Screen Distance Δy Pixel	Δx Pixel	Calculated Distance d inch	Δx Pixel
0.00	168	276	0	0	0.000	0.000
0.25	170	314	38	2	1.312	0.257
0.50	171	342	66	3	2.279	0.446
0.75	172	388	112	4	3.868	0.757
1.00	173	424	148	5	5.111	1.001
1.25	174	461	185	6	6.389	1.251
vertical scale line slope, m_v					0.007 in/pixel	
horizontal pixel distance slope, m_{xy}					0.035 pixel/pixel	
vertictal scale factor, k_y					0.00675 in/pixel	

Table A.2 (h): Scale Positioned 7 inch away from the Nozzle Exit, (X =7in)

Table A.2 Cross-Sectional Tests Camera Calibration:
Vertical Scale Factor Data

Scale Distance	Screen Coordinates		Screen Distance		Calculated Distance	
d	x	y	Δx	Δy	d	Δy
inch	Pixel	Pixel	Pixel	Pixel	inch	Pixel
0.00	416	227	0	0	0.000	0.000
0.50	385	225	-31	-2	0.494	-1.173
1.00	354	224	-62	-3	0.988	-2.347
1.50	322	222	-94	-5	1.498	-3.558
2.00	291	221	-125	-6	1.993	-4.731
2.50	259	220	-157	-7	2.503	-5.942
3.00	227	219	-189	-8	3.013	-7.153
3.50	195	218	-221	-9	3.523	-8.364
4.00	164	217	-252	-10	4.017	-9.537
4.50	133	216	-283	-11	4.511	-10.711
5.00	101	215	-315	-12	5.022	-11.922
5.50	70	214	-346	-13	5.516	-13.095
6.00	40	214	-376	-13	5.994	-14.230
6.50	10	213	-406	-13	6.472	-15.366
horizontal scale line slope, m_h					0.01593 in/pixel	
vertical pixel Distance slope, m_{yx}					0.03785 pixel/pixel	
horizontal scale factor, k_x					0.01594 in/picel	

Table A.3 (a): Scale Positioned at the Nozzle Axis (single point calibration)

Scale Distance	Screen Coordinates		Screen Distance		Calculated Distance	
d	x	y	Δx	Δy	d	Δy
inch	Pixel	Pixel	Pixel	Pixel	inch	Pixel
0.00	413	178	0	0	0.000	0.000
0.50	386	178	-27	0	0.521	-0.144
1.00	359	178	-54	0	1.043	-0.287
1.50	333	177	-80	-1	1.545	-0.426
2.00	306	177	-107	-1	2.067	-0.569
2.50	280	177	-133	-1	2.569	-0.708
3.00	253	176	-160	-2	3.090	-0.852
3.50	227	176	-186	-2	3.592	-0.990
4.00	200	176	-213	-2	4.114	-1.134
4.50	173	176	-240	-2	4.635	-1.277
5.00	147	176	-266	-2	5.137	-1.416
5.50	121	176	-292	-2	5.640	-1.554
6.00	95	176	-318	-2	6.142	-1.692
6.50	69	176	-344	-2	6.644	-1.831
7.00	44	177	-369	-1	7.127	-1.964
7.50	19	177	-394	-1	7.610	-2.097
horizontal scale line slope, m_h					0.01893 in/pixel	
vertical pixel Distance slope, m_{yx}					0.00589 pixel/pixel	
horizontal scale factor, k_x					0.01893 in/pixel	

Table A.3(b) : Scale is at the Nozzle Eenter Line

Table A.3: Axial Tests Camera Calibration:
Horizontal Scale Factor Data

Scale Distance	Screen Coordinates		Screen Distance		Calculated Distance	
d	x	y	Δx	Δy	d	Δy
inch	Pixel	Pixel	Pixel	Pixel	inch	Pixel
0.00	408	178	0	0	0.000	0.000
0.50	382	177	-26	-1	0.489	-0.184
1.00	355	177	-53	-1	0.996	-0.376
1.50	328	177	-80	-1	1.504	-0.567
2.00	302	176	-106	-2	1.993	-0.752
2.50	275	176	-133	-2	2.500	-0.943
3.00	248	176	-160	-2	3.008	-1.134
3.50	221	176	-187	-2	3.516	-1.326
4.00	194	176	-214	-2	4.023	-1.517
4.50	167	176	-241	-2	4.531	-1.709
5.00	141	176	-267	-2	5.020	-1.893
5.50	114	176	-294	-2	5.527	-2.085
6.00	88	176	-320	-2	6.016	-2.269
6.50	62	176	-346	-2	6.505	-2.453
7.00	36	176	-372	-2	6.994	-2.638
7.50	11	176	-397	-2	7.464	-2.815
horizontal scale line slope, m_h					0.01880 in/pixel	
vertical pixel Distance slope, m_{yx}					0.00709 pixel/pixel	
horizontal scale factor, k_x					0.01880 in/pixel	

Table A.3(c) : Scale is 0.25 in front of the Nozzle Center Line

Scale Distance	Screen Coordinates		Screen Distance		Calculated Distance	
d	x	y	Δx	Δy	d	Δy
inch	Pixel	Pixel	Pixel	Pixel	inch	Pixel
0.00	413	178	0	0	0.000	0.000
0.50	385	178	-28	0	0.529	-0.158
1.00	359	178	-54	0	1.020	-0.305
1.50	333	177	-80	-1	1.511	-0.452
2.00	306	177	-107	-1	2.020	-0.604
2.50	279	176	-134	-2	2.530	-0.757
3.00	253	176	-160	-2	3.021	-0.904
3.50	227	176	-186	-2	3.512	-1.051
4.00	200	176	-213	-2	4.022	-1.203
4.50	173	176	-240	-2	4.532	-1.356
5.00	147	176	-266	-2	5.023	-1.503
5.50	121	176	-292	-2	5.514	-1.649
6.00	95	176	-318	-2	6.004	-1.796
6.50	69	177	-344	-1	6.495	-1.943
7.00	44	177	-369	-1	6.967	-2.084
7.50	19	177	-394	-1	7.440	-2.226
horizontal scale line slope, m_h					0.01888 in/pixel	
vertical pixel Distance slope, m_{yx}					0.00565 pixel/pixel	
horizontal scale factor, k_x					0.01888 in/pixel	

Table A.3(d) : Scale is 0.25 behind of the Nozzle Center Line

Table A. Axial Tests Camera Calibration:
Horizontal Scale Factor Data

Scale Distance	Screen Coordinates		Screen Distance		Calculated Distance	
d	x	y	Δy	Δx	d	Δx
inch	Pixel	Pixel	Pixel	Pixel	inch	Pixel
0.00	229	133	0	0	0.000	0.000
0.50	228	180	47	-1	0.564	-1.092
0.75	228	199	66	-1	0.792	-1.533
1.00	227	219	86	-2	1.032	-1.998
1.25	226	239	106	-3	1.272	-2.463
1.50	226	258	125	-3	1.500	-2.904
1.75	226	278	145	-3	1.740	-3.369
2.00	225	299	166	-4	1.992	-3.856
vertical scale line slope, m_v					0.01200 in/pixel	
horizontal pixel distance slope, m_{xy}					-0.02323 pixel/pixel	
vertictal scale factor, k_y					0.01200 in/pixel	

Table A.4(a) : Scale is at the Nozzle Center Line (Single Poing Calibration)

Scale Distance	Screen Coordinates		Screen Distance		Calculated Distance	
d	x	y	Δy	Δx	d	Δx
inch	Pixel	Pixel	Pixel	Pixel	inch	Pixel
0.00	355	143	0	0	0.000	0.000
0.50	355	177	34	0	0.509	-0.363
1.00	354	210	67	-1	1.004	-0.715
1.50	354	243	100	-1	1.498	-1.067
vertical scale line slope, m_v					0.01498 in/pixel	
horizontal pixel distance slope, m_{xy}					0.01067 pixel/pixel	
vertictal scale factor, k_y					0.01498 in/pixel	

Table A.4(b) : Scale is 0.25 in Front of the Nozzle Center Line

Table A.4: Axial Tests Camera Caliberation: Vertical Scale Factor Data

Scale Distance	Screen Coordinates		Screen Distance		Calculated Distance	
d	x	y	Δy	Δx	d	Δx
inch	Pixel	Pixel	Pixel	Pixel	inch	Pixel
0.50	359	145	42	0	0.593	-0.170
0.75	359	161	58	0	0.819	-0.235
1.00	359	177	74	0	1.045	-0.300
1.25	359	193	90	0	1.270	-0.365
1.50	359	210	107	0	1.510	-0.434
1.75	358	227	124	-1	1.750	-0.503
2.00	358	243	140	-1	1.976	-0.567
vertical scale line slope, m_v					0.01412 in/pixel	
horizontal pixel distance slope, m_{xy}					0.01067 pixel/pixel	
vertictal scale factor, k_y					0.01412 in/pixel	

Table A.4(c) : Scale is at the Nozzle Center Line

Scale Distance	Screen Coordinates		Screen Distance		Calculated Distance	
d	x	y	Δy	Δx	d	Δx
inch	Pixel	Pixel	Pixel	Pixel	inch	Pixel
0.00	360	145	0	0	0.000	0.000
0.50	360	177	32	0	0.490	-0.351
1.00	359	210	65	-1	0.996	-0.713
1.50	359	243	98	-1	1.502	-1.075
vertical scale line slope, m_v					0.01532 in/pixel	
horizontal pixel distance slope, m_{xy}					0.01097 pixel/pixel	
vertictal scale factor, k_y					0.01532 in/pixel	

Table A.4(d) : Scale is 0.25 in Behind the Nozzle Center Line

Table A.4: Axial Tests Camera Calibration: Vertical Scale Factor Data

APPENDIX B

Theoretical Verification of the Calibration Scale Factors

An optical ray tracing method, along with the paraxial approximation, was utilized to verify the camera calibration results. To further simplify the ray tracing analysis, the wall of the tank was treated as water. This approximation was justified because the thickness of the glass was very small compared to the water/glass and glass/camera spacing; also, the glass index of refraction (1.5) was close to that of water (1.33). Hence, the optical path length does not change significantly by the above approximation. Refer to figure B.1 for illustrating the derivation of the scale factors.

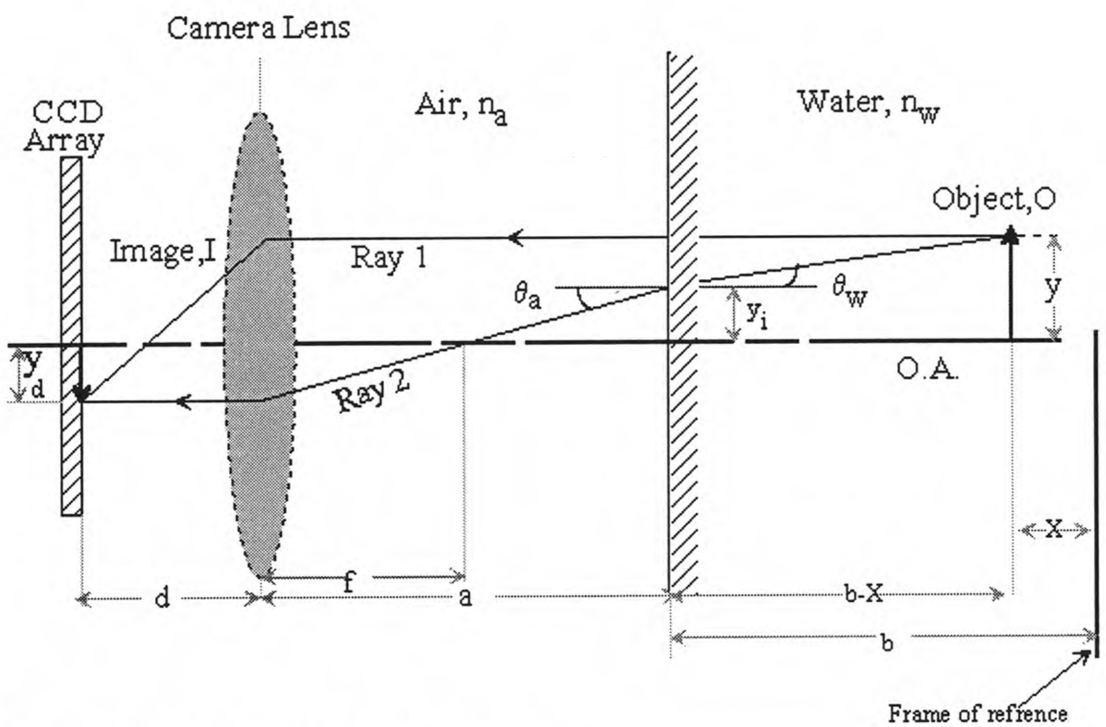

Figure B.1: Schematic of Optical System

As a ray coming from a point inside the water tank crosses the interface, it deflects in accordance with Snell's law which is defined as:

$$n_w \sin(\theta_w) = n_a \sin(\theta_a) \quad \text{(B.1)}$$

where n_w and n_a are the indices of refraction of water and air respectively, and θ_w and θ_a are the angles that a ray incident on the interface makes with the normal to the interface on the water side and the air side, respectively. A ray normal to the interface does not undergo any deflection as it crosses the boundary and it is focused at the back focal point of the camera. Another ray approaching the interface at an angle θ_w refracts at the interface, leaving the boundary at an angle θ_a. If the second ray crosses the front focal point of the camera's lens, it comes out parallel to the optical axis as it leaves the lens. The intersection of the two rays defines the location of a point on the image plane. Mapping the rest of the points on the object surface defines the image. The resulting image is usually real, inverted and smaller than the object. The size of the resulting image, which was defined on Figure B.1 as y_d, can be determined from geometrical considerations. Using Snell's law, along with small angle approximation, the angle θ_a is found as:

$$\theta_a = \frac{n_w}{n_a}\theta_w \quad \text{(B.2)}$$

Also, the angle θ_w can be expressed in terms of the object length y, the distance above the optical axis at which ray 2 intersects with the interface y_i, and the distance of the object from the interface z as:

$$\theta_w = \tan^{-1}\left(\frac{y - y_i}{z}\right) \approx \frac{y - y_i}{z} \quad \text{(B.3)}$$

Substituting for θ_w from Equation(b.3) into Equation (b.2) for θ_a yields the following expression for θ_a

$$\theta_a = \frac{n_w}{n_a}(\frac{y-y_i}{z}) \qquad (B.4)$$

Also, the angle θ_a is found, in terms of the object length y and the distance at which ray 2 hits the interface above the optical axis y_i, according to the following expression:

$$\theta_a = \tan^{-1}(\frac{y_i}{a-f}) \approx \frac{y_i}{a-f} \qquad (B.5)$$

Combining Equations (B.4) and (B.5) to fine an expression for y_i, and substituting this expression into Equation (B.3) yields

$$\theta_w = \frac{y - \dfrac{y}{1+(\dfrac{n_a}{n_w})(\dfrac{z}{a-f})}}{z} \qquad (B.6)$$

Using the small angle approximation once again, the image length y_d is found in terms of the angle θ_a and the focal length f as:

$$y_d = f\theta_a \qquad (B.7)$$

Substituting in the above equation the expression for θ_a given in Equation (B.4), yields :

$$y_d = f(\frac{n_w}{n_a})\theta_w \qquad (B.8)$$

Substituting for the angle θ_w, the above expression for y_d becomes

$$y_d = f(\frac{n_w}{n_a})\frac{y - \dfrac{y}{1+(\dfrac{n_a}{n_w})(\dfrac{z}{a-f})}}{z} \qquad (B.9)$$

Simplifying the above equation gives:

$$y_d = \frac{\left(\frac{f}{a-f}\right)y}{1+\left(\frac{n_a}{n_w}\right)\left(\frac{z}{a-f}\right)} \qquad \text{(B.10)}$$

The CCD array to some extent simulates the task of the retina in human eye. It maps the image to 512x480 pixels. The signal from the CCD array was inverted so the final image on the screen was upright. Since the size of the pixel on the monitor screen was larger than the size of the pixel on the CCD array, the image on the screen was magnified. To figure out the number of pixels that will be seen on the screen, the image length must be multiplied by the sensitivity factor of the CCD array, K. Hence the length of the image on the monitor screen becomes:

$$y'_d = K\frac{\left(\frac{f}{a-f}\right)y}{1+\left(\frac{n_a}{n_w}\right)\left(\frac{z}{a-f}\right)} \qquad \text{(B.11)}$$

Now, defining the scale factor (k) to be the ratio between the object length (y) and the image length from the screen (y'_d), yields

$$k=\frac{1}{Kf}\left(a-f+\frac{n_a}{n_w}z\right) \qquad \text{(B.12)}$$

The sensitive factor K for the horizontal image dimension is 2029 pixel/inch and the sensitivity factor for the vertical image dimension is 2493 pixel/inch. Figure A.2 shows the agreement between the experimental evaluation of the vertical scale factor and the theoretical scale factor for the cross-sectional calibration. Comparison between the measured and theoretically predicted values of the scale factors are presented in Table B.1.

Distance along optical axis X (in)	Measured scale factor Horizontal kx,m	Vertical ky,m	Theoretical scale factor Horizontal kx,t	Vertical ky,t
0.00	0.013801	0.011011	0.014374	0.011697
1.00	0.013077	0.010522	0.013592	0.011060
2.00	0.012210	0.009846	0.012809	0.010423
3.00	0.011597	0.009256	0.012027	0.009786
4.00	0.010786	0.008612	0.011244	0.009150
5.00	0.010070	0.008049	0.010462	0.008513
6.00	0.009392	0.007488	0.009679	0.007876
7.00	0.008502	0.006754	0.008897	0.007240

Table B.1: Comparison of Measured and Theoretical Scale Factors for the Cross Sectional Calibration

APPENDIX C

Uncertainty Analysis

Estimating the uncertainty of the camera image position measurements involved determining the uncertainty for each of the following measured quantities:

1. Position measurement
2. Image scale factor, k
3. Distance measurements

C.1 Position Measurement Uncertainty

It was necessary to make several position measurements, such as measuring the location of the nozzle, the boundary of the Plexiglas plates representing the ceiling and the back wall of the test chamber, and the outline of the jet. Uncertainty in measuring the location of a point on the image was associated with the camera and the image viewing software. The non-linearity, hysteresis and drift of the camera were accounted for by calibrating the camera. Hence, the camera resolution was the only major source of uncertainty in the position measurement. The resolution of the camera was 1 pixel; therefore, the resolution uncertainty in the camera position measurement was $\pm\frac{1}{2}$ pixel in both the vertical and horizontal directions. However, the uncertainty in choosing the location of a certain point on the image, using an image editing software, was limited to ± 1 pixel in the vertical and horizontal directions. Furthermore, noise and stray reflections in the images of the jet made determining the location of the jet boundary and attachment point uncertain to within about 2 pixels.

C.1 The Scale Factor Uncertainty

Each image had both horizontal and vertical scale factors (k_x and k_y) that were calculated from the following two equations:

$$k_x^2 = (\frac{d_x}{\Delta x})^2 - (k_y \frac{\Delta y}{\Delta x})^2 \quad (C.1)$$

$$k_y^2 = (\frac{d_y}{\Delta y})^2 - (k_x \frac{\Delta x}{\Delta y})^2 \quad (C.2)$$

where d_x and d_y were known horizontal and vertical increments on the scale used for calibration (measured in inches). Δx and Δy were the corresponding increments estimated from the image of the scale(measured in pixels). The second terms on the right hand sides of Equations (C.1) and (C.2) account for any rotation of the scale during calibration. The rotation terms in Equations (C.1) and (C.2) were very small in comparison with the other terms. For example, the magnitude of the rotation term was about 0.005% in the case of the horizontal scale factor (k_x). In fact, the rotation term had no effect on estimating the horizontal factor as was presented in Table A.1 and A.3. For the vertical scale factor (k_y), the magnitude of the rotation term was about 0.05. The rotation term for the vertical scale factor was larger than the rotation term associated with the horizontal scale factor because the horizontal scale factor calibration had more data points than the vertical scale factor calibration. Since the rotation term was much less than the main term, any contribution of the rotation terms to the uncertainty in the scale factor was insignificant. Hence; for estimating the uncertainty in the scale factor, the rotation term will be in Equations (C.1) and (C.2) will be ignored. After simplification, the expressions for the horizontal and vertical scale factors becomes similar. Therefore, the subscripts were dropped from the scale factor symbol (k). The simplified scale factor expression becomes:

$$k \approx \frac{d}{\Delta x} \qquad \text{(C. 3)}$$

where d was the image dimension measured in inches, Δx was the image dimension measured in pixels. The rms. absolute uncertainty estimate in measuring the scale factor (E_k) becomes:

$$E_k = \sqrt{(\frac{1}{\Delta x}E_d)^2 + (-\frac{d}{\Delta x^2}E_r)^2} \qquad \text{(C.4)}$$

where E_d is the uncertainty in measuring the distance between two (0.25 in or 0.5 in) marks on the image of the scale used during calibration. Uncertainty in measuring the distance d (E_d) is composed of the uncertainty of the scale used during calibration (E_m), the resolution uncertainty in choosing the position of the scale marks(E_r), and the scattering uncertainty in the image dimension (E_s). The scatter uncertainty in estimating the image dimension in inches (E_s) was a measure of the difference between the measured image dimensions in inches (d) and the best fit line for the image dimension in inches (d) through the image dimension in pixels (Δx). The rms. estimate of the uncertainty in the image dimension measurement becomes :

$$E_d = \sqrt{E_m^2 + (\frac{d}{\Delta x}E_r)^2 + E_s} \qquad \text{(C.5)}$$

Uncertainty in measuring the image dimension in inches (E_m) was $\pm\frac{\sqrt{2}}{32}$ in. The maximum scattering uncertainty was established to be ±0.021 inch. Substituting Equation (C.5) into Equation (C.4) yields for the scale factor uncertainty

$$E_k = \sqrt{\frac{E_m^2 + E_s^2}{\Delta x^2} + 2\cdot(\frac{d}{\Delta x^2}E_r)^2} \qquad \text{(C.6)}$$

Also, the images will have uncertainty associated with positioning the camera with respect to the object being imaged. From calibration, the best linear fit for the scale factor (k inch/pixel) measurements versus the distance measured along the optical axis away from the plane of the jet discharge (X inch) was found as :

$$k(X) = a + bX \qquad \text{(C.7)}$$

where a and b were linear fit constants. Using the above equation to determine the scale factor from the position X adds two terms to the scale factor uncertainty. One term is associated with the uncertainty in measuring distance X with respect to a frame of reference. This uncertainty, E_x, was established to be within ($\pm\frac{1}{8}$ in). The second term, that adds to the scale factor uncertainty, comes from the scattering of the scale factor measurements from the linear fit to the scale factor data versus the distance of the object from a frame of reference. This additional uncertainty is denoted by E_{sk}. For the cross-sectional calibration, the frame of reference was at the nozzle exit. For the axial calibration the frame of reference coincided with the nozzle axis. The scale factor uncertainty thus becomes:

$$E_k = \sqrt{\left(\frac{E_m^2 + E_s^2}{\Delta x}\right)^2 + 2\cdot\left(\frac{d}{\Delta x^2} E_r\right)^2 + (b\,E_X)^2 + E_{sk}^2} \qquad \text{(C.8)}$$

For the cross-sectional calibration , an eight point calibration was performed. Values for the constant b and scattering uncertainty E_{sk} were determined for both horizontal and vertical scale factors. For the horizontal scale factor k_x, the constant b was 0.000746 in^2/pixel, and the vertical scale factor constant b was 0.000605 in^2/pixel. The scattering error E_{sk} was ±0.00008 inch/pixel for both horizontal and vertical scale factors. The longitudinal calibrations did not have as many data points. One of the longitudinal calibrations had three points from which the constant b was estimated to be 0.0032 in^2/pixel for the horizontal scale factor and 0.0024 in^2/pixel for the vertical scale factor. The other calibration was made at a single point. The value for the scattering uncertainty in the scale factor was approximated as the scattering uncertainty from the cross sectional calibration. The scale factor relative uncertainty, defined by the absolute scale factor uncertainty divided by the scale factor magnitude, becomes:

$$e_k = \frac{E_k}{k} \qquad \text{(C.9)}$$

Tables C.1 and C.2 contain the scale factor uncertainties from the cross sectional calibration. Table C.3 and C.4 contain the uncertainties in the horizontal and vertical scale factors from the longitudinal calibration.

C.2 Distance Measurement

Distance measurements were made to determine the length of the attachment distance, the location of the jet with respect to the apparatus, and the growth of the jet. The distance was calculated from the image scale factor and the dimension in pixels according to the following expression

$$L = k\Delta x \tag{C.10}$$

where k is the scale factor and Δx is the image dimension in pixels. The distance measurements uncertainty becomes:

$$E_L = \pm\sqrt{(E_k\Delta x)^2 + (kE_{\Delta x})^2} \tag{C11}$$

where $E_{\Delta x}$ is the resolution uncertainty associated with determining the position of the beginning and ending point. The rms. estimate of the resolution uncertainty becomes $\pm\sqrt{2}$ pixels. E_k is the scale factor uncertainty. Hence, the uncertainty in distance measurements, E_L, becomes:

$$E_L = \pm\sqrt{(\Delta x_L E_k)^2 + 2\ k^2} \tag{C.12}$$

The relative distance measurement uncertainty defined by the absolute uncertainty divided by the measured distance is given by:

$$e_L = \frac{E_L}{L} \tag{C.13}$$

The magnitudes of the rms. uncertainty estimates associated with the length of the attachment distance measurements made using the axial isothermal laminar jet images are given in Table C.5. The absolute uncertainty in measuring the point of reattachment from the axial jet images was within ± 0.30 in, and the corresponding relative uncertainty was ±4%.

Axial Distance X (in)	Horizontal Scale Factor k_x (in/pixel)	Scatering Uncertaitny E_s (in)	Scale Length d_x (in)	Image Length Δx (pixel)	Absolute Uncertainty E_{kx}	Relative Uncertainty e_{kx}
0	0.0138	0.02	4.0	290	0.00023	2%
1	0.0131	0.02	3.5	268	0.00024	2%
2	0.0122	0.01	3.0	246	0.00024	2%
3	0.0116	0.02	3.5	302	0.00022	2%
4	0.0108	0.02	3.5	325	0.00020	2%
5	0.0101	0.01	3.5	348	0.00019	2%
6	0.0094	0.02	3.5	373	0.00019	2%
7	0.0085	0.00	3.5	469	0.00016	2%

Table C.1
Uncertainty Analysis of the Horizontal Scale Factor from- Cross Sectional Data

Axial Distance X (in)	Vertical Scale Factor k_y (in/pixel)	Scatering Uncertaitny E_s (in)	Scale Length d_y (in)	Image Length Δy (pixel)	Absolute Uncertainty E_{ky}	Relative Uncertainty e_{ky}
0	0.0110	0.02	2.00	181	0.00031	3%
1	0.0105	0.01	2.00	190	0.00028	3%
2	0.0098	0.01	1.75	177	0.00030	3%
3	0.0093	0.01	1.75	189	0.00028	3%
4	0.0086	0.01	1.50	174	0.00030	3%
5	0.0081	0.01	1.50	186	0.00028	3%
6	0.0075	0.01	1.50	200	0.00026	4%
7	0.0068	0.05	1.25	185	0.00040	6%

Table C.2
Uncertainty Analysis of the Vertical Scale Factor from Cross-Sectional Data

Axial Distance X (in)	Horizontal Scale Factor k_x (in/pixel)	Scale Length d_x (in)	Image Length Δx (in)	Absolute Uncertainty E_{kx} (in/pixel)	Relative Uncertainty e_{kx}
single point	0.01593	6.50	406	0.00043	3%
0.25	0.01880	7.50	394	0.00052	3%
-0.25	0.01888	7.50	397	0.00051	3%
0.00	0.01893	7.50	394	0.00051	3%

Table C.3
Uncertainty Analysis of the Horizontal Scale Factor from Longtidunal Calibration

Axial Distance X (in)	Vertical Scale Factor k_y (in/pixel)	Scale Length d_y (in)	Image Length Δy (in)	Absolute Uncertainty E_{ky} (in/pixel)	Relative Uncertainty e_{ky}
single point	0.0120	2.00	166	0.00058	5%
0.25	0.0149	1.50	98	0.00063	4%
-0.13	0.0153	1.50	100	0.00063	4%
0.00	0.0141	2.00	140	0.00082	6%

Table C.4
Uncertainty Analysis of the Vertical Scale Factor from Longtidunal Calibration

Horizontal Scale Factor k_x (in/pixel)	Attachment Length L (in)	Image length of attachment Δx (pixel)	Absolute Uncertainty E_L (in)	Relative Uncertainty e_L
0.01590	2.9892	188	0.12	4%
0.01590	4.1658	262	0.16	4%
0.01893	4.3160	228	0.20	5%
0.01893	6.0197	318	0.27	4%
0.01893	6.7769	358	0.30	4%

Table C.5
Estimating the Uncertainty in the Attachment Distance
Measured from Longtidunal Isothermal Data

APPENDIX D

Theoretical Prediction of the Jet Attachment Length

D.1 Isothermal Jet

For theoretical approximation, the jet expansion and center line velocity decay are approximated to be similar to those of an un-deflected jet inspite of the jet curving toward the wall. This is not exactly true; however, it is a reasonable first approximation. Figure D.1 shows a comparison between a curved jet and an un-deflected jet. The velocity profile for the un-deflected turbulent free jet is given by:

$$\frac{u}{U_{\max}} = \sec h^2 \eta \qquad \text{(D.1)}$$

Where η and U_{max} (the center line velocity) are defined in the following two equations:

$$\eta = \frac{\sigma Y}{X} \qquad \text{(D.2)}$$

$$U_{\max} = \sqrt{\left(\frac{3\sigma J_0}{4\rho X}\right)} \qquad \text{(D.3)}$$

where σ is an empirical constant which is a measure of the jet entrainment. See Sawyer (1960) for more details about the definition of this constant and the simple theory presented here. For the curved jet Y and X are measured along the jet, center line and normal to it. This complies with the un-deflected jet coordinates. ρ is the fluid density and J_0 is the jet momentum at the nozzle outlet. The jet mass flow rate (m) and momentum (J_0) are evaluated from the given velocity profile as

$$m = 2U_{max}\frac{X}{\sigma} \tag{D.4}$$

$$J = \frac{4}{3}U^2{}_{max}\frac{X}{\sigma} \tag{D.5}$$

The location of the jet outer boundary is defined as the locus of points where the local axial velocity of the jet drops to one tenth of the local center line velocity U_{max}. Using this definition for the curved jet, the width of the jet (δ) at the point where the jet outer boundary would first strike the plate, in the absence of the wall effect, can be found from the following equation:

$$0.1 = \sec h^2\left(\frac{\sigma\,\delta}{X_1}\right) \tag{D.6}$$

From which follow, the jet 1/2 width is found as:

$$\frac{\delta}{2} = \frac{X_1}{\sigma}a\tanh\sqrt{0.9} = \frac{1.825}{\sigma}X_1 \tag{D.7}$$

From Figure D.1, the jet attachment length is related to the nozzle-to-plate height (h), the nozzle diameter (D), the jet radius of curvature (R), and the angle of the jet impingement (θ) by the following geometrical relations:

$$X_1 - X_0 = R\theta \tag{D.8}$$

$$h = R(1-\cos\theta) + \delta_1\cos\theta \tag{D.9}$$

$$L = R\sin\theta \tag{D.10}$$

where (X_0) corresponds to the location along the jet center line corresponding to the nozzle locations, (X_1) corresponds to the distance along the jet center-line to the point where the jet would hit the plate, and (L) is the jet attachment length. The jet radius of curvature is related to the jet momentum and the net pressure difference acting on the jet (Δp) by the following equation:

$$\Delta p = \frac{J}{R} \qquad \text{(D.11)}$$

X_0 is related to the velocity of the jet at the nozzle outlet. Assuming uniform velocity U at the exit yields

$$\rho U t = 2\rho U \frac{X_0}{\sigma} \Rightarrow X_0 = \frac{t}{2\sigma} \qquad \text{(D.12)}$$

X_1 is evaluated by considering a mass conservation for the top half of the jet. The mass flow rate of the fluid between the jet center line and the reattaching stream line must be equal to half of the mass flow rate at the nozzle outlet. The conservation of the mass flow rate in the jet top half is then expressed by the following equation:

$$\frac{1}{2}\dot{m} = \int_0^{Y_R} \rho u dY \qquad \text{(D.13)}$$

The mass flow rate at the nozzle exit is related to the jet momentum by the following relation:

$$\frac{1}{2}\dot{m} = \frac{1}{2}\sqrt{J_0 D \rho} \qquad \text{(D.14)}$$

Substituting for the velocity profile in Equation (D.13), then equating Equation (D.13) with Equation (D.14), yields

$$\frac{1}{2}\sqrt{J_0 D \rho} = \sqrt{\frac{3\rho J_0 X}{4\sigma}} T \qquad \text{(D.15)}$$

where T is defined as:

$$T = \tanh\left(\frac{\sigma\, Y_R}{X}\right) \tag{D.16}$$

and where Y_R corresponds to the reattaching streamline. Solving Equation (D.16) for X_1, yields

$$X_1 = \frac{\sigma_t}{3T_1^2} \tag{D.17}$$

Substituting for the values of X_1 and X_0 into Equations (D.9) and (D.10) yields

$$\frac{h}{t} = \frac{\sigma}{3\theta}\frac{1-T_1^2}{T_1^2}\left(1-\cos\theta + \frac{1.825}{\sigma}\left(\frac{\theta\cos\theta}{1-T_1^2}\right)\right) \tag{D.18}$$

$$\frac{L}{h} = \frac{\sin\theta}{1-\cos\theta + \dfrac{1.825}{\sigma}\dfrac{1}{1-T_1^2}} \tag{D.19}$$

To solve the above equations, a relationship between θ and T_1 is found from applying a momentum balance at the attachment point as follows:

$$J_1\cos\theta = J_2 - J_3 \tag{D.20}$$

where J_1, J_2, and J_3 are Defined below as:

$$J_1 = 2\int_0^\infty(\rho\, u)u\,dY = \frac{4}{3}\rho U^2{}_{max}\frac{X}{\sigma} \tag{D.21}$$

$$J_2 = \int_{-\infty}^{0}(\rho\, u)u\,dY + \int_0^{Y_R}(\rho\, u)u\,dY \tag{D.22}$$

$$J_3 = \int_{Y_R}^{\infty}(\rho\, u)u\,dY \tag{D.23}$$

Combining (D.21), (D.22), and (D.23) into (D.20), yields:

$$\cos\theta = \frac{3}{2}T_1 - \frac{1}{2}T_1^3 \tag{D.24}$$

Equation (D.24) is combined with Equation (D.18) to solve for T_1. Once T_1 is known, then the attachment length is evaluated using Equation (D.19).

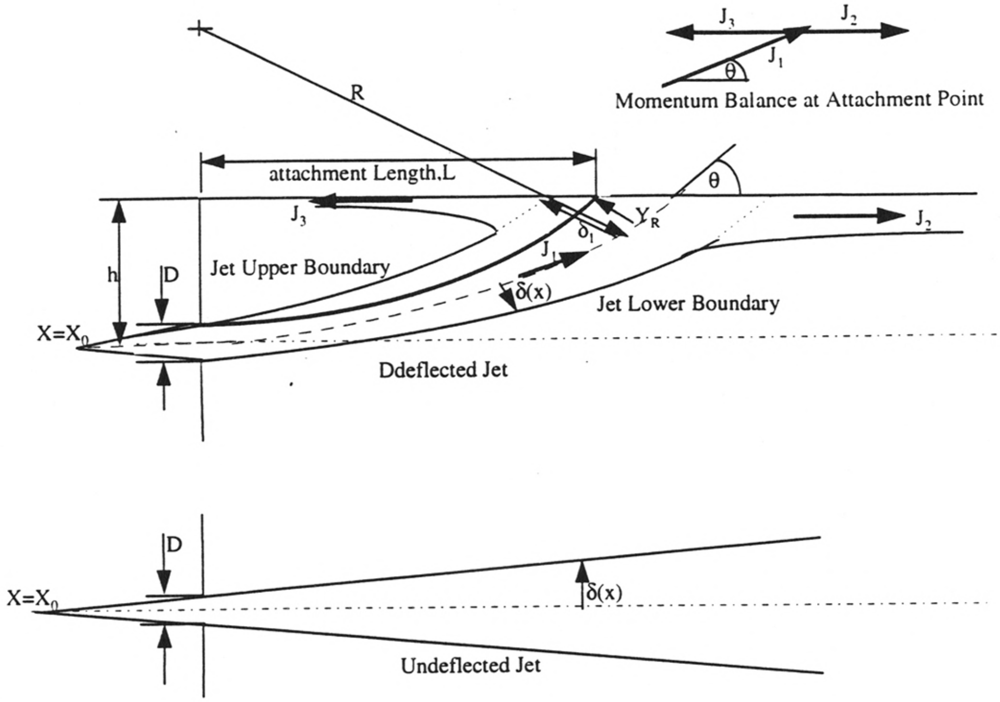

Figure D.1: Relating Curved Jet to Un-deflected Jet

APPENDIX E

CCD CAMERA SPECIFICATION

Imager	1/2 in interline transfer CCD
• Pixels	768 (H) x 494 (V)
• Cell Size	8.4 (H) x 9.8 (V) microns
• Sensing Area	6.41 (H) x 4.89 (V) mm
• Dynamic Range	67db
	Low noise, blooming suppression
• Chip Size	7.95 mm (H) x 6.45 mm (V)
Scanning	525 lines, 2:1 interlace
• Clock:	28.6363 MHz
• Pixel Click:	14.31818 MHz
• Horizontal Frequency	15.734 KHz
• Vertical Frequency	59.92 Hz
Other	
• Sync	Int./Ext.
• TV Resolution	570 (H) x 485 (V) lines
• Video Output	1.0 V p-p composite video, 75
• S/N Ratio	50db min.
• Minimum Illumination	1.0 lux(F=1.4) without IR cut filter
• AGC	ON (16db standard, 32db max.)/Off
• Gamma	0.45 or 1

• Lens Mount	C-mount
• Power Requirement	DC 12 V (9V min.) 2.5 W
• Operating Temperature	-10 C to + 50 C
• Storage Temperature	-30 C to +60 C
• Operating Humidity	within 70%
• Storage Humidity	within 90%
• Vibration	7G(1 Hz to 2 Hz)
• Shock	70G
Dimensions	45mm (W) x 39mm (H) x 80 mm (L)

APPENDIX F

Dt 2861 FRAME GRABBER SPECIFICATIONS

Standard monochrome video input

• Input Signal:	DT2861-60Hz,RS-170,RS-330 NTSC; ac-coupled,dc restoration (or) DT2861-50Hz,CCIR,PAL; ac-coupled, dc restoration Interlaced; a jumper-selectable chrominance notch filter is available to eliminate color information from NTSC and PAL signals
• A/B:	8-bit at 1-Mhz with dc restoration
• Frame Grab Speed:	1/30 s
• Sync Signal:	Composite from external input; or internal with sync output (for inuts without composite sync)
• Reselution:	480 Lines x 512 Lines (Dt2861-60Hz)

Arithmetic logic unit (alu) and lookup tables (luts)

• ALU Size:	8-bit operands; 8-bit plus carry result
• ALU Speed:	100 ns per pixel (one 512 x 512 x 8 bit image frame in 1/30 s)
Function:	Logic AND, OR, XOR; addition and

	subtraction; identity (passthrough)
Input LUTs:	Eight, 256 x 8-bit each
Result Input LUTs:	Four, 512 x 8-bit each

Slow-scan and non-standard video and control inputs

• Scan Triger Input :	Falling edge initate digitaizition of a complete frame; presents one LSTTL load
• Pixel Clock Input:	0 to 12 million pixels per second
• Clock Enable Input:	When low, indicates active pixel presence; presents one LSTTL load
• Pixel Rate:	0 to 12 million pixels per second
• Video Input Signal:	Jumper-selectavle ac or dc coupoing, dc rstoration Jumper-selectable 75ohm temination
•Videow Input Ranges:	0.340 to 1.000, Jumper-selectalble 0.000 to 0.66- - 1.320V, resistor-selectavle
• Format:	Non-interlace

Frame-store memory

• Frame-store Memory:	Sixteen (4 Mbytes total), 512x512x8-bit each (256 Kbyte each); memory-mapped
• Access:	Transpernt form bus; read or write any time

Power requiremts

• +5V:	+/-10%,@2.5 A typical
• +12V:	+/-10%.@0.08A typical
• -12V:	+/-10%, @0.08A typical

Connectors

• Video Input/OUtput (j1):	16-pin AMP connector (matching connector Am 226733-5)
• Slow-Scan Control (j2):	10-pin 3M-type connector (mating connector 3M 3473-7010)
• External I/O ports (j3,j4):	(2) 16-pin 3M-type connectors (mating connector 3M 3452-7016)

APPENDIX G

Laser Specs

Manufacturer: Spectra-Physics

Models Number: 124 B Helium-Neon Laser

Serial Number: 3575/1377

output

Wavelength: 632.8 nm

Power TEM_{00}: 15 mW

Beam Characteristics

Beam Diameter (@1/e$^{2)}$: 1.1 mm

Beam Divergence: 0.75 mrad

Optics

output mirror: G3817-005

High Reflector: G3801-012

Installation & Test: Not Available

Resonator Characteristics

Transverse Mode: TEM_{00}

Degree of Polarization: 1×10^{-3}

Angle of Polarization: Vertical $\pm 5°$

Resonator Configuration: Long Radius

Resonator Length: 70.1 cm

Axial Mode Spacing: 2.4 MHz

Plasma Excitation: Direct current, self-starting

Amplitude Stability

Beam amplitude noise (1-100 Hz): <0.3% rms.

Beam amplitude ripple (1-120 Hz): <0.2%

Long term power drift: <5% over 10°C

Warm-up time: 1 hour

Environmental Capability

Operating temperature: 10°C to 40°C (50°F to 105°F)

Altitude: Sea level to 3000 m(10,000 ft.)

Humidity: Below dew point

Power Requirements

Voltage: 115/230 V ±10%

Power: 125 watts

Physical Characteristics

Weight: Laser Head: 11.4 kg (25 lb.)

Power Supply: 3.5 kg (7.5 lb.)

Dimensions: 816 mm (L) x 83 mm (W) x 47 mm (H)

32.13 in (L) x 3.32 in (W) x 1.85 in

APPENDIX H

Image Processing Procedure

This Appendix contains a summary of the image processing that was applied to the raw images that were grabbed by the camera and the frame grabber before they were printed. The image processing included filtering the background and stray reflections when possible, extracting quantitative information from the images, drawing a 0.25 in x 0.25 in grid to give a feeling about the actual size of the image, and normalizing the image aspect ratio. The sequence of those image processes is presented in Figure H.1 (a through f). For printing, the images were saved in a bitmap format; then, they were imported to MS-POWER POINT for annotation. The images were copied into the MS-WINDOWS CLIP BOARD from MS-POWER POINT , then they were pasted into MS-WORD for printing. MS-Word automatically scaled the images to fit on the page.

H.1 Image filtering

For each jet image there was a background image that was grabbed before injecting the seed. The background image was subtracted from the jet images by subtracting the intensity values at each pixel in the back ground image from the intensity values at the corresponding pixels in the jet image. The background image was filtered by the image.c program. A listing of image.c is in Appendix N.1. This image filtering process works when the water inside the tank is reasonably clean and the seed concentration in the tank is very low. However, when the seed concentration in the tank increases, excessive seed floats in the tank and the water becomes very cloudy. Therefore the above filtering procedure becomes useless. Other types of image filtering were applicable like thresholding, in which the intensity value below or above a selected intensity value was set to zero. After filtering the image, an area of the image around the jet was selected and cropped. All parts of the image outside the cropped area were then discarded. This minimized the size of the image file and left out unnecessary parts of the image. Cropping the images was applied by the program process.c. A listing of the process.c source code is in Appendix N.2.

H.2 Extracting Quantitative Information

Extracting image information was done using the Xview image editor. Before importing the images into the Xview editor, it was necessary to convert the files from the DATA TRANSLATION .IMG format into the .PMG, Xview compatible format. In the .PMG format, the intensity is stored in an 8 bit character greyscale. The format conversion was done by the image.c program. A listing of the image.c program is in Appendix N.1. The Xview image editor allows zooming in on the images and it enables the user from reading the image pixel coordinates within ± 1 pixel resolution.

H.3 Drawing The Grid lines

Drawing the grid line on the images was done setting the intensity value for the pixel locations corresponding to the grid at some intensity value near the maximum intensity value in the buffer. The horizontal and vertical increment of the grid were calculated from the horizontal and vertical scale factors, respectively. The grid was drawn by the process.c program. A listing of the process.c program is in Appendix N.2.

H.4 Normalizing the Images Aspect Ratio

Normalizing the aspect ratio was accomplished using the Xview image editor. For the cross-sectional images, which were supposed to have a square grid, the image horizontal dimension was set equal to the image vertical dimension. For the axial jet images, the image horizontal dimension was adjusted according to the following equation:

$$I_h' = \frac{k_y}{k_x} I_h \qquad \text{(H.1)}$$

where I_h is the raw image horizontal dimension, I_h' is the image horizontal dimension after scaling. k_x is the image horizontal scale factor, and k_y is the image vertical scale factor.

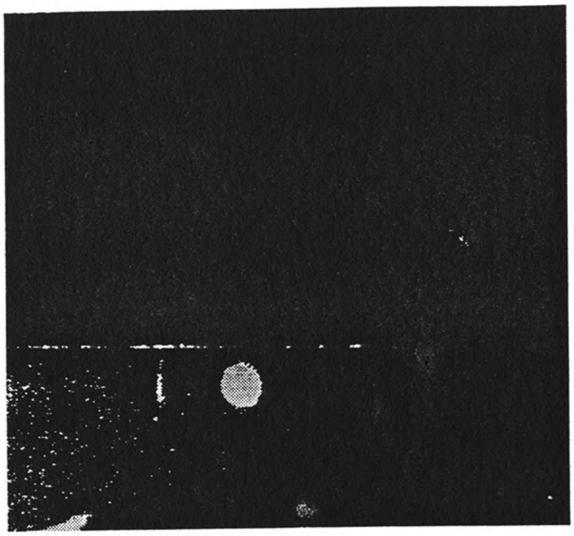

Figure H.1(a): Image Before Filtering

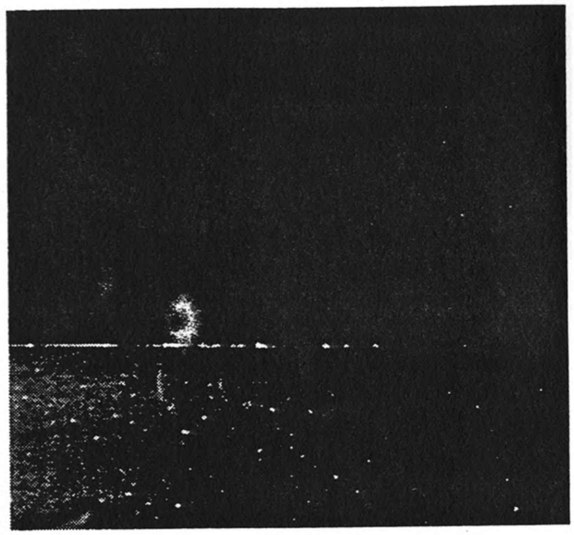

Figure H.1(b): Background Image

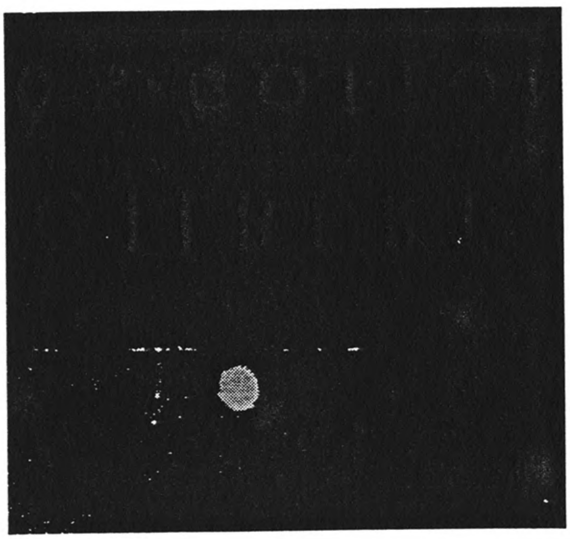

Figure H.1(c:): Image After Filtering

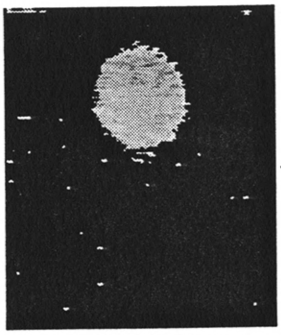

Figure H.1(d): Image after Cropping

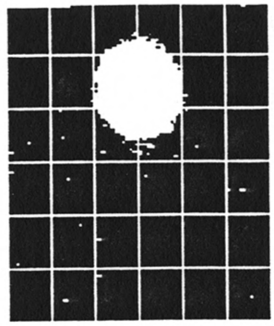

Figure H.1(e) : Image after Drawing Grid

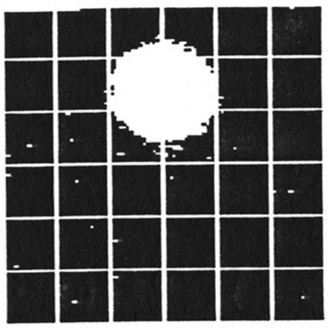

Figure H.1(f) : Image after Normalizing the Aspect Ratio

APPENDIX I

LIST OF RAW AND PROCESSED DATA

This Appendix contains lists of the quantitative data extracted from the images for the approximately isothermal laminar jet. The jet attachment lengths, measured from the axial jet images, are listed in Table I.1. The jet attachment lengths deduced from the cross-sectional jet images are listed in Table I.2. Table I.3 contains the extracted raw data from the cross-sectional images and Table I.4 has the calculated jet boundary coordinates ,as well as the horizontal and vertical dimensions of the jet. Table I.5 contains the raw and processed jet trajectory extracted from the axial images of the jet.

Ceiling-to-Nozzle height h, (in)	Measured Temperatures		Temperature Difference ΔT(°F)	Image Horizontal Horizontal scale factor k_x in/pixel	Measured Jet Attachment length	
	Discharge T_d (°F)	Abient T_∞(°F)			Pixels	inch
0.3750	71.6	71.5	0.1	0.0159	188	2.989
0.5625	71.5	71.4	0.1	0.0159	262	4.166
0.7500	71.8	71.4	0.4	0.0189	228	4.315
0.7500	71.8	71.0	0.8	0.0189	191	3.615
0.7500	72.9	71.7	1.2	0.0189	161	3.047
0.9375	72.0	71.8	0.2	0.0189	318	6.018
1.1250	72.4	72.2	0.2	0.0189	358	6.775

Table I.1: Axial Images Measurements Of the Jet to Wall Attachment

Ceiling-to-Nozzle height h, (in)	Measured Temperatures		Temperature Difference ΔT(°F)	Jet Attachment length L (in)
	Discharge T_d (°F)	Abient T_∞(°F)		
0.3750	71.4	71.1	0.3	2.4
0.5625	71.6	71.3	0.3	3.2
0.7500	72.0	71.8	0.2	4.8
0.7500	72.1	70.6	1.5	2.0
0.9375	73.4	73.1	0.3	5.6
1.1250	75.8	75.5	0.3	6.0

Table I.2: Cross-Sectional Measurements Of the Jet to Wall Attachment

Image Number	Distance from from Nozzle Exit inch	Reference Coordinates		Jet boundary Coordinates			
		Ceiling Vertical position Pixels	Nozzle Middle Plane Pixels	Vertical Dimension Pixels		Horizontal Dimension Pixels	
				Top	Bottom	Left	Right
1	0.0	313	213	324	370	194	231
2	0.4	313	213	322	370	194	231
3	0.8	313	212	319	370	193	230
4	1.2	313	212	320	371	192	231
5	1.6	312	211	319	372	191	230
6	2.0	313	211	317	371	190	231
7	2.4	316	211	316	372	189	233
8	2.8	316	211	316	372	187	235
9	3.2	315	211	315	373	183	239
10	3.6	317	213	317	372	180	245
11	4.0	317	213	317	372	175	251
12	4.4	317	216	317	370	170	261
13	4.8	315	218	315	368	160	275
14	5.2	315	218	315	367	151	285
15	5.6	315	224	315	365	139	308

Table I.3(a): Isothermal Cross-Sectional Images Raw Data for Ceiling-to-nozzle Height = 6/16 in

Image Number	Distance from Nozzle Exit inch	Scale factors		Jet Boundary Coordinates		Calculated Jet Dimensions	
		Horizontal kx pixel/inch	Vertical ky pixel/inch	Top inch	Bottom inch	Vertical inch	Horizontal inch
1	0.0	0.013779	0.011051	0.1516	0.6299	0.4784	0.5098
2	0.4	0.013480	0.010810	0.1213	0.6161	0.4948	0.4988
3	0.8	0.013182	0.010568	0.0791	0.6024	0.5233	0.4877
4	1.2	0.012883	0.010326	0.0902	0.5989	0.5087	0.5025
5	1.6	0.012585	0.010084	0.0881	0.6050	0.5169	0.4908
6	2.0	0.012287	0.009842	0.0491	0.5708	0.5217	0.5038
7	2.4	0.011988	0.009600	0.0000	0.5376	0.5376	0.5275
8	2.8	0.011690	0.009358	0.0000	0.5241	0.5241	0.5611
9	3.2	0.011391	0.009117	0.0000	0.5288	0.5288	0.6379
10	3.6	0.011093	0.008875	0.0000	0.4881	0.4881	0.7210
11	4.0	0.010795	0.008633	0.0000	0.4748	0.4748	0.8204
12	4.4	0.010496	0.008391	0.0000	0.4447	0.4447	0.9552
13	4.8	0.010198	0.008149	0.0000	0.4319	0.4319	1.1728
14	5.2	0.009899	0.007907	0.0000	0.4112	0.4112	1.3265
15	5.6	0.009601	0.007665	0.0000	0.3833	0.3833	1.6226

Table I.4(a): Isothermal Cross-Sectional Images Processed Data
for Ceiling-to-nozzle Height = 6/16 in

Image Number	Distance from from Nozzle Exit inch	Reference Coordinates: Ceiling Vertical position Pixels	Reference Coordinates: Nozzle Middle Plane Pixels	Jet boundary Coordinates: Vertical Dimension Pixels: Top	Vertical Dimension Pixels: Bottom	Horizontal Dimension Pixels: Left	Horizontal Dimension Pixels: Right
0	0.0	252	225	281	326	204	245
1	0.4	252	224	277	326	203	244
2	0.8	250	224	272	325	204	244
3	1.2	249	224	268	322	203	244
4	1.6	248	225	264	322	203	246
5	2.0	247	224	257	319	202	246
6	2.4	246	225	254	314	201	249
7	2.8	246	224	249	310	196	251
8	3.2	246	225	246	302	188	262
9	3.6	246	214	246	300	174	254
10	4.0	245	233	245	296	165	301
11	4.4	239	239	239	294	150	327
12	4.8	238	232	238	291	83	381
13	5.4	235	228	235	299	55	400
14	6.0	234	222	234	313	29	414
15	6.6	237	219	237	323	1	436

Table I.3(b): Isothermal Cross-Sectional Images Raw Data for Ceiling-to-nozzle Height = 9/16 in

Image Number	Distance from Nozzle Exit inch	Scale factors: Horizontal kx pixel/inch	Scale factors: Vertical ky pixel/inch	Jet Boundary Coordinates: Top inch	Jet Boundary Coordinates: Bottom inch	Calculated Jet Dimensions: Vertical inch	Calculated Jet Dimensions: Horizontal inch
0	0.0	0.013779	0.011051	0.3205	0.8178	0.4973	0.5649
1	0.4	0.013480	0.010810	0.2702	0.7999	0.5297	0.5527
2	0.8	0.013182	0.010568	0.2325	0.7926	0.5601	0.5273
3	1.2	0.012883	0.010326	0.1962	0.7538	0.5576	0.5282
4	1.6	0.012585	0.010084	0.1613	0.7462	0.5849	0.5412
5	2.0	0.012287	0.009842	0.0984	0.7086	0.6102	0.5406
6	2.4	0.011988	0.009600	0.0768	0.6528	0.5760	0.5754
7	2.8	0.011690	0.009358	0.0281	0.5989	0.5709	0.6429
8	3.2	0.011391	0.009117	0.0000	0.5105	0.5105	0.8430
9	3.6	0.011093	0.008875	0.0000	0.4792	0.4792	0.8874
10	4.0	0.010795	0.008633	0.0000	0.4403	0.4403	1.4681
11	4.4	0.010496	0.008391	0.0000	0.4615	0.4615	1.8578
12	4.8	0.010198	0.008149	0.0000	0.4319	0.4319	3.0390
13	5.4	0.009750	0.007786	0.0000	0.4983	0.4983	3.3638
14	6.0	0.009303	0.007424	0.0000	0.5865	0.5865	3.5815
15	6.6	0.008855	0.007061	0.0000	0.6072	0.6072	3.8520

Table I.4(b): Isothermal Cross-Sectional Images Processed Data for Ceiling-to-nozzle Height = 9/16 in

Image Number	Distance from Nozzle Exit inch	Reference Coordinates: Ceiling Vertical position Pixels	Reference Coordinates: Nozzle Middle Plane Pixels	Jet boundary Coordinates: Vertical Dimensions Pixels: Top	Jet boundary Coordinates: Vertical Dimensions Pixels: Bottom	Jet boundary Coordinates: Horizontal Dimensions Pixels: Left	Jet boundary Coordinates: Horizontal Dimensions Pixels: Right
1	0.0	279	292	321	367	272	312
2	0.4	279	292	320	367	272	312
3	0.8	277	292	317	366	272	312
4	1.2	275	292	314	365	272	312
5	1.6	275	292	311	365	272	312
6	2.0	273	292	307	364	272	312
7	2.4	273	293	302	364	272	314
8	2.8	271	295	293	360	273	316
9	3.2	270	296	287	358	273	319
10	3.6	268	297	281	351	273	321
11	4.0	268	300	275	346	273	327
12	4.4	267	300	272	335	270	329
13	4.8	265	295	265	327	257	332
14	5.2	263	293	263	318	242	344
15	5.6	261	292	261	312	223	361
16	6.0	257	293	257	307	199	386
17	6.4	254	222	254	298	169	274

Table I.3(c): Isothermal Cross-Sectional Images Raw Data for Ceiling-to-nozzle Height = 12/16

Image Number	Distance from Nozzle Exit inches	Scale factors: Horizontal kx pixel/inch	Scale factors: Vertical ky pixel/inch	Jet Boundary Coordinates: Top inch	Jet Boundary Coordinates: Bottom inch	Calculated Jet Dimensions: Vertical in	Calculated Jet Dimensions: Horizontal in
1	0.0	0.013779	0.011051	0.4642	0.9725	0.5084	0.5511
2	0.4	0.013480	0.010810	0.4432	0.9512	0.5080	0.5392
3	0.8	0.013182	0.010568	0.4227	0.9405	0.5178	0.5273
4	1.2	0.012883	0.010326	0.4027	0.9293	0.5266	0.5153
5	1.6	0.012585	0.010084	0.3630	0.9076	0.5445	0.5034
6	2.0	0.012287	0.009842	0.3346	0.8956	0.5610	0.4915
7	2.4	0.011988	0.009600	0.2784	0.8736	0.5952	0.5035
8	2.8	0.011690	0.009358	0.2059	0.8329	0.6270	0.5027
9	3.2	0.011391	0.009117	0.1550	0.8023	0.6473	0.5240
10	3.6	0.011093	0.008875	0.1154	0.7366	0.6212	0.5325
11	4.0	0.010795	0.008633	0.0604	0.6734	0.6129	0.5829
12	4.4	0.010496	0.008391	0.0420	0.5706	0.5286	0.6193
13	4.8	0.010198	0.008149	0.0000	0.5052	0.5052	0.7648
14	5.2	0.009899	0.007907	0.0000	0.4349	0.4349	1.0097
15	5.6	0.009601	0.007665	0.0000	0.3909	0.3909	1.3249
16	6.0	0.009303	0.007424	0.0000	0.3712	0.3712	1.7396
17	6.4	0.009004	0.007182	0.0000	0.3160	0.3160	0.9454

Table I.4(c): Isothermal Cross-Sectional Images Processed Data
for Ceiling-to-nozzle Height = 12/16 in

Image Number	Distance from Nozzle Exit inches	Reference Coordinates: Ceiling Vertical position Pixels	Reference Coordinates: Nozzle Middle Plane Pixels	Jet boundary Coordinates: Vertical Dimensions Pixels: Top	Vertical Dimensions Pixels: Bottom	Horizontal Dimensions Pixels: Left	Horizontal Dimensions Pixels: Right
1	0.0	264	261	323	367	242	279
2	0.4	261	261	321	367	241	280
3	0.8	259	261	320	367	241	280
4	1.2	258	261	318	367	241	280
5	1.6	262	261	317	366	240	281
6	2.0	256	261	313	362	240	281
7	2.4	253	261	309	363	239	283
8	2.8	252	261	303	361	237	284
9	3.2	251	261	297	357	236	286
10	3.6	248	261	289	352	235	287
11	4.0	247	262	281	344	235	289
12	4.4	245	260	270	337	230	290
13	4.8	243	260	261	327	226	294
14	5.2	240	258	252	316	219	297
15	5.6	241	254	242	301	201	307
16	6.0	238	250	238	292	180	319
17	6.4	227	238	227	269	83	393

Table I.3(d): Isothermal Cross-Sectional Images Raw Data for Ceiling-to-nozzle Height = 15/16 in

Image Number	Distance from Nozzle Exit inches	Scale factors: Horizontal kx pixel/inch	Scale factors: Vertical ky pixel/inch	Jet Boundary Coordinates: Top inch	Jet Boundary Coordinates: Bottom inch	Calculated Jet Dimensions: Vertical in	Calculated Jet Dimensions: Horizontal in
1	0.0	0.013779	0.011051	0.6520	1.1383	0.4863	0.5098
2	0.4	0.013480	0.010810	0.6486	1.1458	0.4972	0.5257
3	0.8	0.013182	0.010568	0.6446	1.1413	0.4967	0.5141
4	1.2	0.012883	0.010326	0.6195	1.1255	0.5060	0.5025
5	1.6	0.012585	0.010084	0.5546	1.0487	0.4941	0.5160
6	2.0	0.012287	0.009842	0.5610	1.0433	0.4823	0.5038
7	2.4	0.011988	0.009600	0.5376	1.0560	0.5184	0.5275
8	2.8	0.011690	0.009358	0.4773	1.0201	0.5428	0.5494
9	3.2	0.011391	0.009117	0.4194	0.9664	0.5470	0.5696
10	3.6	0.011093	0.008875	0.3639	0.9230	0.5591	0.5768
11	4.0	0.010795	0.008633	0.2935	0.8374	0.5439	0.5829
12	4.4	0.010496	0.008391	0.2098	0.7720	0.5622	0.6298
13	4.8	0.010198	0.008149	0.1467	0.6845	0.5378	0.6935
14	5.2	0.009899	0.007907	0.0949	0.6009	0.5061	0.7722
15	5.6	0.009601	0.007665	0.0077	0.4599	0.4523	1.0177
16	6.0	0.009303	0.007424	0.0000	0.4009	0.4009	1.2931
17	6.4	0.009004	0.007182	0.0000	0.3016	0.3016	2.7913

Table I.4(d): Isothermal Cross-Sectional Images Processed Data
for Ceiling-to-nozzle Height = 15/16 in

Image Number	Distance from Nozzle Exit inch	Reference Coordinates		Jet boundary Coordinates			
		Ceiling Vertical position Pixels	Nozzle Middle Plane Pixels	Vertical Dimensions Pixels		Horizontal Dimensions Pixels	
				Top	Bottom	Left	Right
1	0.0	241	248	315	358	230	266
2	0.4	238	248	314	358	230	266
3	0.8	237	248	310	358	228	267
4	1.2	235	248	308	357	228	267
5	1.6	232	247	301	356	226	268
6	2.0	230	247	297	354	225	268
7	2.4	227	247	293	351	224	269
8	2.8	226	246	284	349	222	269
9	3.2	223	246	278	344	221	270
10	3.6	219	244	266	340	218	270
11	4.0	215	244	258	335	215	273
12	4.4	212	244	249	327	214	273
13	4.8	208	243	235	318	213	272
14	5.2	205	242	224	305	210	274
15	5.6	202	241	212	292	206	276
16	6.0	198	240	200	267	191	289
17	6.4	194	241	194	251	166	316
18	6.8	191	245	191	232	141	349

Table I.3(e): Isothermal Cross-Sectional Images Raw Data for Ceiling-to-nozzle Height = 18/16 in

Image Number	Distance from Nozzle Exit inch	Scale factors		Jet Boundary Coordinates		Calculated Jet Dimensions	
		Horizontal kx pixel/inch	Vertical ky pixel/inch	Top inch	Bottom inch	Vertical inch	Horizontal inch
1	0.0	0.013779	0.011051	0.8178	1.2930	0.4752	0.4960
2	0.4	0.013480	0.010810	0.8215	1.2971	0.4756	0.4853
3	0.8	0.013182	0.010568	0.7714	1.2787	0.5072	0.5141
4	1.2	0.012883	0.010326	0.7538	1.2597	0.5060	0.5025
5	1.6	0.012585	0.010084	0.6958	1.2504	0.5546	0.5286
6	2.0	0.012287	0.009842	0.6594	1.2204	0.5610	0.5283
7	2.4	0.011988	0.009600	0.6336	1.1904	0.5568	0.5395
8	2.8	0.011690	0.009358	0.5428	1.1511	0.6083	0.5494
9	3.2	0.011391	0.009117	0.5014	1.1031	0.6017	0.5582
10	3.6	0.011093	0.008875	0.4171	1.0738	0.6567	0.5768
11	4.0	0.010795	0.008633	0.3712	1.0359	0.6647	0.6261
12	4.4	0.010496	0.008391	0.3105	0.9650	0.6545	0.6193
13	4.8	0.010198	0.008149	0.2200	0.8964	0.6764	0.6017
14	5.2	0.009899	0.007907	0.1502	0.7907	0.6405	0.6336
15	5.6	0.009601	0.007665	0.0767	0.6899	0.6132	0.6721
16	6.0	0.009303	0.007424	0.0148	0.5122	0.4974	0.9117
17	6.4	0.009004	0.007182	0.0000	0.4094	0.4094	1.3506
18	6.8	0.008706	0.006940	0.0000	0.2845	0.2845	1.8108

Table I.4(e): Isothermal Cross-Sectional Images Processed Data
for Ceiling-to-nozzle Height = 18/16 in

Measured Jet Trajectory Pixels			Calculated Jet Trajectory inch		
Horizontal	upper edge	Lower edge	Horizontal	upper edge	Lower edge
415	11	52	0	0.1320	0.6240
384	11	51	0.4929	0.1320	0.6120
353	10	50	0.9858	0.1200	0.6000
323	9	48	1.4628	0.1080	0.5760
291	6	44	1.9716	0.0720	0.5280
260	4	42	2.4645	0.0480	0.5040
229	3	38	2.9574	0.0360	0.4560
198	1	36	3.4503	0.0120	0.4320
167	0	32	3.9432	0.0000	0.3840
136	0	29	4.4361	0.0000	0.3480
105	0	25	4.929	0.0000	0.3000
74	0	22	5.4219	0.0000	0.2640
43	0	20	5.9148	0.0000	0.2400
12	0	18	6.4077	0.0000	0.2160
Image Horizontal scale factor (Kx):				0.0159	inch/pixel
Image Vertical scale factor (ky) :				0.0120	inch/pixel
Measured Vertical Ceiling Location:				136	pixels
Measured Backwall Horizontal Location:				415	pixels

Table I.5 (a): Isothermal Jet Axial Image Data for Ceiling-to-Nozzle Height= 6/16 in

Measured Jet Trajectory Pixels			Calculated Jet Trajectory inch		
Horizontal	upper edge	Lower edge	Horizontal	upper edge	Lower edge
415	26	65	0	0.3120	0.7800
385	25	63	0.477	0.3000	0.7560
354	22	61	0.9699	0.2640	0.7320
323	19	58	1.4628	0.2280	0.6960
293	16	56	1.9398	0.1920	0.6720
261	13	55	2.4486	0.1560	0.6600
229	10	51	2.9574	0.1200	0.6120
199	7	50	3.4344	0.0840	0.6000
167	5	48	3.9432	0.0600	0.5760
136	0	41	4.4361	0.0000	0.4920
106	0	37	4.9131	0.0000	0.4440
75	0	35	5.406	0.0000	0.4200
44	0	31	5.8989	0.0000	0.3720
12	0	28	6.4077	0.0000	0.3360
Image Horizontal scale factor (Kx):				0.0159	inch/pixel
Image Vertical scale factor (ky) :				0.0120	inch/pixel
Measured Vertical Ceiling Location:				136	pixels
Measured Backwall Horizontal Location:				415	pixels

Table I.5 (b): Isothermal Jet Axial Image Data for Ceiling-to-Nozzle Height= 9/16 in

Measured Jet Trajectory Pixels			Calculated Jet Trajectory inch		
Horizontal	upper edge	Lower edge	Horizontal	upper edge	Lower edge
435	35	68	0	0.4935	0.9588
412	31	61	0.4347	0.4371	0.8601
386	28	59	0.9261	0.3948	0.8319
362	25	58	1.3797	0.3525	0.8178
337	22	55	1.8522	0.3102	0.7755
312	15	53	2.3247	0.2115	0.7473
286	10	48	2.8161	0.1410	0.6768
261	6	43	3.2886	0.0846	0.6063
235	3	39	3.78	0.0423	0.5499
211	1	31	4.2336	0.0141	0.4371
186	0	25	4.7061	0.0000	0.3525
161	0	20	5.1786	0.0000	0.2820
135	0	17	5.67	0.0000	0.2397
111	0	15	6.1236	0.0000	0.2115
86	0	15	6.5961	0.0000	0.2115
61	0	16	7.0686	0.0000	0.2256
36	0	18	7.5411	0.0000	0.2538
11	0	21	8.0136	0.0000	0.2961
Image Horizontal scale factor (Kx):				0.0189	inch/pixel
Image Vertical scale factor (ky) :				0.0141	inch/pixel
Measured Vertical Ceiling Location:				107	pixels
Measured Backwall Horizontal Location:				435	pixels

Table I.5 (c): Isothermal Jet Axial Image Data for Ceiling-to-Nozzle Height= 12/16 in

Measured Jet Trajectory Pixels			Calculated Jet Trajectory inch		
Horizontal	upper edge	Lower edge	Horizontal	upper edge	Lower edge
435	48	80	0	0.6768	1.1280
411	43	74	0.4536	0.6063	1.0434
385	41	72	0.945	0.5781	1.0152
362	38	71	1.3797	0.5358	1.0011
335	37	68	1.89	0.5217	0.9588
311	34	66	2.3436	0.4794	0.9306
286	30	64	2.8161	0.4230	0.9024
262	25	61	3.2697	0.3525	0.8601
237	21	58	3.7422	0.2961	0.8178
210	15	51	4.2525	0.2115	0.7191
185	11	50	4.725	0.1551	0.7050
161	6	46	5.1786	0.0846	0.6486
136	4	41	5.6511	0.0564	0.5781
110	2	35	6.1425	0.0282	0.4935
86	0	29	6.5961	0.0000	0.4089
60	0	24	7.0875	0.0000	0.3384
35	0	20	7.56	0.0000	0.2820
12	0	20	7.9947	0.0000	0.2820
Image Horizontal scale factor (Kx):				0.0189	inch/pixel
Image Vertical scale factor (ky) :				0.0141	inch/pixel
Measured Vertical Ceiling Location:				107	pixels
Measured Backwall Horizontal Location:				435	pixels

Table I.5 (d): Isothermal Jet Axial Image Data for Ceiling-to-Nozzle Height= 15/16 in

Measured Jet Trajectory Pixels			Calculated Jet Trajectory inch		
Horizontal	upper edge	Lower edge	Horizontal	upper edge	Lower edge
432	61	92	0.0579	0.8601	1.2972
411	54	85	0.4632	0.7614	1.1985
387	53	84	0.9264	0.7473	1.1844
362	51	81	1.4089	0.7191	1.1421
337	49	80	1.8914	0.6909	1.1280
311	47	78	2.3932	0.6627	1.0998
285	43	76	2.895	0.6063	1.0716
261	39	74	3.3582	0.5499	1.0434
235	33	67	3.86	0.4653	0.9447
211	29	62	4.3232	0.4089	0.8742
186	24	56	4.8057	0.3384	0.7896
161	18	52	5.2882	0.2538	0.7332
136	13	45	5.7707	0.1833	0.6345
111	8	39	6.2532	0.1128	0.5499
60	0	34	7.2375	0.0000	0.4794
35	0	27	7.72	0.0000	0.3807
11	0	26	8.1832	0.0000	0.3666
Image Horizontal scale factor (Kx):				0.0189	inch/pixel
Image Vertical scale factor (ky) :				0.0141	inch/pixel
Measured Vertical Ceiling Location:				107	pixels
Measured Backwall Horizontal Location:				435	pixels

Table I.5 (e): Isothermal Jet Axial Image Data for
Ceiling-to-Nozzle Height= 18/16 in

APPENDIX J

Flowmeter Calibration

An F&P-10A3555 flow meter was used to measure the nozzle discharge water flowrate. The flow meter full-scale range of 0.81 GPM (at 100%) with a 1% resolution. The flowmeter normally was repeatable to within 0.1-0.2 divisions; however, the laminar flow tests were very low on the scale which made calibration necessary. For the laminar jet images, the nozzle discharge flowrate was such that the flowmeter float pointed at the lowest flowmeter mark. See Figure J.1 for the position of the flow meter mark used for the laminar jet tests.

The flowmeter was calibrated using the volume collection method. The flowmeter discharge was collected in a glass beaker, and the time during which the flowmeter discharged into the beaker was recorded. The volume flow rate was calculated in gallon per minute (GPM) from the measured time and collected water mass as

$$\dot{V} = \frac{m}{\rho \cdot t} \tag{J.1}$$

where $\dot{V}$ is the volume flow rate, m is the mass collected during the volume collection process, ρ is the water density, and t is the time of the volume collection process. The density was interpolated from steam tables using the measured water temperature. The mass was weighed by a scale to within ± one tenth of a gram. The empty beaker was put on the scale and the scale reading was zeroed before water from the flowmeter discharge was directed into the beaker. After the time of the water collection process elapsed, the beaker was weighed again to estimate the net mass of the collected water. The time of the water collection was measured using a stop watch with 0.01 second resolution. Another source of error in the time measurement was the reaction time which was estimated to be 0.5 second. The mass flowrate was measured several times for each calibration settings. The average water volume flowrate was considered the true reading of the scale. The random uncertainty, E_R, in the flowmeter calibration (using a 95% confidence interval) was approximated as twice the standard deviation of the water flowrate measurements (σ_V, GPM). Neglecting the error in the density, the absolute uncertainty in the volume flow rate (E_v) becomes

$$E_v = \sqrt{(\frac{E_m}{\rho \cdot t})^2 + (\frac{E_t}{\rho \cdot t^2})^2 + (2\sigma_v)^2} \qquad \text{(J.2)}$$

where E_m is the uncertainty in the mass measurement and E_t is the uncertainty in the time measurement.

Table J.1 contains the average volume flow rate measurements, the standard deviation of the measured water flowrate , and absolute uncertainty in the volume flowrate measurements. Tables J.2 (a) through J.2 (f) contain the raw data for the flowmeter calibration.

Sample Calculation

For the first data point, it was found that the calculated mass was m= 203.1± 0.1 grams, the time of collection was t= 139.42 ± 0.5 seconds ,and the temperature T= 71±1.0. From the temperature, the density of water ρ was found to be 998.05 kg/m^3. The mass flow rate is thus

:

$$\dot{V} = \frac{203.1\ gm}{139.42\ s\ x\ 977.042\frac{kg}{m^3}} \bullet \frac{1.5850\ x\ 10^4\ \frac{GPM}{(\frac{m^3}{s})}}{1000\frac{gm}{kg}} = 0.023GPM$$

The standard deviation of the water volumetric flow rate for the first data set was estimated to be 0.0002 GPM, which yields a 95% confidence uncertainty of ±0.0004 GPM. :

$$E_v = \pm\sqrt{(0.0004)^2 + (0.0001)^2} = \pm 0.0004\ GPM$$

The uncertainty in the flow rate measurements is calculated by substituting into Equation J.2

$$E_{v,m} = \pm\sqrt{(\frac{0.1\ gm}{977.048\ (\frac{kg}{m^3})\ x\ 139.42\ s})^2 + (\frac{0.5\ s\ x\ 203.1\ gm}{977.048\ (\frac{kg}{m^3})(139.42\ s)^2})^2 + (0.0004)^2} \bullet \frac{15850\ \frac{GPM}{(\frac{m^3}{s})}}{1000\frac{gm}{kg}} = \pm 0.0004\ GPM$$

Flowmeter Number of Divisions	Water Average Flow rate V (GPM)	Water flow Rate Staandar of Deviation σv	Absolute Flowrate Uncertainty GPM	Relative Flowrate Uncertainty (%)
1	0.023	0.0002	0.0004	1.74%
2	0.054	0.0004	0.0009	1.67%
3	0.062	0.0001	0.0004	0.60%
4	0.068	0.0003	0.0007	1.03%
5	0.078	0.0005	0.001	1.28%
6	0.09	0.0006	0.0012	1.30%

Table J.1: Flowmeter Calibration

Mass Grams	Time Seconds	Temperature °F
203.1	139.42	71.0
185.3	128.99	71.1
180.4	126.56	71.3
182.6	128.28	71.4
176.7	124.59	71.6
182.4	128.78	71.7
179.3	126.57	71.8

Table J.2 (a): 1 division

Mass Grams	Time Seconds	Temperature °F
311.3	92.37	70.8
319.0	96.94	71.4
303.9	91.7	71.4
317.4	96.06	71.6
307.2	92.94	71.7
305.9	92.66	71.8
307.4	93.35	72.0
302.3	92.09	72.1

Table J.2 (b): 2 division

Mass Grams	Time Seconds	Temperature °F
384.7	100.72	72.4
387.0	101.65	72.5
390.2	102.58	72.6
388.1	102.04	72.7
383.3	101.05	72.9
385.5	101.67	73.0

Table J.2 (c): 3 division

Mass Grams	Time Seconds	Temperature °F
437.6	103.2	73.0
429.0	101.6	73.1
434.2	103.0	73.1
436.0	103.6	73.2
436.3	103.6	73.2
427.3	101.9	73.2
424.9	101.5	73.2

Table J.2 (d): 4 division

Mass Grams	Time Seconds	Temperature °F
497.0	102.0	72.3
493.0	102.3	72.8
492.2	102.5	72.7
483.2	100.7	72.7
493.3	103.2	72.7
49.2	102.1	72.7
489.5	102.4	72.8

Table J.2 (e): 5 division

Mass Grams	Time Seconds	Temperature °F
567.3	101.6	72.9
568.8	101.7	72.7
566.5	101.7	72.6
563.0	101.3	72.6
563.3	101.7	72.6
564.5	101.9	72.6
552.7	100.9	72.5

Table J.2 (f): 6 division

Table J.2 : Flowmeter Calibration Raw Data

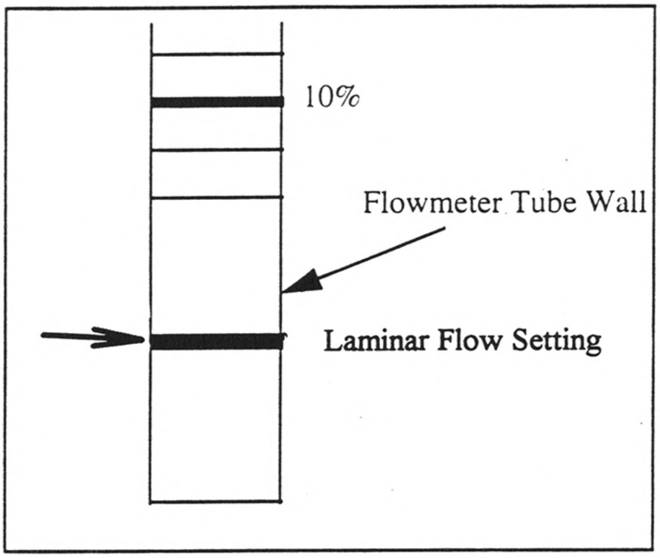

Figure J.1: Flowmeter Calibration

APPENDIX K

Thermocouple Calibration and Temperature Measurement Evaluation

This Appendix contains the thermocouple calibration and the uncertainty analysis for the thermocouple measurements. Although thermocouple junction measuring the jet discharge temperature was separated from the nozzle opening by the nozzle length, the actual discharge temperature was not expected to be different by very much. Thermal analysis of the jet discharge nozzle temperature is also included in this section.

K.1 Thermocouple Calibration

Since the purpose of the temperature measurement was monitoring the temperature difference between the water at the nozzle discharge and the ambient water inside the tank, the thermocouple junctions were calibrated against each other. This provided a measure of how different the thermocouple characteristics were. All the thermocouple junctions were packed closely together and immersed in a bath of water. The average temperature reading of all the thermocouple junctions were considered to be the true temperature (73.6 °F). The uncertainty in the temperature measurement consisted of the statistical error and the instrument error. The instrument error associated with the junction and the Doric 403A digital temperature indicator used with type T copper-constant thermocouple wire was about (±1 °F) . The Doric 403A digital temperature indicator resolution was (0.1 °F). Then, the resolution uncertainty of the temperature measurement is within ± 0.05 °F. The statistical error, with a 95% confidence interval, was about ±0.1°F. Table K.1 contains the thermocouple number, its measurement, and the uncertainty in each of the measurements. For estimating the uncertainty in the temperature difference, the thermocouples will each have an offset error. Hence, the contribution of the uncertainty in the temperature difference measurement is limited to the Doric-403A indicator resolution and the temperature calibration error which is the deviation of the single thermocouple measurement from the average temperature of all the thermocouples. It is estimated, within a 95% confidence level, as twice the standard deviation of the single thermocouple temperature measurement from the average temperature, σ_T. Combining the uncertainty sources in the temperature difference measurement, the uncertainty in the temperature difference measurement becomes 0.11 °F.

Thermocouple	Temperature (°F)
1	73.5 ± 1.0
2	73.6 ± 1.0
3	73.6 ± 1.0
4	73.7 ± 1.0
5	73.6 ± 1.0
6	73.8 ± 1.0
7	73.8 ± 1.0

Table K.1: Thermocouples Calibration

<u>Sample Calculation of Temperature Uncertainty</u>

$T_{avg} = 73.6$ °F
$\sigma_T = \pm 0.1$ °F
$E_{resolution} \pm 0.05$ °F
$$E_{\Delta T} = \sqrt{0.1 \cdot 0.1 + 0.05 \cdot 0.05} = 0.11^{\circ}F$$

K.2 Thermal Analysis of Nozzle Discharge Temperature Measurement

Since the thermocouple junction used for measuring the temperature of the nozzle discharge was placed in the reinforced PVC hosing, and the location of the temperature measurement was separated from the nozzle opening by the length of the nozzle assembly, the temperature measured would be different from the actual temperature at the nozzle opening. The possible temperature change is a function of the temperature difference between the water inside the tube and the ambient water. Looking at the simplified schematic on Figure K, an energy balance yields

$$\rho \dot{v} C_P (T_2 - T_1) = h \pi D L \Delta T \qquad \text{(K.1)}$$

where ρ is the density of water (1000 kg/m^3), v is the volume flowrate (0.02340 GPM), C_p (4.2 kJ/kg.k) is the water specific heat, h is the connective heat transfer coefficient approximately (2000 w/m^2.C), D is the diameter of the tube (0.5 inch), L is the length of the pipe immersed in water (6 inches), and ΔT is the temperature difference between the water in the tube and the ambient water temperature. Solving for the temperature difference between the inlet and the exit temperature yields

$$T_2 - T_1 = \frac{h \pi D L}{\rho \dot{v} C_P} \Delta T \qquad \text{(K.2)}$$

Substituting the values of the different parameters, yields

$$T_2 - T_1 = 0.111 \cdot \Delta T \, ^\circ C \qquad \text{(K.3)}$$

which is relatively small, but not insignificant, for the range of the ΔT used in the current experiments.

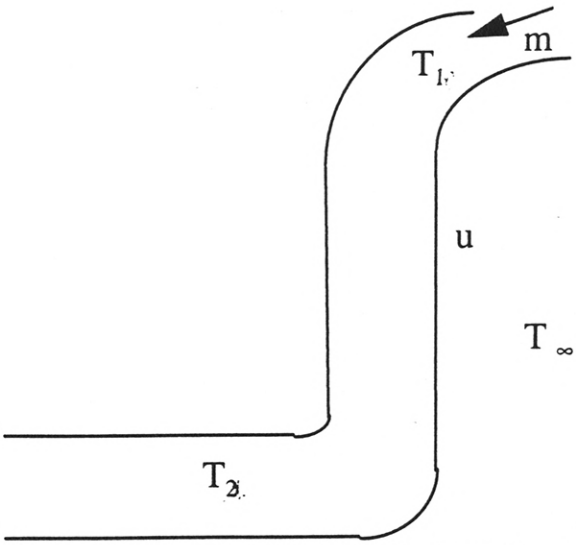

Figure K.1: Schematic of the Jet Discharge Temperature Thermal Analysis

APPENDIX L

Raw Image Files List

L.1 Cross-Sectional Raw Image File List

L.1.1 Isothermal Cross-Sectional Raw Image File List

Ceiling-to-Nozzle Height	Raw Image File	Background Image File
6/16 in	cs0_*.img	csbk0_*.img
9/16 in	cs1_*.img	csbk1_*.img
12/16 in	cs2_*.img	csbk2_*.img
15/16 in	cs3_*.img	csbk3_*.img
18/16 in	cs4_*.img	csbk4_*.img

Table L.1: Isothermal Cross-Sectional File List

Independent Tests are represented using the following format; e.g., cs0_*.img where * represents a multiple of a 0.4 in increment in cross-section position.

L.1.2 Buoyant Isothermal Cross-Sectional Axial Raw Image File List

Temperature Difference Between the Jet Discharge Ceiling-to-Nozzle Height ΔT	Image File
-0.8 ° F	csbo_1.img
-0.6 ° F	csbo_2.img
-0.3 ° F	csbo_3.img
-0.1 ° F	csbo_4.img
0.0 ° F	csbo_5.img
0.1 ° F	csbo_6.img
0.2 ° F	csbo_7.img
0.3 ° F	csbo_8.img
0.6 ° F	csbo_9.img
0.8 ° F	csbo_10.img
1.0 ° F	csbo_11.img
1.3 ° F	csbo_12.img
1.5 ° F	csbo_13.img
1.7 ° F	csbo_14.img

Table L.2: File List of the Cross-Sectional Images of Buoyant Jet

L.1.3 Variable Flowrate Cross-Sectional Raw Image File List

Flowrate At Nozzle Discharge	Image File
0.0227 GPM	csfl1_*.img
0.0525 GPM	csfl2_*.img
0.0604 GPM	csfl3_*.img

Table L.3: File List of the Cross-Sectional Variable Flowrate Jet Images

L.2 Axial Raw Image File List

L.2.1 Isothermal Axial Raw Image File List

Ceiling-to-Nozzle Height	Raw Image File	Background Image File
6/16 in	ax0.img	axbk0.img
9/16 in	ax1.img	axbk1.img
12/16 in	ax2.img	axbk2.img
15/16 in	ax3.img	axbk3.img
18/16 in	ax4.img	axbk4.img

Table L.4: Isothermal Axial File List

L.2.2 Buoyant Isothermal Axial Raw Image File List

Temperature Difference Between the Jet Discharge Ceiling-to-Nozzle Height ΔT	Image File
-1.2 ° F	axbo_1.img
-1.0 ° F	axbo_2.img
-0.8 ° F	axbo_3.img, axbo_4.img
-0.6 ° F	axbo_5.img, axbo_6.img
-0.3 ° F	axbo_7.img
-0.2 ° F	axbo_8.img, axbo_9.img
0.4 ° F	ax_3.img
0.8 ° F	axbo_10.img
1.2 ° F	axbo_11.img

Table L.5: File List of the Axial Images of Buoyant Jet

L.2.3 Variable Flowrate Axial Raw Image File List

Flowrate At Nozzle Discharge	Image File
0.0227 GPM	axfl1_*.img
0.0525 GPM	axfl2_*.img
0.0604 GPM	axfl3_*.img

Table L.6: File List of the Axial Variable Flowrate Jet Images

APPENDIX M

REAL TIME IMAGE ACQUISITION PROGRAM SOURCE CODE

M.1 File: mach.asm

Programmer: Kent D. Funk

```
_TEXT       SEGMENT  WORD PUBLIC 'CODE'
_TEXT       ENDS
_DATA       SEGMENT  WORD PUBLIC 'DATA'
_DATA       ENDS
CONST       SEGMENT  WORD PUBLIC 'CONST'
CONST       ENDS
_BSS  SEGMENT  WORD PUBLIC 'BSS'
_BSS  ENDS
DGROUP      GROUP       CONST, _BSS, _DATA
            ASSUME DS: DGROUP, SS: DGROUP

_TEXT       SEGMENT
            ASSUME      CS:_TEXT
            PUBLIC      __Kigate
;-------------------------------------------------------------------------------
;       __Kigate : Universal Kernel Interrupt Gate.
;
;       A generic, parameterized vector table call gate is constructed as:
;
;       Vector Table:           igate_s:
;       /------------\LO        /------------------------------\LO
;       |          |  /------->| uchar opcode9A   'CALL FAR'  |
;       |------------|  |       |------------------------------|
; xx| void far *------/  /-------void (far *_Kigate)(void)    |
;       |------------|     |    |------------------------------|
;       |          |     |    | void far *usrp             |<-----\
;       \------------/HI   |  |------------------------------|     |
;                 |   | void (far *ifunc)(intargs_s) |<-----|-----\
;                 |   \------------------------------/HI   |    |
;                 |                                  |    |
__Kigate PROC FAR ;<-----/                               |    |
pusha    ;                          |    |
push   ds;          Stack, intargs_s:            |    |
push   es;         /------------------------------\HI  |    |
       ;       +28| FLAGS  | INT xx             |    |    |
          ;        |---------                |    |    |
```

```
;	+26| CS	|	|  |  |
			;	|---------	|  |  |
;	+24| IP	|	|  |  |
		;	|-------------------------------|  |  |
;	+22| CS	| CALL FAR __Kigate  |  |  |
		;	|---------	|  |  |
;	+20| IP	| void far * far *gate-------/  |
		;	|-------------------------------|	|
;	+18| AX	| PUSHA	^	|	|
		;	|---------	|	|	|
;	+16| CX	|	|	|	|
		;	|---------	|	|	|
;	+14| DX	|	|	|	|
		;	|---------	|	|	|
;	+12| BX	|	|	|	|
		;	|---------	|	|	|
;	+10| SP ------------------/	|	|
		;	|---------	|	|
;	+08| BP	|	|	|
		;	|---------	|	|
;	+06| SI	|	|	|
		;	|---------	|	|
;	+04| DI	|	|	|
		;	|-------------------------------|	|
;	+02| DS	| PUSH DS	|	|
		;	|-------------------------------|	|
		;	+00| ES	| PUSH ES	|<-- BP,SP |
		;	\-------------------------------/LO	|
		;			|
			; Setup a Standard 'C' Environment.	|
			mov	bp,sp	;	|
			mov	ax,DGROUP	;	|
			mov	ds,ax	;	|
			cld		;	|
	;			|
; Call 'ifunc(intargs_s)' through double far indirection.	|
les	bx,DWORD PTR [bp+20]	;	|
call	DWORD PTR es:[bx+4]	;-----------------------------------/
;
; Unwind the Stack and ReTurn from Interrupt.
```

```
                mov         sp,bp
                pop         es
                pop         ds
popa
add             sp,4            ; !!NOTE: throw away CALL FAR __Kigate!!
iret
__Kigate                ENDP

                PUBLIC      __Klock
                PUBLIC      __Kulock
;-----------------------------------------------------------------------------
;       __Klock/__Kulock : Lock/Unlock the kernel.
;
__Klock                     PROC FAR
pushf
cli
pop             ax
ret
__Klock                     ENDP
__Kulock                PROC FAR
                push    bp
                mov         bp,sp
                mov         ax,[bp+6]
                push    ax
popf
pop             bp
ret
__Kulock                ENDP

                PUBLIC      __Ksetivec
;-----------------------------------------------------------------------------
;       __Ksetivec : Set interrupt vectors, return old value.
;
__Ksetivec              PROC FAR
                push    bp
        mov             bp,sp                           ; 6[bp] := ivector #
                push    ds                                  ; 8[bp] := new
ivector
pushf
                mov         bx,[bp+6]                   ; fetch the ivector #
                shl         bx,2                                ; scale it by 4
```

```
        xor     ax,ax                   ; set DS= 0
        mov     ds,ax

        cli                             ; lock the CPU
        les     ax,DWORD PTR [bx]       ; ES:AX = the old
vector
        mov     dx,es           DX:AX = the old vector, for return
        les     cx,DWORD PTR [bp+8] ; ES:CX = the new vector
        mov     [bx],cx                         ; set the offset
        mov     [bx+2],es                       ; set the
segment
        popf                            ; restore the stack frame
        pop     ds
        pop     bp
ret
__Ksetivec              ENDP

        PUBLIC          __Kgetivec
;-----------------------------------------------------------------------------
;       __Kgetivec : Get interrupt vector.

;
__Kgetivec              PROC FAR
        push    bp
        mov             bp,sp                           ; 6[bp] :=
ivector #
pushf
        mov             bx,[bp+6]               ; fetch the ivector #
        shl             bx,2                            ; scale it by 4
        xor             ax,ax                           ; set ES= 0
        mov             es,ax

        cli                                                     ; lock
the CPU
        les             ax,DWORD PTR es:[bx]    ; ES:AX = the old
vector
        mov             dx,es   DX:AX = the old vector, for return
        popf             ;   restore the stack frame
        pop             bp
ret
__Kgetivec              ENDP

_TEXT
ENDS
```

M.2 File: mach.h

Programmer: Kent D. Funk

```
#ifndef _MACH_H
#define _MACH_H

#ifndef _SIZE_T_DEFINED
#define _SIZE_T_DEFINED
typedef unsigned int                    size_t;
#endif

#ifndef _MACH_T
#define _MACH_T

/* --- Standard Machine Types --- */
typedef unsigned long               ulong;
typedef unsigned int               ushort;
typedef unsigned char               uchar;
typedef volatile unsigned int   v_ushort;
typedef volatile unsigned char          v_uchar;

#define __far _far
#define __cdecl _cdecl
#define __interrupt _interrupt

#pragma pack(1)
typedef union _word_u {
        struct {
                uchar  l;
                uchar  h;
        }                       b;
        ushort          w;
} word_u;
typedef union _addr_u {
        struct {
                ushort  offset;
                ushort  segment;
        }                       w;
        ulong           l;
} addr_u;
#pragma pack()

#endif /* _MACH_T */
```

```
/* --- Interrupt Call Gate Arguments --- */
#pragma pack(2)
typedef struct _intargs_s {
        ushort          es;
        /* PUSH ES              */
        ushort          ds;
        /* PUSH DS              */
        ushort          di,si,bp,sp;            /* PUSHA            */
        ushort          bx,dx,cx,ax;            /*      ...         */
        void            __far * __far *gate;    /* CALL_GATE        */
        ushort          ip,cs,flags;            /* INT xx           */
} intargs_s;
#pragma pack()

/* --- Interrupt Gates --- */
#pragma pack(1)
typedef struct _igate_s {
        uchar           opcode9A;
        void            (__far *_Kigate)(void);
        void            __far *usrp;
        void            (__far *ifunc)(intargs_s);
} igate_s;
#pragma pack()

/* --- Machine Function Declarations --- */
extern void             __far __cdecl _Kigate(void);
extern ushort   __far __cdecl _Klock(void);
extern void             __far __cdecl _Kulock(ushort);
extern void             (__cdecl __interrupt __far * __cdecl __far _Ksetivec(
                                ushort, void (__cdecl __interrupt __far *)()))();
extern void             (__cdecl __interrupt __far * __cdecl __far
_Kgetivec(ushort))();

/* --- Compiler Intrinsic Declarations --- */
extern void             __cdecl                         _enable(void);
extern void     __cdecl                         _disable(void);
extern int              __cdecl                         outp(ushort, int);
extern ushort   __cdecl                         outpw(ushort, ushort);
extern int              __cdecl                         inp(ushort);
extern ushort   __cdecl                         inpw(ushort);
#pragma intrinsic(_enable,_disable,outp,outpw,inp,inpw)

#endif /* _MACH_H */
```

M.3 File: mvdt.h

Programmer: Jianyig Shi

```
/************* functions  in the PC_STUB file  ********/
void  VI_Open() ;
void  Img_Err() ;
/************* image data capture and transfer via DT-Connect functions ****/

void   camera_init();
void   stereo_cxfer();
void   stereo_back();
void   camera_done();

/************** MAUAL : image processing functions *********/
void   man_match();
/**************  AUTOMATIC : image processing functions *********/

void   l_threshold();
void   c_threshold();
void   auto_match();

/*********   functions for saving image file ********/
FILE    *DT_header() ;
void   dt_save();
void   dt_read();
/******** image data constants  ********/
#define SHADE_NUM    256
#define FRAME_COL    512
#define FRAME_ROW    480
#define FRAME_BYTES  262144      /* 512*512 = 262144 ; 512*480 = 245760 */
#define JUNKBITS     512       /*--- this is DT header bytes   ----*/
#define SHADE_LO   0
#define SHADE_HI    180

/******** some handy flags *********/
#define  TESTING    0
#define  SIMULATION  1
```

M.4 File state.c

```
/****************************************************************
*****
   state.c - This programe can ONLY run on PC host

   This file includes following functions :

      vi_int_init()   enable the interrupt from frame grabber DT2861
      vi_int_uninit() recover original interrupt mask and vector
      vi_int_ifunc()  interrupt handle - finite state machine

   Notes : (1) This is the interrupt mode implementation.

   Programmer :          Jianying Shi
   Date Originated :     Dec. 29, 92
   Date Last Modified :  Dec. 31, 92

****************************************************************
****/
#include <stdio.h>
#include <stdlib.h>
#include <conio.h>
#include "mach.h"

#define CAP_LOOP       10

/* ----------------- VI INTERRUPT DRIVER FOREGROUND ---------------- */

static igate_s          vi_gate;
static int              vi_state = 0 ;

int                     vi_buffer = 1 ;     /* writer here */
int                     loop_num = 0 ;      /* writer here */
int                     int_counter = 0;    /* writer here */

#pragma check_stack(off)
#include "video.c"

/* ----------------- VI INTERRUPT DRIVER FOREGROUND ----------------
|
|
-------------------------------------------------------------------*/
static void __far vi_int_ifunc(intargs_s args)
{
```

```
    outpw(0x230, (inpw(0x230) & ~DONEINT));     /* clear DONEINT bit    */
    outpw(0x234, (inpw(0x234) & ~SYNCINT));     /* clear SYNCINT bit */
    int_counter++;

/*-------------------------------------------------------------------
| switch on state - a finite state machine
-------------------------------------------------------------------*/

    switch (vi_state) {

      case 0 :

          outpw(io->incsr2, MODE(0)|BUFSEL(0));
          outpw(io->incsr1, ALUM|ALU(15)|BUSY|DONEINT);
          vi_state = (loop_num>VI_LOOP) ? 1 : 0 ;
          loop_num++;
          break ;

      case 1 :

          outpw(io->ypan, DISBUF(vi_buffer));
          outpw(io->incsr2, MODE(0)|BUFSEL(vi_buffer));
          outpw(io->incsr1, ALUM|ALU(15)|BUSY|DONEINT);
          vi_state = 0;
          loop_num = 0;
          vi_buffer++;
          break;

    }

    outp(0xA0, 0x20);                 /* ACK the slave  8259  */
    outp(0x20, 0x20);                 /* ACK the master 8259  */
    return;

}

/* ------------------------- VI DRIVER BACKGROUND -------------------------- */

static  (__interrupt __far *vec_save)();
static   ushort imsk;
static   ushort imsk_save;

static void vi_int_uninit(void)
{
      _disable();                     /* interrupts off */
```

```
        outp(0xA1, ((inp(0xA1) & ~imsk)|(imsk_save & imsk)));
    _Ksetivec(VI_VEC, vec_save);
    _enable();                      /* interrupts on */
}

void vi_int_init(void)
{

        vi_gate.opcode9A= (uchar)0x9A;
        vi_gate._Kigate= _Kigate;
        vi_gate.usrp= (void __far *)0;
    vi_gate.ifunc= vi_int_ifunc;
    imsk= (uchar)(1 << (VI_IRQ & 0x07));

    _disable();                     /* interrupts off     */
    imsk_save= inp(0xA1);           /* save slave imsk    */
    outp(0xA1, (imsk_save & (~imsk)));    /* enable video ints   */
        vec_save= _Ksetivec(VI_VEC, (void (__interrupt __far *)())&vi_gate);
    _enable();                      /* interrupts on */
    atexit(vi_int_uninit);
}
#pragma check_stack(on)
```

m.5 File: video.c

```
/**********************************************************************
*****
   video.c - This programe can ONLY run on PC host

   It is used to initializes video capture board DT2861 so that
   the board can be used for interrupt mode

   Programmer :         Jianying Shi
   Date Originated :    Feb. 21, 92
   Date Last Modified : Dec. 29, 92

**********************************************************************
****/
#include "video.h"

static video_s *io;
/**********************************************************************
******
   Initialize Video Capture Board DT2861

   input : Pointer to the Video Stucture
         Base port address for the video grabber board
         Base port address for mux if there is any
   Output: the video structure is initialized
         0 - normal termination

   Two Status of DT2861 Board after sucessful return from video_init :

   ~VI_DONE_INT :  Continuous sampling = display camera
   VI_DONE_INT  :  one sample = interrupt when done

**********************************************************************
******/
int video_init( base, muxbase)
ushort_t base, muxbase;
{
        ushort_t i, j, save;

     /* Dynamically get memsory for video stucture */

     if ((io = (video_s *)malloc( sizeof(video_s) )) == (video_s *)0)
        exit(1);
```

```
/* Initialize the I/O interface. */

    io->flags= 0;
    io->incsr1= base+0x00;
    io->incsr2= base+0x02;
    io->outcsr= base+0x04;
    io->cursor= base+0x06;
    io->index= base+0x08;
    io->xpan= base+0x08;
    io->inlut= base+0x0A;
    io->rlut= base+0x0A;
    io->ypan= base+0x0A;
    io->redgrn= base+0x0C;
    io->start= base+0x0C;
    io->blue= base+0x0E;
    io->end= base+0x0E;
    io->inputmux= muxbase;
if (muxbase != 0) io->flags |= INPUTMUX;

/* Kill the output and clear any pending operations. */

    outpw(io->outcsr, (inpw(io->outcsr) & ~DISPLAY));
outpw(io->incsr1, (inpw(io->incsr1) & ~PASS));
outpw(io->incsr1, (inpw(io->incsr1) & ~BUSY));
    while ((inpw(io->incsr1) & BUSY) == BUSY);

/* Setup output and input1 to something benign. */

    outpw(io->outcsr, 0);
outpw(io->incsr1, ALUM|ALU(3)); /* Logical F= 0  */

/*---  Don't have to initialize LUTs and frame buffers ---*/
/*---  thus old LUTs and buffers are inherited         ---*/

#if 0
/* Initialize the input LUTs. */

save = inpw(io->incsr1);
    outpw(io->incsr2, MODE(2));
    for (i= 0; i < 8; i++) {
        outpw(io->incsr1, save|INSEL(i));
        for (j= 0; j < 256; j++) {
                    outpw(io->index, j);
                    outpw(io->inlut, j);
            }
```

```
        }
        outpw(io->incsr1, save);

    /* Initialize the resultant LUTs. */

        outpw(io->incsr2, MODE(3));
        for (i= 0; i < 4; i++) {
            outpw(io->incsr1, save|RSEL(i));
            for (j= 0; j < 256; j++) {
                        outpw(io->index, j);
                        outpw(io->rlut, j);
                }
        }
        for (i= 0; i < 4; i++) {
            outpw(io->incsr1, save|RCARRY|RSEL(i));
            for (j= 0; j < 256; j++) {
                        outpw(io->index, j);
                        outpw(io->rlut, 0xFF);
                }
        }
        outpw(io->incsr1, save);

    /* Initialize the output LUTs. */

        save= inpw(io->outcsr);
        for (i= 0; i < 8; i++) {
            outpw(io->outcsr, save|OSEL(i));
            for (j= 0; j < 256; j++) {
                        outpw(io->index, j);
                        outpw(io->redgrn, RED(j)|GREEN(j));
                        outpw(io->blue, j);
                }
        }
        outpw(io->outcsr, save);
#endif

    /* Initialize frame buffers. */

        outpw(io->incsr2, MODE(0));
        outpw(io->start, SLINE(0)|SPIXEL(0));
        outpw(io->end, ELINE(-1)|EPIXEL(-1));
        for (i= 0; i < 16; i++) {
                outpw(io->incsr2, BUFSEL(i));
                outpw(io->incsr1, ASEL|BUSY|ALUM|ALU(3));
                while ((inpw(io->incsr1) & BUSY) == BUSY);
```

```
    }

  /* Initialize optional video multiplexer and set up the flay */

  if (io->flags & INPUTMUX ) {
    if ( VI_BECK ) outpw( io->inputmux, VI_BECK );
    else        outpw( io->inputmux, 1 );
  }

  /*---  if external sync source used   ---*/

#if VI_SYNC_SOURCE
  outpw(io->outcsr, DISPLAY|CURSOR|OSEL(0)|EXTTIM );
#else
  outpw(io->outcsr, DISPLAY|CURSOR|OSEL(0));
#endif

  /*-------------------------------------------------
  |  Initialize video input  ( A = F  function )
  |  One sampling for interrupt driven fuctions
  |  Continuous sampling for non-interrupt mode
  ---------------------------------------------------*/

  /* Initialize output display. */

  outpw(io->ypan, DISBUF(0));
    outpw(io->xpan, 0);
  outpw(io->cursor, CLINE(255)|CPIXEL(255));
  outpw(io->incsr2, MODE(0)|BUFSEL(0));

#if VI_DONE_INT
  outpw(io->incsr1, ALUM|ALU(15)|BUSY|DONEINT);
#else
  outpw(io->incsr1, ALUM|ALU(15)|BUSY|PASS);
#endif

  /* Mark I/O interface as initialized and pending. */

  io->flags |= INIT|PENDING;
    return(0);
}
```

M.6 File: video.h

Programmer: Jianying Shi

```
/* --- VIDEO: Generic Data Types. --- */
typedef unsigned char   byte_t;
typedef unsigned short  ushort_t;
typedef unsigned long   ulong_t;

/* --- function prototype  --- */

int       video_init( ushort_t iobase, ushort_t muxbase);

/* --- VIDEO: DT2861 Video Low Level Port I/O Package Interface. --- */
typedef struct _video {
        ushort_t    flags;          /* Port I/O package flags  */
        ushort_t    incsr1;         /* Video input control/status
                                                reg1 pio_addr   */
        ushort_t    incsr2;         /* Video input control/status
                                                reg2 pio_addr   */
        ushort_t    outcsr;         /* Video output control/status
                                                     pio_addr */
        ushort_t    index;          /* Current LUT index pio_addr*/
        ushort_t    inlut;          /* Current input LUT entry
                                                     pio_addr */
        ushort_t    rlut;           /* Current resultant LUT
                                                     pio_addr */
        ushort_t    redgrn;         /* Current red/green LUT entry
                                                     pio_addr */
        ushort_t    blue;           /* Current blue LUT entry
                                                     pio_addr */
        ushort_t    cursor;         /* Cursor control pio_addr */
        ushort_t    xpan;           /* X-panning control pio_addr */
        ushort_t    ypan;           /* Y-panning control pio_addr */
        ushort_t    start;          /* Starting line/pixel control
                                                     pio_add */
        ushort_t    end;            /* Ending line/pixel control
                                                     pio_addr */
        ushort_t    inputmux;           /* DT2859 Video multiplexer base
pio_addr */
        ushort_t    buffer;         /* pointer to current on-board
                                                     buffer */
} video_s;
```

```
/* --- VIDEO: flags macros. --- */
#define PENDING        0x0001        /* board operation left pending
*/
#define INPUTMUX       0x0002        /* optional input video mux present
*/
#define INIT           0x8000        /* board successfully initialized               */

/* --- VIDEO: incsr1 macros. --- */
#define INSEL(v)       ((v)&0x07)
#define ALUM           0x0008
#define CARRYIN        0x0010
#define PASS           0x0020
#define DONEINT        0x0040
#define BUSY           0x0080
#define RCARRY         0x0100
#define RSEL(v)        (((v)&0x03)<<9)
#define ASEL           0x0800
#define ALU(v)         (((v)&0x0F)<<12)

/* --- VIDEO: incsr2 macros. --- */
#define BUFSEL(v)      ((v)&0x0F)
#define MODE(v)        (((v)&0x07)<<4)
#define BSEL           0x0080
#define FBACK(v)       (((v)&0x0F)<<8)
#define WP(v)          (((v)&0x0F)<<12)

/* --- VIDEO: outcsr macros. --- */
#define OSEL(v)        ((v)&0x07)
#define EXTTIM         0x0008
#define CURSOR         0x0010
#define DISPLAY        0x0020
#define TRGEN          0x0040
#define EXTTRG         0x0080
        /*    reserved      0x0100        */
#define BUSBUF(v)      (((v)&0x07)<<9)
#define FRPROC         0x1000
#define FIELD          0x2000
#define SYNCINT        0x4000
#define VSYNC          0x8000

/* --- VIO: ypan register macros. --- */
#define DISBUF(v)      (((v)&0x0f)<<12)

/* --- VIDEO: redgrn macros. --- */
```

```
#define RED(v)        ((v)&0xFF)
#define GREEN(v)      (((v)&0xFF)<<8)

/* --- VIDEO: start/end macros. --- */
#define SLINE(v)      (((v)&0x1FF)<<7)
#define SPIXEL(v)     (((v)>>2)&0x7F)
#define ELINE(v)      (((v)&0x1FF)<<7)
#define EPIXEL(v)     (((v)>>2)&0x7F)

/* --- VIDEO: cursor macros. --- */
#define CLINE(v)      ((((v)>>1)&0xFF)<<8)
#define CPIXEL(v)     (((v)>>1)&0xFF)

/* --- VIDEO: channel register --- */
#define CHANNEL       0x0007

/* --- VIDEO: interrupt parameters --- */

#define VI_IRQ                    10
#define VI_VEC             0x72

#define VI_BASE             0x230
#define VI_MUX_BASE             0x2E3

#define VI_TRIG             0x378     /* port ( lpt1 ) address        */
#define VI_PULL             0x00      /* used for sync two cameras    */
#define VI_NORM               0xff     /* negative going               */

/*--- VIDEO: Compile Options. ---*/

#define VI_ERRCHECK                /* uncomment for extended error checking
*/
#define VI_MAXBOARDS   1              /* maximum supported DT2861 video
boards       */
#define VI_DONE_INT    1            /* interrupt mode flag                */
                                    /* 1 - generate interrupt when done      */
                                    /* 0 - generate no interrupt when done   */

#define VI_STEREO       0          /* flag for a pair of stereo cameras     */
#define VI_SYNC_SOURCE  1              /* sync source when capturing images
*/

                                    /* 1 - external sync : use camera sync   */
                                    /* 0 - internal sync : use syn on board  */

#define VI_BECK        4           /* Camera channel set for Dr. Beck       */
```

```
/* This needs to be changed to suit specific applications */

#define VI_LOOP          3         /* loop number for storing image to buffers */
```

M.7 File: makefile

Programmer: Jianyig Shi

```
/*makefile*/
SHELL=      sh
BIN=        .

LIBDIR =        $(AL860)/lib
LIBS =         cop860.lib
CC =        cl
CFLAGS =         -AL -G2 -I$(AL860)\include -nologo -DFAR=far
AS =        masm
AFLAGS =    -Ml

DEP1 = video.h

.asm.obj:
    $(AS) $(AFLAGS) $*,$*,,,

.c.obj:
    $(CC) -c $(CFLAGS) $*.c

OBJS=        record.obj \
                state.obj \
                mach.obj

CSRCS =   record.c state.c video.c
ASRCS =   mach.asm



record.exe:    $(OBJS) $(DEP1)
    cl -o $@ $(OBJS)
    rm state.obj
    rm record.obj

state.obj : state.c video.c
    $(CC) -c $(CFLAGS) state.c
```

M.8 File record.c

Programmer: Jianying Shi

```
#include <stdio.h>
#include <stdlib.h>
#include "mach.h"
#include "video.h"

extern int          loop_num ;      /* reader here */
extern int          int_counter ;   /* reader here */
extern int          vi_buffer ;     /* reader here */

int main(void)
{
    int         c, fg_state;
    double        sk;

    video_init( 0x230, 0x2E3 );

printf("\033[2J");              /* clear screen */
printf("\033[2;23H");             /* paint defaults*/
printf("\033[10;1H");             /* paint defaults*/

sk = (double)VI_LOOP/(double)30;

printf("\n working ... this will capture one image every %4f second\n", sk+0.1);


    vi_int_init();
    while ( vi_buffer < 14 ) {
        printf("\033[20;10H%4d", vi_buffer);
        printf("\033[20;20H%4d", loop_num);
        printf("\033[20;30H%4d", int_counter);
    }

printf("\033[22;10H");
printf("\n DONE !\n");

        return(0);
}
```

M.3 File: mydt.h

Programmer: Jianyig Shi

```
/************* functions  in the PC_STUB file  ********/
void  VI_Open() ;
void  Img_Err() ;
/************* image data capture and transfer via DT-Connect functions ****/

void   camera_init();
void   stereo_cxfer();
void   stereo_back();
void   camera_done();

/************** MAUAL : image processing functions *********/
void   man_match();
/**************  AUTOMATIC : image processing functions *********/

void   l_threshold();
void   c_threshold();
void   auto_match();

/*********   functions for saving image file ********/
FILE    *DT_header() ;
void   dt_save();
void   dt_read();
/******** image data constants  ********/
#define SHADE_NUM    256
#define FRAME_COL    512
#define FRAME_ROW    480
#define FRAME_BYTES  262144      /* 512*512 = 262144 ; 512*480 = 245760 */
#define JUNKBITS     512       /*--- this is DT header bytes   ----*/
#define SHADE_LO   0
#define SHADE_HI    180

/******** some handy flags *********/
#define  TESTING    0
#define  SIMULATION  1
```

M.7 File: makefile

Programmer: Jianyig Shi

```
/*makefile*/
SHELL=        sh
BIN=

LIBDIR =           $(AL860)/lib
LIBS =            cop860.lib
CC =          cl
CFLAGS =            -AL -G2 -I$(AL860)\include -nologo -DFAR=far
AS =          masm
AFLAGS =      -Ml

DEP1 = video.h

.asm.obj:
    $(AS) $(AFLAGS) $*,$*,,,

.c.obj:
    $(CC) -c $(CFLAGS) $*.c

OBJS=           record.obj \
                    state.obj \
                    mach.obj

CSRCS =     record.c state.c video.c
ASRCS =     mach.asm



record.exe:     $(OBJS) $(DEP1)
        cl -o $@ $(OBJS)
        rm state.obj
        rm record.obj

state.obj : state.c video.c
        $(CC) -c $(CFLAGS) state.c
```

APPENDIX N

Image Processing Programs

N.1 image.c Program Source Code

```
/*
*****************************************************************
***
   DT_read.c    This programe can run on both i860 and PC

   Purpose : Read an image data in .IMG format into a buffer
                (optional ) : Read the a background Image and Subtract It From
The First Image

   Input :  filename, image data length in bytes,
            pointer to image data
   Output :  None

   Programmer :       Jianying Shi
   Date Originated :   April 22, 92

   Notes :  (1) if run on PC, be aware the size limitation on
                image buffer
            (2) if run on I860, no size limitation problem

*****************************************************************
***
*/
#include <stdlib.h>
#include <stdio.h>


main()
{
     int    x, y ;
        unsigned char grey_shade,grey_shade2;
     FILE   *fin, *fout,*fbk;
     char   fl_in[20], fl_out[20];

     /* --- open files for reading in image data --- */
     printf( "Enter the input file name: " );
     scanf( "%s%*c", fl_in );
     if( ( fin=fopen(fl_in,"rb") ) == NULL ){
          printf( "\n Unable to open input file %s \n", fl_in );
```

```
        exit(1) ;
    }


    /*if( ( fbk=fopen("c:bak.img","rb") ) == NULL ){
            printf( "\n Unable to open input file %s \n", "c:bak.img" );
        exit(1) ;
    }*/

/* --- open files for writing out image data --- */
printf( "Enter the output file name: " );
scanf( "%s%*c", fl_out );
if( ( fout=fopen(fl_out,"wb") ) == NULL ){
        printf( "\n Unable to open output file %s \n", fl_out );
        exit(1) ;
}

/* --- read in the header part and discard them --- */
    for( x=0; x<512; x++ ){
     grey_shade = (unsigned char)fgetc( fin );
     //grey_shade2 = (unsigned char)fgetc( fbk );
    }

/* --- read in the image body --- */
fprintf( fout, "%s", "P5\n" );
    fprintf( fout, "%d %d\n", 512, 480 );
    fprintf( fout, "%d\n", 255 );
    for( y=0; y<512; y++ ){
            for( x=0; x<512; x++ ){     /* --- read in row by row --- */
                    grey_shade = (unsigned char)fgetc( fin );
                    //grey_shade2 = (unsigned char)fgetc( fbk );
                    grey_shade =grey_shade;
                    if(grey_shade<0) grey_shade=0;
                    putc( grey_shade, fout );
            }
    }

    fclose( fin );
    fclose( fout );

    return(0);
}
```

N.2 process.c Program Source Code

```
/*
*********************************************************************
***
   process.c    This programe can not run on PC

   Purpose : Read an image data in .PMG format, Crop the Image, Draw a
             0.25 in 0.25 ingrid in the cropped area.

   Input :  Input and Outpur filenames, horizontal and vertical scale factors, size
            of the cropped area, and the coordintaes of the top right corner.

   Output :  Cropped and Gridded Image

   Programmer :        Samer Mahmoud
   Date Originated :   April 22, 92

   Notes : (1) if run on PC, be aware the size limitation on
           image buffer
         (2) if run on I860, no size limitation problem

*********************************************************************
***
*/
#include <stdlib.h>
#include <stdio.h>


main()
{
     int    x, y,xcount=-1,ycount=-1,dx,dy ,temp,num;

     unsigned char grey_shade[480][512],grey[144][114],map1,map2,max=0;
     FILE   *fin, *fout;
     char   fl_in[20], fl_out[20],discard[50];

     /* --- open files for reading in image data --- */
     printf( "Enter the input file name: " );
     scanf( "%s%*c", fl_in );
     if( ( fin=fopen(fl_in,"rb") ) == NULL ){
          printf( "\n Unable to open input file %s \n", fl_in );
          exit(1) ;
     }

     /* --- open files for writing out image data --- */
```

```
printf( "Enter the output file name: " );
scanf( "%s%*c", fl_out );
if( ( fout=fopen(fl_out,"wb") ) == NULL ){
      printf( "\n Unable to open output file %s \n", fl_out );
      exit(1) ;
}

/* --- read in the header part and discard them --- */
for(x=0;x<=17;x++){
            fscanf(fin,"%s",discard);
    printf("%s\n",discard);
    }


/* --- read in the image body --- */
fprintf( fout, "%s", "P5\n" );
fprintf( fout, "%d %d\n", 114,144);
fprintf( fout, "%d\n", 255 );
for( y=0; y<480; y++ ){
      for( x=0; x<512; x++ ){     /* --- read in row by row --- */
                  grey_shade[y][x] = (unsigned char)fgetc(fin);

      }
}

for( y=0; y<480; y++ ){
      for( x=0; x<512; x++ ){     /* --- read in row by row --- */
                  if(grey_shade[y][x]>=max) max=grey_shade[y][x];
      }
}

   map1=3*max;
   map2=2*max;

for( y=0; y<480; y++ ){
            if(y>=196 && y<=340) ycount+=1;
      for( x=0; x<512; x++ ){     /* --- read in row by row --- */
                  dx=x-248;
                  if(y>=196 && y<=340){
                    if(x>=191 && x<=305){
                      xcount+=1;
                      grey[ycount][xcount]=grey_shade[y][x];
                    }
            }
```

```
		}
		xcount=-1;

	}
	 xcount=-1;
	 ycount=-1;
	   for( y=0; y<480; y++ ){
			dy=y-196;
			if(y>=196 && y<=340) ycount+=1;
		for( x=0; x<512; x++ ){     /* --- read in row by row --- */
				dx=x-248;
				if(y>=196 && y<=340){
				  if(x>=191 && x<=305){
				    xcount+=1;
				    // printf("%d %d\n",ycount,xcount);
			if(x==248) grey[ycount][xcount]=map1;
				    if((dx%19)==0 && x !=248)
grey[ycount][xcount]=map2;
				    if(y==196) grey[ycount][xcount]=map1;
			if((dy%24)==0 && y !=196) grey[ycount][xcount]=map2;
				  }
				}
		}
		xcount=-1;

	}

	for( y=0; y<144; y++ ){
		for( x=0; x<114; x++ ){     /* --- read in row by row --- */
				putc(grey[y][x], fout );

		}
	}
	fclose( fin );
	fclose( fout );

	return(0);
}
```

APPENDIX O

Variation of Chamber Temperature During Tests

Two independent tests were run to monitor the transient temperature response of the water inside the test chamber during tests. In the first test, the temperature of the water inside the plastic bucket containing the copper coils was not controlled. This test was started with the discharge temperature about 72.8 °F, which was about 0.3 °F above the temperature of the water inside the chamber. The temperature was monitored frequently for 250 minutes. In the second test, the temperature of the water in the plastic bucket containing the copper coils was controlled by introducing tap water at 1 GPM and about 65.7 °F, and the temperatures were monitored for about 30 minutes. The results of both tests were plotted in Figures O.1 and O.2. As Figure O.1 shows, increasing the discharge temperature lead to an increase in the water temperature. The rate of change in the discharge water temperature was about 0.028 °F/min. initially, then the rate slowed a little. From Figure O.2, the cold temperature jet reached steady-state in about 7.5 minutes and lasted about 23 minutes before the ambient temperature started significantly changing. This was approximately a sufficient time to run the negatively buoyant tests, since the tests took about 30 minutes to complete.

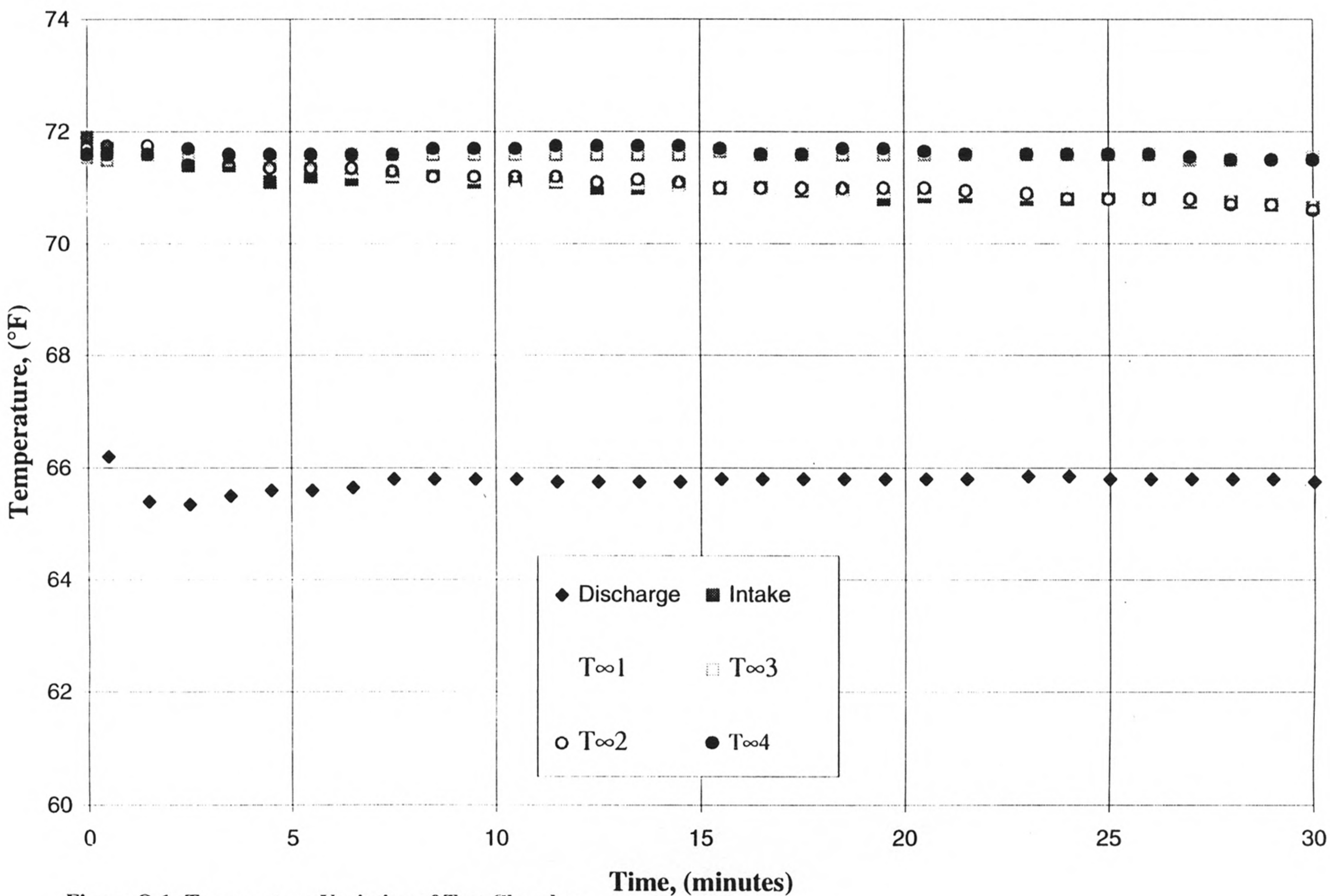

Figure O.1: Temperature Variation of Test Chamber
(Cooling Water Was Controlled)

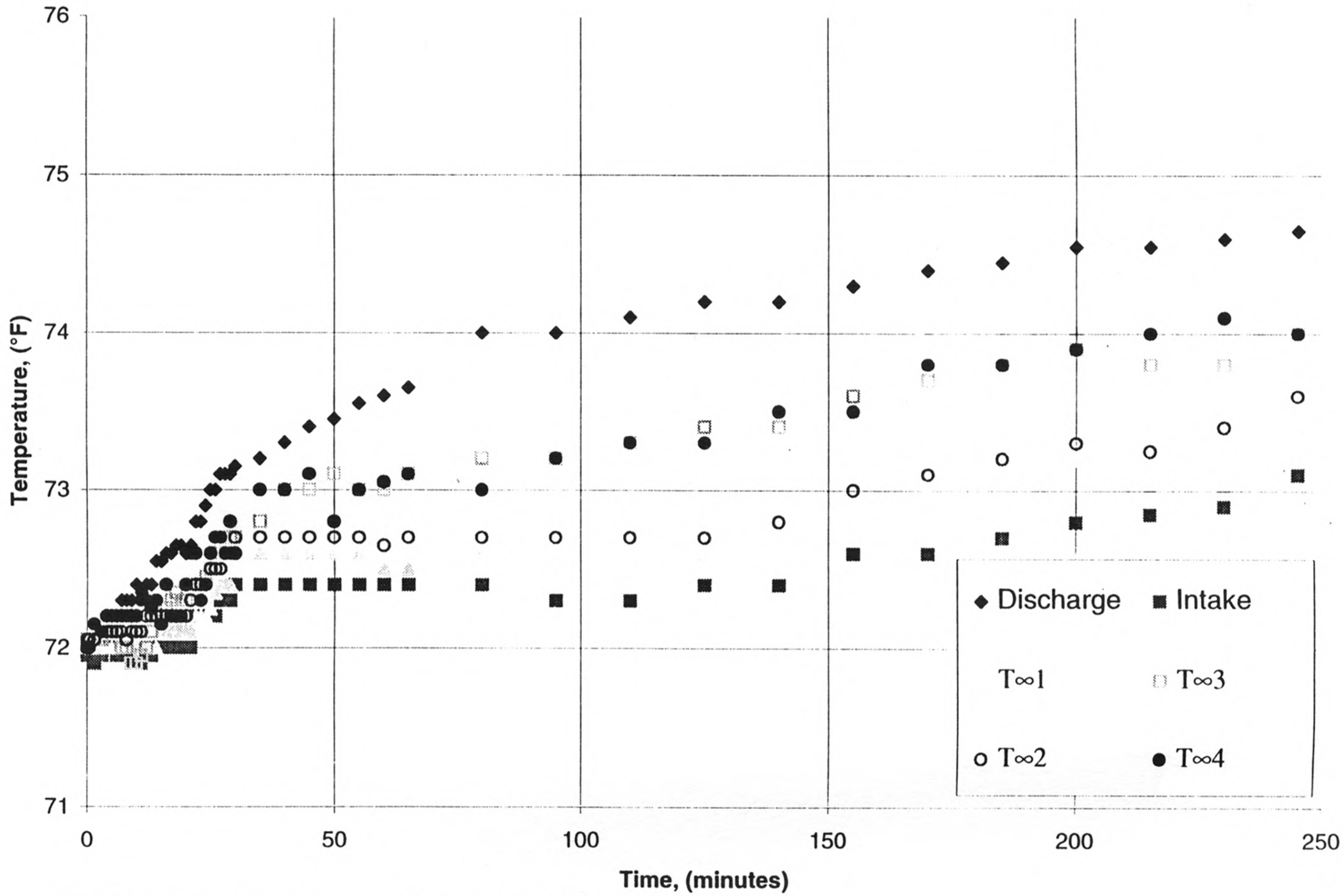

Figure O.2: Temperature Variation of Test Chamber
(Cooling Water Was Not Controlled)